Activation of Small Molecules by the Metal-Amido Bond of Rhodium(III) and Iridium(III) (η^5-C$_5$Me$_5$)M-Aminopyridinate Complexes

Ana Zamorano, Nuria Rendón,[*] Joaquín López-Serrano, Eleuterio Álvarez, and Ernesto Carmona

Instituto de Investigaciones Químicas (IIQ) Departamento de Química Inorgánica and Centro de Innovación en Química Avanzada (ORFEO-CINQA)

Consejo Superior de Investigaciones Científicas (CSIC) and Universidad de Sevilla

Av. Américo Vespucio 49, Isla de la Cartuja, 41092 Sevilla (Spain)

Fax: (+34)954460565

E-mail: nuria@iiq.csic.es (N. R.)

ABSTRACT.

We report the synthesis and structural characterization of five-coordinate complexes of rhodium and iridium of type $[(\eta^5\text{-}C_5Me_5)M(N^\wedge N)]^+$ (**3-M$^+$**), where N^N represents the aminopyridinate ligand derived from 2-NH(Ph)-6-(Xyl)C$_5$H$_3$N (Xyl = 2,6-Me$_2$C$_6$H$_3$). The two complexes were isolated as salts of the BAr$_F$ anion (BAr$_F$ = B[3,5-(CF$_3$)$_2$C$_6$H$_3$]$_4$).

The M—N$_{amido}$ bond of complexes **3-M$^+$** activated readily CO, C$_2$H$_4$ and H$_2$. Thus, compounds **3-M$^+$** reacted with CO under ambient conditions, but whereas for **3-Rh$^+$**, CO migratory insertion was fast yielding a carbamoyl carbonyl species, **4-Rh$^+$**, the stronger Ir—N$_{amido}$ bond of complex **3-Ir$^+$** caused the reaction to stop at the CO coordination stage. In contrast, **3-Ir$^+$** reacted reversibly with C$_2$H$_4$ forming adduct **5-Ir$^+$**, which subsequently rearranged irreversibly to a [Ir](H)(=C(Me)N(Ph)-) complex **6-Ir$^+$**, that contains a N-stabilized carbene ligand. Computational studies supported a migratory insertion mechanism, giving first a β-stabilized linear alkyl unit, [Ir]-CH$_2$CH$_2$N(Ph)-, followed by a multi-step rearrangement that led to the final product **6-Ir$^+$**. Both β- and α-H eliminations, as well as their microscopic reverse migratory insertion reactions, were implicated in the alkyl-to-hydride/carbene reorganization. The analogous reaction of **3-Rh$^+$** with C$_2$H$_4$ originated a complex mixture of products from which only a branched alkyl [Rh]-C(H)(Me)N(Ph)- (**5-Rh$^+$**) could be isolated, featuring a β-agostic methyl interaction. Reactions of **3-M$^+$** with H$_2$ promoted a catalytic isomerization of the Ap ligand from classical k^2-N,N´ binding to k-N plus η^3-pseudoallyl coordination mode.

INTRODUCTION

In recent years we have explored the chemistry of cationic $[(\eta^5\text{-}C_5Me_5)M(III)]$ complexes of rhodium and iridium stabilized by coordination to bulky, formally monoanionic bidentate ligands (L^X), encompassing cyclometalated phosphines and especially in the context of this work, aminopyridinates.[1,2] The latter are also called pyridylamido ligands and are represented onwards in a simplified manner as Ap or as N^N (see Figure 1).[3] Compounds built around $[(\eta^5\text{-}C_5Me_5)M]$ rhodium and iridium frameworks have arisen considerable interest, for they are valuable molecules finding countless applications in catalysis,[4-7] bio-organometallic studies,[8,9] and other areas of research.[10]

Similarly to previously reported amido complexes of late transition metals,[11] the amido nitrogen atom of metal-bound aminopyridinate groups can function as a π-donor (Figure 1a), partially offsetting the electronic unsaturation of positively charged metal centers, and allowing the stabilization of five-coordinate complexes of the type $[(\eta^5\text{-}C_5Me_5)M(N^\wedge N)]^+$. As represented in Figure 1, bulky aryl substituents on both the amido and six-position of the pyridine termini, may provide desirable steric protection to the low-coordinate metal center.

The previously reported complexes[1,2] behaved as markedly reactive Lewis acids when treated with a variety of Lewis bases (L), forming readily the corresponding six-coordinate, 18-electron adducts $[(\eta^5\text{-}C_5Me_5)M(N^\wedge N)(L)]^+$ (L = NH_3, NCMe, CNXyl, and others). Intriguingly, none of the compounds investigated reacted with C_2H_4 even under rather forcing conditions, hampering observation of products originating from migratory insertion of the alkene into the M—N_{amido} bond.[12,13] It appeared plausible that failure to detect C_2H_4 reactivity was due to steric reasons, in other words, that the required side-on metal approach of the C=C bond was impeded by steric interactions with the C_5Me_5 and Ap ligands, in particular with the aryl substituents of the amido nitrogen atom. In accordance with this assumption, it was found that complexes of rhodium and iridium alike, exhibited a significant decrease in the rate of the H_2-catalyzed isomerization of the coordinated pyridylamido ligand from the common k^2-

N,N´ binding to an unconventional k-N,η^3-benzylic bonding mode (Figure 1b), when the N_{amido} substituent was changed from $2,6\text{-}Me_2C_6H_3$ to $2,6\text{-}Pr_2^iC_6H_3$.

Considering the above information, we deemed of interest studying the chemistry of related $[(\eta^5\text{-}C_5Me_5)M(N^\wedge N)]^+$ complexes, **3-Rh$^+$** and **3-Ir$^+$**, in which the aminopyridinate ligand is the conjugated base of phenyl[6-(2,6-dimethylphenyl)pyridine-2-yl]amine (compound **1** in Figure 1c). Relative to previously assayed Ap ligands, little if any relevant changes are introduced in the overall electronic properties of the $N^\wedge N$ chelating unit, whereas replacing the N_{amido} $2,6\text{-}R_2C_6H_3$ (R = Me, Pr^i) substituent by the substituent-devoid phenyl group is expected to mitigate significantly steric hindrance in the vicinity of the short $M\!=\!=\!=\!N_{amido}$ bond of complexes **3-M$^+$**, facilitating ligand coordination.

In this contribution we report studies on the reactivity of complexes **3-M$^+$** toward C_2H_4 that proceeds under mild conditions yielding products stemming from migratory insertion of the olefin into the M—N_{amido} bond.[12,13] Computational studies supporting a mechanistic path entailing irreversible C-N bond formation, along with reversible α- and β-H eliminations, and their microscopic reverse migratory insertion reactions, are also incorporated.[14] Furthermore, for the investigated reaction of **3-Ir$^+$** with C_2H_4, formation of the experimentally observed hydride-carbene product **6-Ir$^+$** was computed to be more favorable than generation of the alternative hydride-olefin isomer. The mentioned reactivity adds to the observation of CO migratory insertion into the Rh—N_{amido} bond of **3-Rh$^+$**, and to the diverse and unusual H-H, C-H and N-H bond activation encountered in the reactions of H_2 with complexes **3-M$^+$**, although the latter activations are predictable on the basis of previous work.[1,2]
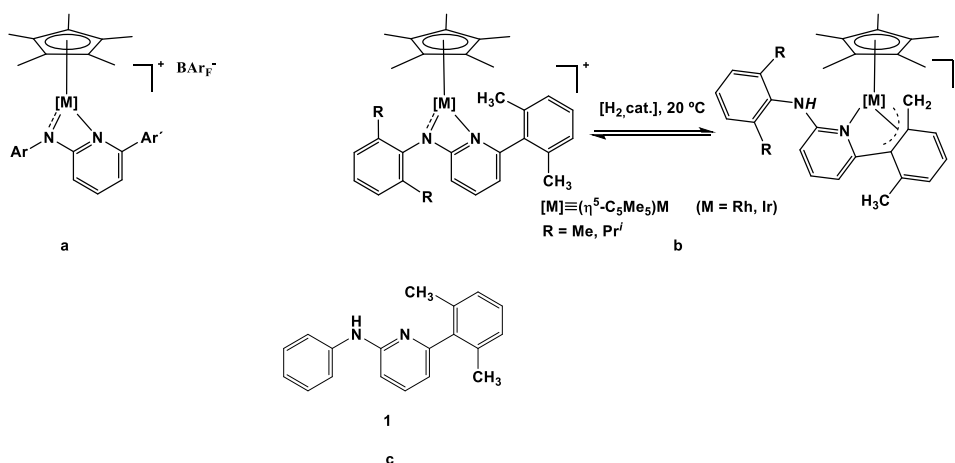
Figure 1. (**a**) General representation for five-coordinate complexes of $[(\eta^5\text{-}C_5Me_5)M(III)]^+$ units (M = Rh, Ir) and aryl-substituted aminopyridinate ligands. (**b**) Previously reported H_2-catalyzed isomerization of the Ap ligand of complexes of type **a**. (**c**) The aminopyridinate precursor, **1**, utilized in this work.

RESULTS AND DISCUSSION

Rhodium and iridium cationic $[(\eta^5\text{-}C_5Me_5)M(Ap)]^+$ complexes. The synthesis of the amine ligand precursor ApH (compound **1**, Figure 1c) was performed as reported previously for analogous, differently substituted aminopyridines.[1b] Synthetic and characterization details can be found in the Supporting Information (SI, see Scheme S1). The neutral chloride complexes $[(\eta^5\text{-}C_5Me_5)M(Cl)(Ap)]$ (**2-Ir**, **2-Rh**), were obtained from the corresponding $[(\eta^5\text{-}C_5Me_5)MCl_2]_2$ dimers and the lithium amide, LiAp. As shown in Scheme 1, the chloride ligand of compounds **2-M** was readily extruded by action of NaBAr$_F$ (BAr$_F$ = B[3,5-$(CF_3)_2C_6H_3$]$_4$) to give the five-coordinate amido-pyridine complexes $[(\eta^5\text{-}C_5Me_5)M(N^\wedge N)]^+$ (**3-Ir$^+$**, **3-Rh$^+$**). The reactions were accompanied by a pronounced color change from the original yellow or reddish to almost black or dark brown, for Ir and Rh, respectively. As noted previously,[1,2] the dark color of these complexes is typical of compounds of this kind in which the M—N$_{amido}$ functionality has multiple bond character, due to σ- and π-donation from the anionic nitrogen atom.[10,15]
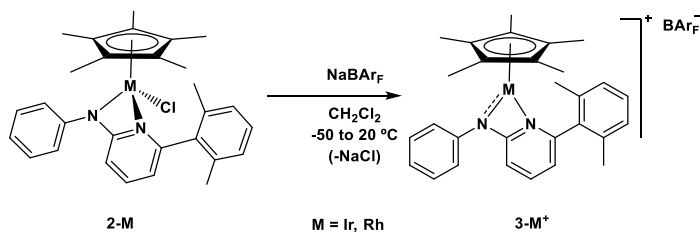
Scheme 1. Synthesis of the cationic complexes 3-M$^+$.

The four complexes **2-M** and **3-M⁺** (M = Rh, Ir) were fully characterized by microanalysis, IR and multinuclear 1D and 2D NMR spectroscopy (see the Experimental Section and SI). In addition, neutral compounds **2-M**, as well as **3-Ir⁺**, were structurally authenticated by single-crystal X-ray studies. Figure 2 depicts the molecular structure of **3-Ir⁺**, while those of chloride derivatives **2-M** (Ir and Rh) are collected in Figures S35-S36 (see the SI). Metrical parameters have normal values, though it is worth remarking that the Ir—N_{amido} bond length of this complex (Ir1—N2 in Figure 2) at 1.972(6) Å, is significantly shorter than the corresponding bond in the neutral chloride precursor **2-Ir** (2.092(2) Å), in agreement with the proposed π-donor nature of the N_{amido} function of **3-Ir⁺**. Besides, the Ir1—N2 bond is also significantly shorter than the dative covalent Ir1—N1 bond to the pyridine moiety (2.109(6) Å)
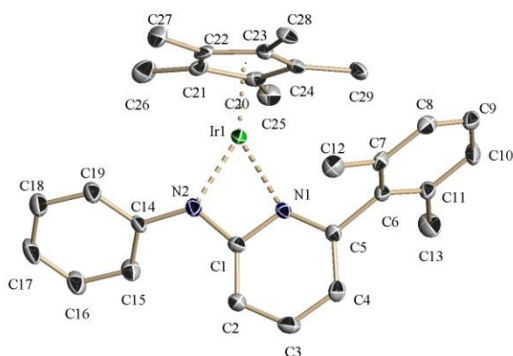

Figure 2. X-ray structure of complex **3-Ir⁺** (30% ellipsoids, anion BArF⁻ and hydrogens omitted for clarity). Selected bond lengths (Å) and angles (deg): Ir(1)–N(1) 2.109(6), Ir(1)–N(2) 1.972(6), Ir(1)–C(22) 2.158(7), Ir(1)–C(23) 2.176(7), Ir(1)–C(20) 2.133(8), Ir(1)–C(24) 2.194(7), Ir(1)–C(21) 2.155(7), N(2)-Ir(1)-N(1) 64.3(2), C(1)-N(1)-Ir(1) 93.2(4), C(1)-N(2)-Ir(1) 98.2(4), N(1)-C(1)-N(2) 104.3(6)

Reactions of Complexes 3-M⁺ with CO and C₂H₄. Similarly to related complexes of diversely substituted Ap ligands,[1,2] the rhodium and iridium derivatives **3-M⁺** exhibited distinct behaviour toward CO (Scheme 2). Thus, the room-temperature reaction of **3-Ir⁺** afforded the carbonyl adduct **4-Ir⁺**, characterized by an IR absorption at 2048 cm⁻¹ due to the stretching of the iridium-bound C—O bond. Under the reaction conditions (Scheme 2) migratory insertion of CO into the Ir—N_{amido} bond did not take place. In contrast, an analogous CO adduct was not detected for rhodium, for

nucleophilic attack of the Rh—N$_{amido}$ bond to the coordinated carbonyl occurred very rapidly, with formation of a five-member chelating carbamoyl-pyridine group that became stabilized by coordination of a second molecule of CO, giving the isolated complex **4-Rh$^+$**. The incorporated CO units of this derivative gave rise to IR bands at 2077 (Rh—CO) and 1687 cm^{-1} (Rh—C(O)N), along with corresponding ^{13}C NMR resonances with δ 187.1 and 189.3 ppm ($^1J_{CRh}$ = 76 and 30 Hz), respectively. Although not unprecedented, the insertion of carbon monoxide into a late transition metal-amide bond is a rather uncommon reaction.[2,16] It seems probable that the stronger third-row metal-N$_{amido}$ bond, relative to the Rh—N$_{amido}$ bond, retards migratory insertion of CO, preventing observation of the analogous iridium-carboxamide linkage. In this regard it is worth remarking that migratory insertion of CO into the M—CH$_3$ bond of the two different systems, *fac*-[M(CH$_3$)(I)$_3$(CO)$_2$]$^-$ and [(η^5-C$_5$Me$_5$)M(Me)Cl(CO)], is five or six orders of magnitude faster on rhodium than on iridium.[17]
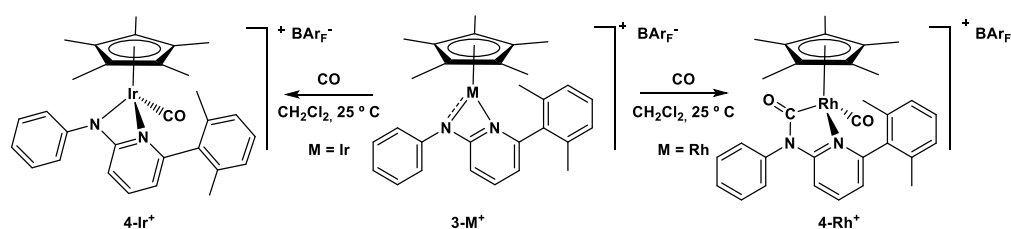
Scheme 2. Synthesis of the carbonyl complexes 4-Ir$^+$ and 4-Rh$^+$. Reactions were performed at room temperature under 1 bar of CO.

The carbonyl derivatives **4-M$^+$** were also characterized by single-crystal X-ray studies. Figure 3 contains ORTEP perspective views of the molecules of the two compounds. Some relevant bond distances and angles are also given. Besides the noticeable, although expected increase in the length of the Ir—N$_{amido}$ bond of **4-Ir$^+$**, now devoid of π-component, relative to **3-Ir$^+$** (2.089(6) *vs.* 1.972(6) Å), metrical parameters have normal values.
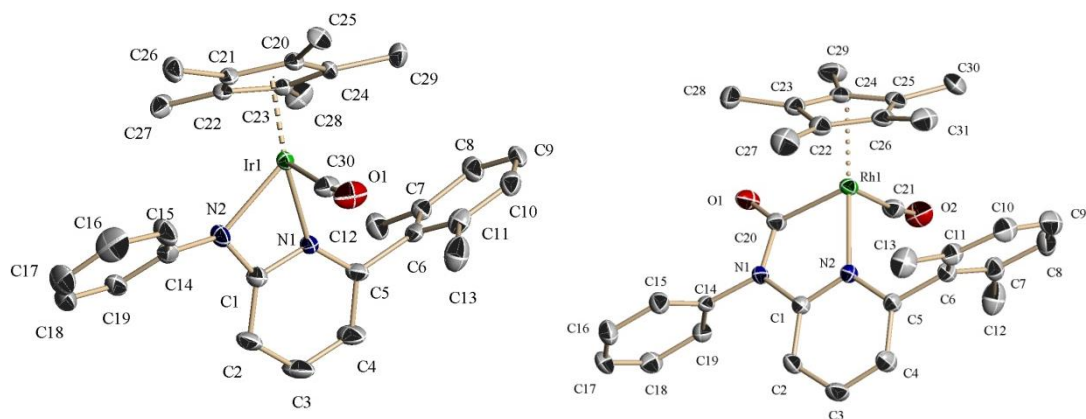
Figure 3. X-ray structure of complexes **4-Ir$^+$** and **4-Rh$^+$** (30% ellipsoids, anion BArF$^-$ and hydrogens omitted for clarity). Selected bond lengths (Å) and angles (deg) for **4-Ir$^+$**: Ir(1)–N(1) 2.137(7), Ir(1)–C(21) 2.163(6), Ir(1)–N(2) 2.089(6), Ir(1)–C(22) 2.232(7), Ir(1)–C(30) 1.874(8), Ir(1)–C(23) 2.259(8), O(1)–C(30) 1.145(9), Ir(1)–C(24) 2.216(10), Ir(1)–C(20) 2.181(7), C(30)-Ir(1)-N(1) 94.2(3), C(1)-N(1)-Ir(1) 94.3(5), C(30)-Ir(1)-N(2) 94.5(3), C(1)-N(2)-Ir(1) 96.3(5), N(2)-Ir(1)-N(1) 62.0(2), N(1)-C(1)-N(2) 107.1(8). Selected bond lengths (Å) and angles (deg) for **4-Rh$^+$**: Rh(1)–N(2) 2.152(3), Rh(1)–C(21) 1.908(5), O(2)–C(21) 1.115(6), Rh(1)–C(20) 2.026(4), O(1)–C(20) 1.200(5), Rh(1)–C(22) 2.235(5), Rh(1)–C(23) 2.251(5), Rh(1)–C(24) 2.157(4), Rh(1)–C(25) 2.262(4), Rh(1)–C(26) 2.333(5), C(21)-Rh(1)-N(2) 94.55(17), C(21)-Rh(1)-C(20) 88.9(2), C(20)-Rh(1)-N(2) 79.13(15), N(1)-C(20)-Rh(1) 111.9(3), C(1)-N(2)-Rh(1) 112.5(3), N(2)-C(1)-N(1) 115.0(4).

As already recalled, the reported $[(\eta^5\text{-C}_5\text{Me}_5)\text{M(N}^\wedge\text{N)}]^+$ iridium and rhodium complexes analogous to **3-M$^+$** (Figure 1b) were unreactive against C_2H_4 (1 bar, room temperature to 130 °C). Alkenes react readily with M—H and M—C bonds through migratory insertion, a fundamental reaction in organotransition metal chemistry, key to a large number of stoichiometric and catalytic transformations.[10] In marked contrast, the analogous reaction of an olefin with the M—N bond of an isolated metal-amido complex to generate a new C—N bond is a less well stablished transformation, the first examples of which having been reported in recent years.[12,13]

When an ethylene atmosphere (1 bar) was introduced in a Young NMR tube containing a CD$_2$Cl$_2$ solution of **3-Ir$^+$**, an immediate color change from almost black to

orange took place, hinting the formation of the desired C_2H_4 adduct $[(\eta^5\text{-}C_5Me_5)Ir(N^\wedge N)(C_2H_4)]^+$ (**5-Ir$^+$**), with the structure shown in Scheme 3. Though C_2H_4 coordination was reversible, such that removal of the ethylene atmosphere under vacuum restored the original black color of complex **3-Ir$^+$**, upon standing at room temperature under C_2H_4 over a period of 24 h, adduct **5-Ir$^+$** rearranged irreversibly to the hydride complex **6-Ir$^+$**. As depicted in Scheme 3, the coordination of the Ir(III) center of this species is completed by a chelating carbene-pyridine ligand resulting from C-N coupling between a molecule of C_2H_4 and the amido nitrogen atom of the original pyridylamido ligand.
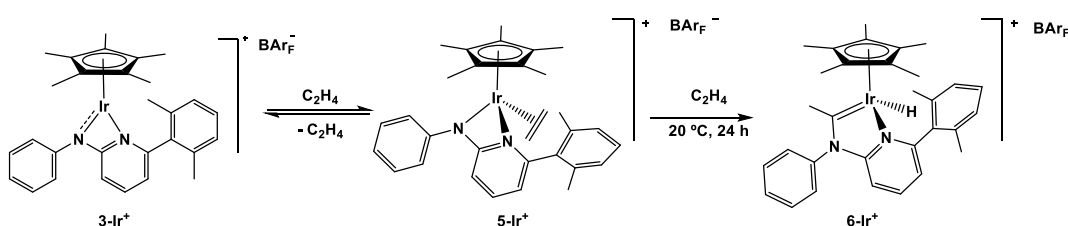
Scheme 3. Reaction of cation 3-Ir$^+$ with ethylene.

Adduct **5-Ir$^+$** could only be studied by solution NMR spectroscopy due to the facility of C_2H_4 dissociation, whereas the stable complex **6-Ir$^+$** was isolated as a crystalline solid and fully characterized by microanalytical, spectroscopic (IR and NMR) and X-ray data. No ^{1}H NMR resonances were recorded at room temperature for the coordinated ethylene molecule of **5-Ir$^+$**, but at -40 ºC a characteristic AA´BB´ multiplet was observed centered at δ 4.02, with δ_A nearly equal to δ_B. In the $^{13}C\{^1H\}$ NMR spectrum registered also at -40 ºC, the corresponding signal appeared at 61.7 ppm. Comparison with the δ value found for free C_2H_4 of 123 ppm reveals a $\Delta\delta$ shift to low frequency of around 61 ppm. This shift is smaller than that recorded for the related $[(\eta^5\text{-}C_5Me_5)Rh(P^\wedge C)(C_2H_4)]^+$ species of cyclometalated $PPr_2{}^i Xyl$ (*ca.* δ 47 and $\Delta\delta$ 76 ppm),[18] suggesting reduced π-back-bonding to ethylene in the present complex.

The existence of hydride and carbene ligands in the formulation proposed for the isomeric complex **6-Ir$^+$** is strongly backed by spectroscopic data. The Ir—H bond gives rise to an IR band at 2096 cm^{-1} due to its stretching vibration, and to a shielded ^1H NMR resonance at -16.42 ppm that appears as a broad singlet. In turn, the ^{13}C nucleus of the

carbene ligand resonates at 235.9 ppm. Figure 4 shows the solid-state structure of the molecules of this complex, corroborating the formulation anticipated in Scheme 3 on the basis of spectroscopic data. The Ir1—C20 bond to the carbene carbon atom has a length of 1.911(12) Å, very similar to distances found for other cationic and neutral carbene complexes of Ir(III) reported by our group.[18-21] The Ir1—N1 bond to the pyridine ring has a distance of 2.113(8) Å that is also comparable to Ir—N$_{pyridine}$ distances found in related complexes described in this paper or previously.[1,2]
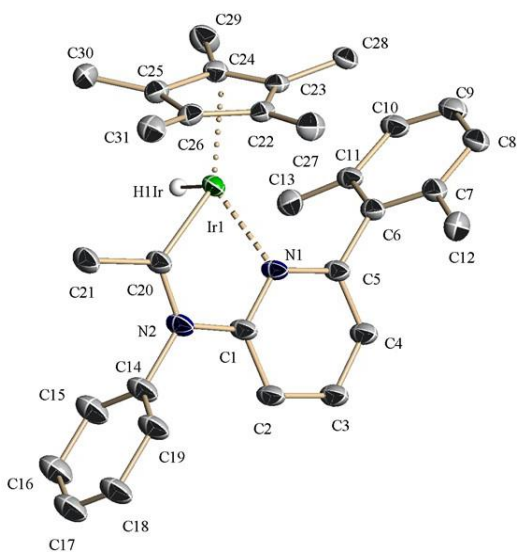

Figure 4. X-ray structure of complex **6-Ir$^+$** (30% ellipsoids, H atoms and anion BAr$_F^-$ omitted for clarity). Selected bond lengths (Angstroms) and angles (degrees): Ir(1)–C(20) 1.911(12), Ir(1)–C(23) 2.340(11), Ir(1)–N(1) 2.113(8), Ir(1)–C(24) 2.280(13), Ir(1)–H(1Ir) 1.6070, Ir(1)–C(25) 2.161(12), N(2)–C(20) 1.345(14), Ir(1)–C(26) 2.226(10), Ir(1)–C(22) 2.284(11), C(20)-Ir(1)-N(1) 78.4(4), C(20)-N(2)-C(1) 115.5(10), C(20)-Ir(1)-H(1Ir) 89.1, N(1)-C(1)-N(2) 116.2(10), N(1)-Ir(1)-H(1Ir) 87.0, N(2)-C(20)-Ir(1) 118.8(8), C(1)-N(1)-Ir(1) 111.1(7).

By analogy with previously reported studies, the α-H elimination that leads to complex **6-Ir$^+$** is expected to be reversible.[18-23] Indeed, observation of the hydride resonance of **6-Ir$^+$** as a broad singlet (*vide supra*) may be suggestive of fast equilibration of this complex with undetectable concentrations of the cyclic alkyl-pyridine solvent species **6-Ir·CD$_2$Cl$_2$$^+$** (Scheme 4), resulting from fast migratory

insertion of the carbene ligand of **6-Ir$^+$** into the Ir—H bond, promoted by coordination of CD$_2$Cl$_2$.[19a] Reaction of **6-Ir$^+$** with an excess of PMe$_3$ triggered the anticipated 1,2-H shift from iridium to the carbene carbon atom, though subsequent chemical changes must be invoked to account for the chemical constitution of the resulting product **7-Ir$^+$**. As specified in Scheme 4, this complex incorporates two molecules of PMe$_3$ and contains in addition a β-functionalized linear alkyl Ir—CH$_2$CH$_2$N$_{amido}$(Ph)-, that derives formally from a direct N—C coupling reaction between the amido terminus of the Ap ligand and a molecule of C$_2$H$_4$. In other words, beyond accomplishing migratory insertion reactivity between the hydride and carbene units of **6-Ir$^+$**, PMe$_3$ induces a branched-to-linear isomerization of the resulting secondary alkyl ligand, Ir—CH(Me)N(Ph)-, and decoordination of its pyridine end. As discussed in the following paragraphs dealing with computational studies, the reactivity represented in Schemes 3 and 4 entails competitive α- and β-H elimination reactions and their microscopic reverse migratory insertions of carbene and olefin functionalities into Ir—H bonds. Monitoring of the reaction between **6-Ir$^+$** and PMe$_3$ by ^{31}P{^{1}H} spectroscopy at low temperature (from -80 ℃ to 20 ℃) did not provide additional useful information. Immediate formation of a complex mixture of products occurred at low temperatures and at 0 ℃ this mixture slowly converted into the final complex **7-Ir$^+$**, that became the only observable species after 15 h at room temperature.
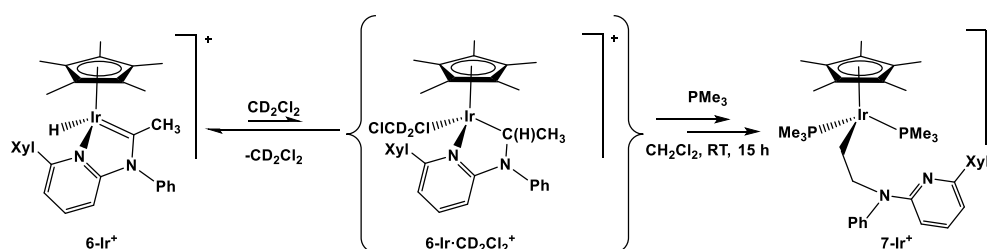
Scheme 4. Reaction of complex 6-Ir$^+$ with PMe$_3$.

Although the NMR properties of **7-Ir$^+$** permitted unambiguous structural identification, additional support was sought through X-ray crystallography. The ^{31}P{^{1}H} NMR spectrum contains the expected singlet with chemical shift -45.4 ppm. In the ^{1}H NMR spectrum, the two equivalent α alkyl protons, Ir—C*H*$_2$CH$_2$- appear as a multiplet centered at 1.47 ppm, as a consequence of coupling to the two β H atoms and

the two ^{31}P nuclei. Likewise, the Ir—CH$_2$C*H*$_2$- resonance is a multiplet, albeit substantially deshielded (3.67 ppm). Corresponding ^{13}C{^{1}H} resonances appear at -7.1 and 56.0 ppm, with two- and three- bond coupling to the ^{31}P nuclei of 7 and 5 Hz, respectively.

Figure 5 presents an ORTEP perspective view of the molecular structure of complex **7-Ir$^+$**. As for related complexes, the coordination of the C$_5$Me$_5$ ring is fairly symmetrical, with Ir—C distances spanning the rather narrow range 2.236(5)-2.281(4) Å. The two Ir—P bonds have similar distances which are indistinguishable within experimental error (2.2734(12) and 2.2854(13) Å, and the σ iridium-carbon bond to C21 has a length of 2.140(4) Å.
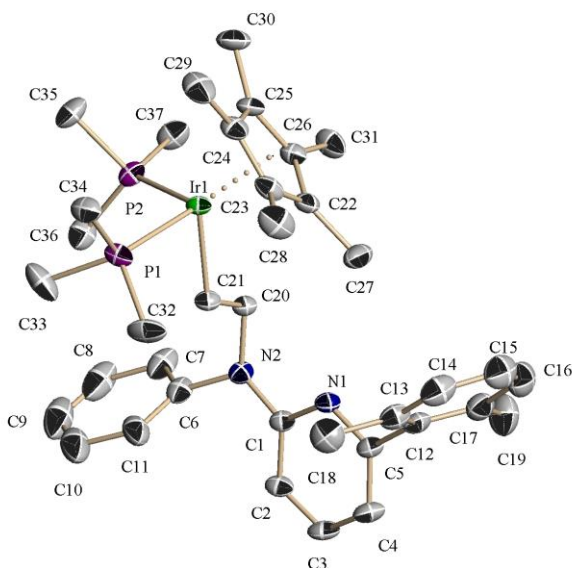

Figure 5. X-ray structure of complex **7-Ir$^+$** (30% ellipsoids, H atoms and anion BAr$_F^-$ omitted for clarity). Selected bond lengths (Angstroms) and angles (degrees): Ir(1)–C(21) 2.140(4), Ir(1)–C(23) 2.246(5), Ir(1)–P(1) 2.2854(13), Ir(1)–C(24) 2.278(4), Ir(1)–P(2) 2.2734(12), Ir(1)–C(25) 2.281(4), C(20)–C(21) 1.534(6), Ir(1)–C(26) 2.236(5), Ir(1)–C(22) 2.267(5), P(1)-Ir(1)-P(2) 96.22(5), Ir(1)-C(21)-C(20) 117.6(3), P(1)-Ir(1)-C(21) 83.23(13), C(21)-C(20)-N(2) 112.0(4), C(21)-Ir(1)-P(2) 89.86(13).

Similarly to the iridium cation **3-Ir**[+] the rhodium analogue **3-Rh**[+] reacted instantly with ethylene. Rather disappointingly, as discussed below a very complex mixture of compounds was observed even at low temperature (-80 ℃), limiting considerably the synthetic and mechanistic utility of this reaction. Nevertheless, some useful information could be collected and will be briefly discussed. Mixing the rhodium complex **3-Rh**[+] and C_2H_4 at 0 ℃ caused immediate consumption of the metal reagent and generation of a complex manifold of products. The ^{1}H NMR spectrum of this mixture (Figure S24) contained discernible η^5-C_5Me_5 resonances between 1.2 and 1.6 ppm for at least four rhodium compounds. One of these species originated in addition a significantly shielded doublet resonance at -0.21 ppm ($^3J_{HH} \sim 6$ Hz). Keeping in mind the results already described for the analogous iridium system and by similarity with NMR data reported in the literature for the Rh···CH_3 δ-agostic bond found in the cationic Rh(III) $[(\eta^5$-$C_5Me_5)Rh(H)(PMeXyl_2)]^+$ complex (δ -0.02 ppm),[23] it can be proposed that one of the components of the said mixture contains a chelating secondary alkyl-pyridine ligand in which the Rh—C(H)MeCH$_2$N- unit is further engaged in a β-agostic methyl interaction (structure **5-Rh**[+] in Figure 6). In one of the many crystallization attempts effected, a few single crystals were obtained and while no full NMR characterization of the pure isolated complex could be accomplished, its molecular structure was disclosed by a single-crystal X-ray study. The ORTEP view of the molecules of **5-Rh**[+] is shown on the right-hand-side of Figure 6 and provides unequivocal proof for a C—N coupling reaction alike that described for the analogous iridium complex. As can be seen, the complex contained a five-membered C^N metallacycle consisting of secondary-alkyl and pyridine ligands, with the Rh(III) center being additionally decorated by a β-agostic interaction, helping to achieve an 18-electron count. Despite the uncertainties in determining the positions of H atoms by X-ray diffraction, the metric parameters for the Rh—CH(CH_3)- linkage are in agreement with the existence in the solid state of a Rh···CH_3 β-agostic interaction. The Rh1—C31 distance is relatively short at 2.362(7) Å, and both the Rh1—H(C31) distance of 1.937 Å and the Rh1—H—C31 angle of 103.15º are well in the 1.8-2.3 Å and 90-140º ranges commonly found, for such bonds.[24] Although the limited experimental evidence obtained for the reaction of **3-Rh**[+] and C_2H_4 prevents a proper discussion of these results, it should be noted that observation of the agostic structure for **5-Rh**[+] is in line with common knowledge that agostic bonds are favored for cationic complexes of first-

and second-row metals, whereas their third-row counterparts prefer the isomeric hydride formulation.[25,26] Computational data discussed next are also in accordance with these observations.
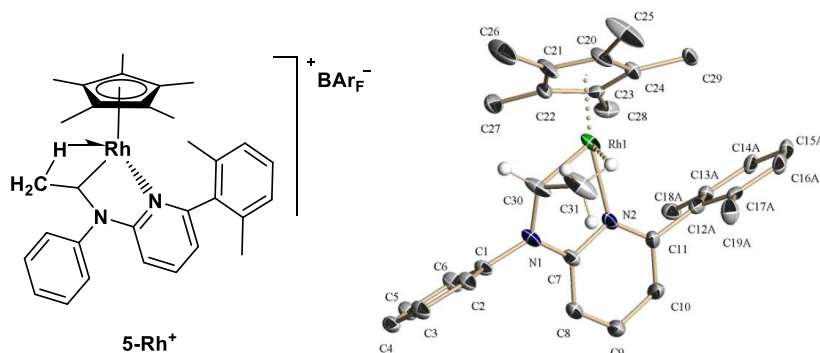

Figure 6. X-ray structure of complex **5-Rh$^+$** (30% ellipsoids, H atoms and BAr$_F^-$ anion omitted for clarity). Selected bond lengths (Angstroms) and angles (degrees): Rh(1)–C(30) 2.009(7), Rh(1)–C(31) 2.362(7), Rh(1)–C(21) 2.153(9), Rh(1)–H(31C) 1.9373, Rh(1)–C(22) 2.123(8), Rh(1)–N(2) 2.153(5), Rh(1)–C(23) 2.179(6), N(1)–C(30) 1.431(8), Rh(1)–C(24) 2.259(6), Rh(1)–C(20) 2.188(7), C(30)-Rh(1)-N(2) 78.2(3), C(7)-N(1)-C(30) 118.3(5), C(30)-Rh(1)-H(31C) 63.9, N(1)-C(7)-N(2) 114.5(5), N(2)-Rh(1)-H(31C) 88.5, N(1)-C(30)-Rh(1) 111.5(4), C(7)-N(2)-Rh(1) 112.3(4), C(31)-H(31C)-Rh(1) 103.15.

The structure presented in Figure 6 for complex **5-Rh$^+$** may be viewed as a model for the intermediate preceding β-H elimination to furnish an isomeric hydride-alkene product. DFT calculations revealed that while an energy barrier of only 7.8 kcal·mol^{-1} needs be overcome (Figure 7), the β-H elimination reaction is thermodynamically uphill by 5.1 kcal·mol^{-1}. Moreover, in a different conformation, **5´-Rh$^+$**, which is just 2.2 kcal·mol^{-1} above the observed structure (Figure 7), α-H elimination to yield a hydride alkylidene complex analogous to **6-Ir$^+$**, thereby containing an N-stabilized carbene ligand, could occur with an affordable energy barrier of 6.4 kcal·mol^{-1}. Notwithstanding, the purported hydride carbene rhodium complex would be thermodynamically unstable in comparison with the isolated complex **5-Rh$^+$** and also with conformation **5´-Rh$^+$**.
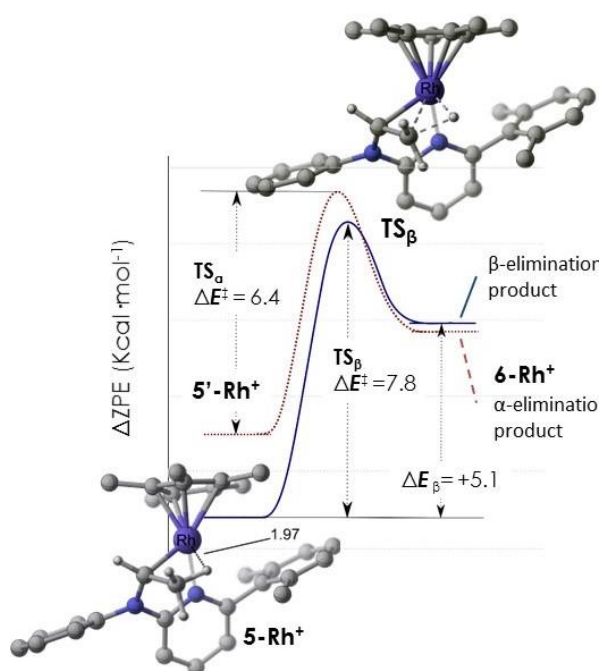
Figure 7. Calculated energy of energy profiles for β- (solid line) and α-H (dotted line) elimination from the appropriate conformer of **5-Rh⁺**. Optimized geometries of **5-Rh⁺** and the transition state for β-H elimination. Zero Point corrected Potential Energies calculated in dichloromethane relative to the ethylene adduct.

Computational studies on the reaction of 3-Ir⁺ with C₂H₄. The nature of the carbene ligand of product **6-Ir⁺**, which besides the N—heteroatom features a methyl substituent at the carbene carbon, denotes that **6-Ir⁺** forms by α-H elimination from a chelating pyridine-alkyl ligand alike intermediate **6-Ir·ClCD₂Cl⁺** of Scheme 4 (*vide supra*). Hence, we initially envisioned a reaction route implicating a highly reactive cationic iridium ethylidene group, [Ir]=C(H)Me, with a structure akin to **A** in Figure 8, formally arising from an iridium promoted tautomerization of coordinated C₂H₄ in **5-Ir⁺**. The said prototropism could be followed by ethylidene migratory insertion into the Ir—N$_{amido}$ bond, yielding an unsaturated branched alkyl (**B** in Figure 8) which would convert into the product by α-H elimination.

A direct 1,2-shift within the coordinated ethylene molecule could account for the ethylene-to-ethylidene tautomerism, similarly to well-established metal promoted acetylene-to-vinylidene rearrangements.[27] While the C₂H₄ and C₂H₂ tautomerizations are strongly endothermic (*ca.* 80 and 45 kcal·mol⁻¹ for the former[21a] and the latter,[27]

15

respectively), the relative energies of the corresponding π-hydrocarbon and carbene isomers change dramatically in the coordination sphere of transition metals. In many reported examples, the driving force for the isomerization is largely associated with the strong electronic interaction between the metal and the carbene type ligand.[21a,27c] Indeed, our computational studies evince that the ethylidene intermediate **A** (Figures 8 and S45-46 in the SI) is only 12.5 kcal·mol^{-1} less stable than its olefin isomer **5-Ir$^+$**, and moreover than the consequent N—C bond formation resulting from nucleophilic attack of the Ir—N$_{amido}$ bond to the Ir=C(H)Me one, needs overcoming a barrier of just 12.1 kcal·mol^{-1}. Nevertheless, all attempts to model the direct 1,2-H shift within the Ir—C$_2$H$_4$ linkage of **5-Ir$^+$** gave unrealistically high energy barriers which justified ruling out this path.

As a variant to the direct 1,2-H shift we analyzed a shuttling function[28-30] of the Ir—N$_{amido}$ unit, abstracting first an olefinic hydrogen atom to yield an iridium-vinyl **C** (Figure 8 and S46) and then protonating the β-C atom of the ligated vinyl to produce **A**. Once again, whereas structure **C** is energetically feasible, laying in energy 10.5 kcal·mol^{-1} above **5-Ir$^+$**, conversion of the latter into the former requires surmounting a barrier of *ca.* 32.6 kcal·mol^{-1}, which is at odds with experimental conditions. Aside from that, this barrier is significantly higher than the topmost step in the migratory insertion mechanism discussed next.
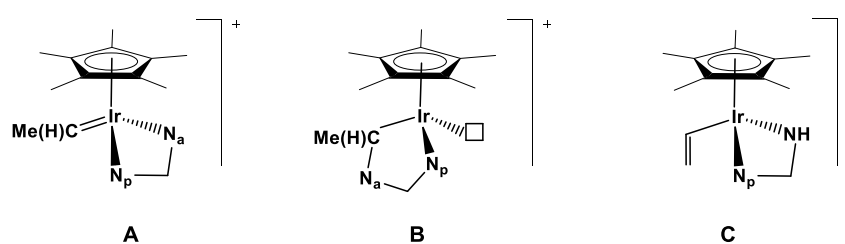

Figure 8. Possible intermediates for an ethylidene route to complex **6-Ir$^+$**.

Scheme 5 summarizes the mechanistic route that implies migratory insertion of ethylene into the Ir—N$_{amido}$ bond of complex **5-Ir$^+$**. Figures 9 and 10 display relevant information on key steps of the calculated energy profile. The migratory insertion is

relatively facile, an energy barrier $\Delta E^{\neq} = 22.1$ kcal·mol^{-1} needs be surpassed to afford an intermediate **D** (Scheme 5 and Figure 9) that is in actuality isoenergetic with the initial pyridylamido ethylene complex **5-Ir$^+$**. The proposed intermediate exhibits a six-member chelating moiety consisting of pyridine and alkyl ends and becomes stabilized by formation of a dative covalent bond between iridium and the former N$_{amido}$ function, now converted into an NH amino one (Ir—N$_{amino}$ distance of 2.27 Å, *vs*. 2.15 Å for Ir—N$_{pyridine}$).
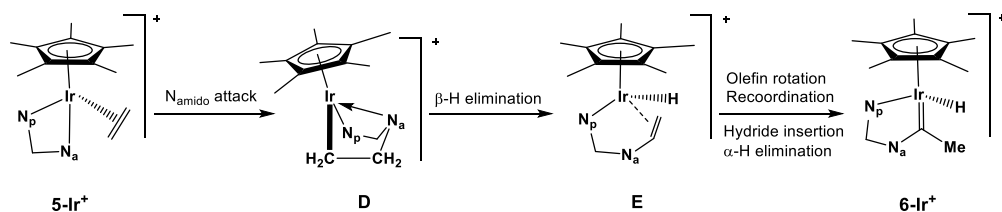
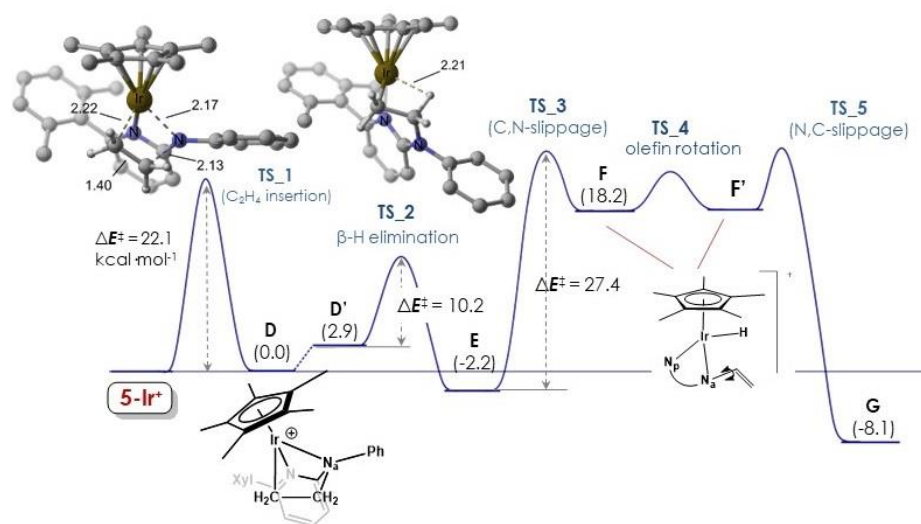**Scheme 5. Key intermediates in the proposed migratory insertion leading to complex 6-Ir$^+$.**

Figure 9. Energy profile including the initial steps of the migratory insertion path. Zero Point corrected Potential Energies calculated in dichloromethane relative to the ethylene adduct.

17

Elongation of the Ir—N_{amino} distance of **D** to 3.00 Å results in a conformation, **D´** (Figure 9 and S47; ΔE^0 = 2.9 kcal·mol^{-1}), from which β-H elimination can take place easily ($\Delta E^{\neq}$ = 10.3 kcal·mol^{-1}). As already anticipated, formation of **6-Ir$^+$** from the resulting species, **E** (Figure 9, ΔE^0 = -2.2 kcal·mol^{-1}) requires a change of the coordinated face of the prochiral olefin. If this process is assisted by the N_{amino} functionality, the barrier for Ir—C to Ir—N *slippage* required to allow olefin dissociation to yield **F** (Figure 9) turned out as rate limiting ($\Delta E^{\neq}$ = 27.4 kcal·mol^{-1} from **E**), but it is still more accessible than the hydrogen abstraction from C_2H_4 discussed previously. As expected, rotation of the N_a—CH=CH$_2$ bond and re-coordination of the olefin through the other face to give the hydride-olefin species **G**, *i.e.* stereoisomer of **E**, are fast, and the latter step is also very exothermic (ΔE^0 = -26.3 kcal·mol^{-1} from **F**). From this point, formation of **6-Ir$^+$** requires hydride insertion and α-elimination from **B**, both steps having accessible energy barriers. Notice that α-H elimination from **B** appears faster than β-H elimination from **B´**, and more significantly, that the energy return from the former process to produce the carbene product **6-Ir$^+$** is larger than that associated with β-H elimination from **B´** to generate the unobserved hydride olefin tautomer **G**. It is worth recalling that although H$_\beta$ elimination is usually faster than H$_\alpha$ elimination when the two reactions can compete, examples are known where the opposite is true. Specifically, in sterically congested systems in which the M-C$_\alpha$-C$_\beta$-H atoms cannot readily adopt the required *syn* approximately coplanar arrangement,[31] formation of α-agostic bonds and α-H elimination may become faster than corresponding processes for β-H atoms.[21,23,32]
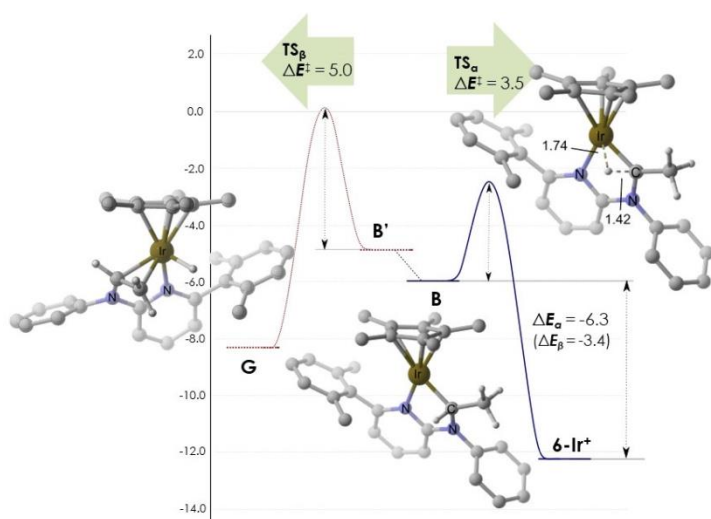
Figure 10. DFT calculated energy profiles for α- (solid line) and β-H (dotted line) elimination from the appropriate conformer, **B** or **B´**, and optimized geometries of relevant species involved in α-H elimination. Zero Point corrected Potential Energies calculated in dichloromethane relative to **5-Ir⁺**.

Reactions of iridium and rhodium complexes 3-M⁺ with H₂. The title reactions proceeded much as expected on the basis of previous studies.[1,2] Briefly, we recall that catalytic amounts of H₂ promote reversible isomerization of the aminopyridinate ligand between classical κ^2-*N,N´*-bidentate binding, to an unprecedented κ-*N*,η^3-pseudo-allyl-coordination, as depicted in Scheme 6 (left part) for **3-Ir⁺** and **8-Ir⁺**. The isomerization implies reversible formation and cleavage of H—H, C—H and N—H bonds. Experimental and computational studies[1,2] support the mechanistic pathway presented in Scheme S2 (see the SI).

Treatment of **3-Ir⁺** with an excess of H₂ yielded the known binuclear hydride $\{[(\eta^5\text{-}C_5Me_5)Ir]_2(\mu\text{-H})_3\}^{+,33}$ whereas catalytic amounts of H₂ (*ca*. 2 mol%) promoted isomerization of the Ap ligand of **3-Ir⁺** to the η^3-benzylic-pyridine coordination found in the new complex **8-Ir⁺** (Scheme 6). The prototropic rearrangement resulted in a **3-Ir⁺**:**8-Ir⁺** equilibrium mixture of *ca*. 1:3, with a half-life, $t_{1/2}$, of about 1.2 h (20 ℃, CD₂Cl₂). Under similar experimental conditions and a H₂ concentration of 1.6 mol%, the analogous complex in which the N_{amido} aryl substituent was 2,6-Pr$^i_2$C₆H₃ instead of C₆H₅, equilibrated with $t_{1/2}$ = 9.1 h. This difference in the rate of almost one order of magnitude clearly reflects the importance of the steric effects of the N_{amido} aryl substituent in the reactivity of complexes alike **3-M⁺**.

19
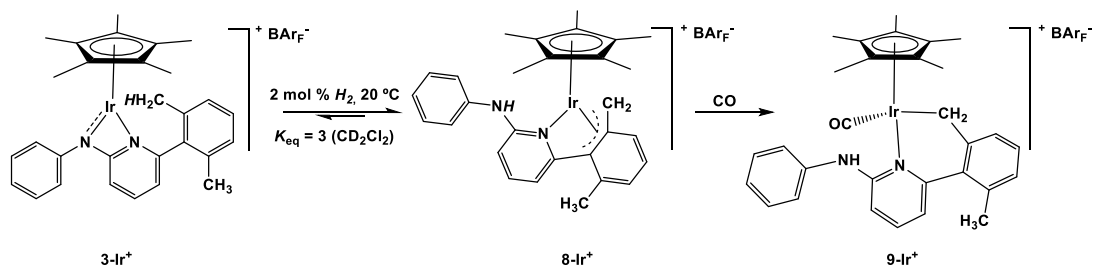
Scheme 6. The H$_2$-catalyzed isomerization of the aminopyridinate ligand of 3-Ir$^+$ and the formation of carbonyl complex 9-Ir$^+$.

Spectroscopic data for **8-Ir$^+$** are similar to those recorded for related complexes.[1] The N*H* resonance is, however, slightly deshielded relative to values found for analogous complexes (6.25 *vs. ca.* 5.94 ppm).[1] It is tempting to associate this shift with the relatively short Ir···HN contact of 2.89 Å observed in the solid state molecular structure of the complex (Figure 11, left). Nonetheless, recalling that hydrogen positions determined by X-ray studies are not particularly accurate and that the Ir···HN contact in **8-Ir$^+$** is longer than known Ir···HC agostic bonds,[34] such a NH···Ir interaction must be very weak and most probably meaningless in terms of electron density sharing. Close similarity of **8-Ir$^+$** to earlier analogues was also found in the reaction with CO (Scheme 6) that occurred with η^3-to-η^1 benzyl coordination change and formation of carbonyl complex **9-Ir$^+$**. The latter exhibits ῡ(CO) at 2029 cm^{-1} (see Experimental Section).
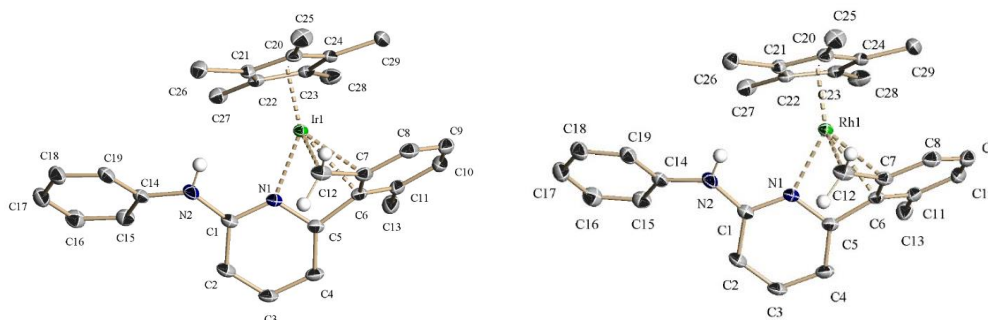

Figure 11. X-ray structures of complexes **8-Ir$^+$** (left) and **8-Rh$^+$** (right) (30% ellipsoids, H atoms and anion BAr$_F^-$ omitted for clarity). Selected bond lengths (Angstroms) and angles (degrees) for **[8-Ir]BAr$_F$**: Ir(1)–N(1) 2.086(3), C(10)–C(11) 1.378(6), Ir(1)–C(6) 2.387(4), C(6)–C(11) 1.423(6), Ir(1)–C(7) 2.252(4), Ir(1)–C(20) 2.170(3), Ir(1)–C(12) 2.118(4), Ir(1)–C(21) 2.153(4), C(6)–C(7) 1.449(5), Ir(1)–C(22) 2.202(3), C(7)–C(12) 1.449(6), Ir(1)–C(23) 2.225(4), C(7)–C(8) 1.423(6), Ir(1)–C(24) 2.187(4), C(8)–C(9) 1.355(7), Ir(1)–H(2N) 2.891, C(9)–C(10) 1.408(6), N(1)-Ir(1)-C(6) 62.04(12), N(1)-Ir(1)-C(12) 80.11(14), C(7)-Ir(1)-C(6) 36.27(13), N(1)-C(5)-C(6) 108.5(3), C(12)-Ir(1)-C(7) 38.59(16), N(1)-C(1)-N(2) 115.1(3). Selected bond lengths (Angstroms) and angles (degrees) for **[8-Rh]BAr$_F$**: Rh(1)–N(1) 2.101(3), C(10)–C(11) 1.372(7), Rh(1)–C(6) 2.379(4), C(6)–C(11) 1.428(7), Rh(1)–C(7) 2.237(4), Rh(1)–C(20) 2.176(4),

Rh(1)–C(12) 2.124(5), Rh(1)–C(21) 2.155(4), C(6)–C(7) 1.441(6), Rh(1)–C(22) 2.191(4), C(7)–C(12) 1.437(7), Rh(1)–C(23) 2.218(4), C(7)–C(8) 1.432(7), Rh(1)–C(24) 2.174(4), C(8)–C(9) 1.350(8), Rh(1)–H(2N) 2.987, C(9)–C(10) 1.406(8), N(1)-Rh(1)-C(6) 62.43(14), N(1)-Rh(1)-C(12) 81.00(17), C(7)-Rh(1)-C(6) 36.21(16), N(1)-C(5)-C(6) 110.3(4), C(12)-Rh(1)-C(7) 38.37(19), N(1)-C(1)-N(2) 115.4(4).

Monitoring the progress of the reaction of **3-Ir**[+] with an excess of H_2 (1 bar) allowed observation of a hydride intermediate in high spectroscopic yield (-6.32 ppm, relative intensity 1 H). Isolation of this complex proved unattainable, for in the presence of H_2 converted quickly into $\{[(\eta^5\text{-}C_5Me_5)Ir]_2(\mu\text{-}H)_3\}^+$, whereas in the absence of this gas it yielded, also rapidly, the 1:3 equilibrium mixture of **3-Ir**[+] and **8-Ir**[+]. No N*H* resonance or other relevant NMR data could, however, be assigned with certainty to this intermediate, which refrains us from putting forward a definitive structural proposal.

Complex **3-Rh**[+] also reacted quickly with 1 bar of H_2 at room temperature though a complex mixture compounds was obtained including $\{[(\eta^5\text{-}C_5Me_5)Rh]_2(\mu\text{-}Cl)_3\}^+$.[35] At least two $\eta^4\text{-}C_5Me_5H$-containing complexes[36] were detected by NMR, the latter possibly related to those that were fully characterized for bulkier aminopyridinate ligands.[2] Likewise, the η^3-benzyl complex **8-Rh**[+] resulting from the H_2-catalyzed isomerization of the aminopyridinate ligand was detected in the crude reaction mixture. The latter complex was subsequently generated in moderate quantities (*ca*. 50% spectroscopic yield) using sub-stoichiometric amounts of H_2 (60 mol%). Complex **8-Rh**[+] was fully characterized. Its X-ray molecular structure is presented in Figue 9 (right-hand-side) and features metrical parameters for the metal-η^3-benzyl moiety similar to those of analogous complexes.

CONCLUSIONS

This work demonstrated that the M—N_{amido} bond of the pyridylamido complexes $[(\eta^5\text{-}C_5Me_5)M(N^\wedge N)]^+$ (**3-M$^+$**), activates readily CO, C_2H_4 and H_2. Whereas CO and C_2H_4 brought about migratory insertion reactivity, H_2 catalyzed a prototropic rearrangement within the Ap ligand, whereby remote transfer of a benzylic hydrogen from the pyridine xylyl substituent to the N_{amido} atom occurred readily in a reversible fashion.

Only **3-Rh$^+$** experienced CO migratory insertion into the Rh—N_{amido} bond, expanding the original four-member $\overline{Rh\text{-}N\text{-}C\text{-}N}$ ring to a five-membered pyridine-carbamoyl rhodacycle, whereas for iridium the stronger M—N_{amido} bond decisively retarded the migratory CO insertion step affording the carbonyl adduct **4-Ir$^+$** as the only observable product. In contrast, **3-Ir$^+$** formed easily, albeit reversibly, the ethylene adduct **5-Ir$^+$**, which rearranged spontaneously by migratory insertion, the end product of the reaction being the hydride N-substituted alkylidene complex **6-Ir$^+$**. DFT studies reinforced a mechanistic scheme encompassing irreversible C—N bond formation followed by reversible β- and α-H elimination reactions.

EXPERIMENTAL SECTION

General Procedures. Microanalyses were performed by the Microanalytical Service of the Instituto de Investigaciones Químicas (Sevilla, Spain). Infrared spectra were obtained from Bruker Vector 22 spectrometer. The mass spectra were obtained at the Mass Spectroscopy Service of the University of Sevilla. The NMR instruments were Bruker DRX-500, DRX-400 and DPX-300 spectrometers. Spectra were referenced to external $SiMe_4$ (δ 0 ppm) using the residual protio solvent peaks as internal standards (^{1}H NMR experiments) or the characteristic resonances of the solvent nuclei (^{13}C NMR experiments). Spectral assignments were made by routine one- and two-dimensional NMR experiments where appropriate. All manipulations were performed under dry, oxygen-free dinitrogen, following conventional Schlenk techniques. The crystal structures were determined in a Bruker-Nonius, X8Kappa diffractometer. Metal complexes $[Cp^*IrCl_2]_2$,[37] $[Cp^*RhCl_2]_2$[37] as well as $NaBAr_F$[38] were prepared as

previously described. The lithium salt of the aminopyridinate ligand employed in this work was prepared according to published procedures.[1b] The ^{1}H and ^{13}C{^{1}H} NMR spectral data for the BAr$_F$ anion (BAr$_F$ = B[3,5-(CF$_3$)$_2$C$_6$H$_3$)$_4$]) in CD$_2$Cl$_2$ are identical for all complexes and therefore are not repeated below. ^{1}H NMR: δ 7.75 (s, 8 H, *o*-Ar), 7.58 (s, 4 H, *p*-Ar); ^{13}C{^{1}H} NMR: δ 162.1 (q, $^1J_{CB}$ = 37 Hz, *ipso*-Ar), 135.3 (*o*-Ar), 129.2 (q, $^2J_{CF}$ = 31 Hz, *m*-Ar), 124.9 (q, $^1J_{CF}$ = 273 Hz, CF$_3$), 117.8 (*p*-Ar).

Compound 2-Ir. A toluene solution of LiAp (1g, 3.57 mmol; 35 mL) at -50 ºC was added to a suspension of [Cp*IrCl$_2$]$_2$ (1.4 g, 1.78 mmol) in toluene at -50 ºC. The resulting mixture was stirred while allowing to warm to room temperature, and stirred further for a period of 14 h. The solution was filtered through celite and the solvent removed under reduced pressure. ^{1}H NMR analysis of the crude reaction mixture showed only the presence of **2-Ir**, which was crystallized from CH$_2$Cl$_2$-hexane mixtures at -23 ºC. Yield: 1.55 g (68%). ^{1}H NMR (C$_6$D$_6$, 25 ºC): δ = 7.54, 7.26, 6.96 (d, t, t, 2:2:1, $^3J_{HH}$ ~ 7.5 Hz, 5 CH$_{Ph}$), 7.06, 7.00, 6.96 (t, br d, br d, 1 H each, $^3J_{HH}$ ~ 7.5 Hz, 3 CH$_{Xyl}$), 6.80 (t, 1 H, $^3J_{HH}$ = 7.9 Hz, 1 CH$_{Pyr}$), 6.35 (d, 1 H, $^3J_{HH}$ = 8.7 Hz, 1 CH$_{Pyr}$), 5.81 (d, 1 H, $^3J_{HH}$ = 7.0 Hz, 1 CH$_{Pyr}$), 2.66, 2.13 (s, 3 H each, 2 Me$_{Xyl}$), 1.16 (s, 15 H, 5 Me$_{Cp*}$); ^{13}C{^{1}H} NMR (C$_6$D$_6$, 25 ºC): δ = 171.2, 156.4 (C$_{q-Pyr}$), 146.3 (C$_{q-Ph}$), 140.0, 139.0, 136.7 (C$_{q-Xyl}$), 137.3, 108.9, 106.5 (CH$_{Pyr}$), 129.0, 124.1, 122.1 (2:2:1, CH$_{Ph}$), 128.5, 128.3, 127.0 (CH$_{Xyl}$), 84.0 (C$_{q-Cp*}$), 21.9, 20.8 (Me$_{Xyl}$), 9.1 (Me$_{Cp*}$); elemental analysis calcd (%) for C$_{29}$H$_{32}$ClIrN$_2$: C, 54.7; H, 5.1; N, 4.4; found: C, 54.6; H, 5.1; N, 4.5.

Compound 2-Rh. Following the procedure described above for **2-Ir**, but using [Cp*RhCl$_2$]$_2$, compound **2-Rh** was obtained in quantitative spectroscopic yield and was crystallized from CH$_2$Cl$_2$-hexane mixtures at -23 ºC. Yield: 0.8 g (64%). ^{1}H NMR (C$_6$D$_6$, 25 ºC): δ = 7.65, 7.28 (d, t, 1:1, $^3J_{HH}$ ~ 7.5 Hz, 4 CH$_{Ph}$), 7.04 (m, 3 H, 1 CH$_{Ph}$ + 2 CH$_{Xyl}$), 6.95 (d, 1 H, $^3J_{HH}$ ~ 7.5 Hz, 1 CH$_{Xyl}$), 6.79, 6.33, 5.81 (m, d, d, 1 H each, $^3J_{HH}$ ~ 7.5 Hz, 3 CH$_{Pyr}$), 2.70, 2.18 (s, 3 H each, 2 Me$_{Xyl}$), 1.10 (s, 15 H, 5 Me$_{Cp*}$); ^{13}C{^{1}H} NMR (C$_6$D$_6$, 25 ºC): δ = 170.4, 158.1 (C$_{q-Pyr}$), 147.9 (C$_{q-Ph}$), 140.4, 139.2, 136.6 (C$_{q-Xyl}$), 137.4, 108.8, 105.0 (CH$_{Pyr}$), 129.1, 125.3, 122.2 (2:2:1, CH$_{Ph}$), 128.2, 127.9, 126.8 (CH$_{Xyl}$), 91.9 (d, $^1J_{CRh}$ = 8 Hz, C$_{q-Cp*}$), 21.9, 20.8 (Me$_{Xyl}$), 8.8 (Me$_{Cp*}$); elemental analysis for C$_{29}$H$_{32}$ClRhN$_2$: C, 63.7; H, 5.9; N, 5.1; found: C, 63.7; H, 6.0; N, 5.2.

Compound [3-Ir]BAr$_F$. To a solution of **2-Ir** (1.5 g, 2.36 mmol) in CH$_2$Cl$_2$ (40 mL), NaBAr$_F$ (2.1 g, 2.36 mmol) in CH$_2$Cl$_2$ (25 mL) was added. Inmmediately the solution turned from orange to dark grey as a consequence of the formation of the cationic complex. The resulting mixture was filtered through celite, evaporated to dryness and the residue washed with pentane, to yield quantitatively the desired product. An analytically pure sample was obtained by crystallization from solutions in hexane:ether mixtures at -23 ºC. Yield: 2.8 g (80%). ^{1}H NMR (CD$_2$Cl$_2$, 25 ºC): δ = δ 7.65 (t, 1 H, $^3J_{HH}$ = 8.0 Hz, 1 CH$_{Pyr}$), 7.44 (t, 2 H, $^3J_{HH}$ = 7.7 Hz, 2 CH$_{Ph}$), 7.33 (t, 1 H, $^3J_{HH}$ = 7.6 Hz, 1 CH$_{Xyl}$), 7.19 (m, 3 H, 1 CH$_{Ph}$ + 2 CH$_{Xyl}$), 7.08 (d, 2 H, $^3J_{HH}$ = 7.8 Hz, 2 CH$_{Ph}$), 6.36, 5.89 (br s., 1 H each, 2 CH$_{Pyr}$), 2.25 (s, 6 H, 2 Me$_{Xyl}$), 1.31 (s, 15 H, 5 Me$_{Cp*}$).^{13}C{^{1}H} NMR (CD$_2$Cl$_2$, 25 ºC): δ = δ 178.3, 155.8 (br, C$_{q-Pyr}$), 145.1, 119.5, 104.9 (br, CH$_{Pyr}$), 143.5 (br, C$_{q-Ph}$), 136.8, 135.9 (1:2, C$_{q-Xyl}$), 130.5, 128.6 (1:2, CH$_{Xyl}$), 129.9, 128.1, 123.1 (br, 2:1:2, CH$_{Ph}$), 88.1 (C$_{q-Cp*}$), 20.6 (Me$_{Xyl}$), 10.2 (Me$_{Cp*}$); HRMS (FAB): m/z calcd for C$_{29}$H$_{32}$N$_2$Ir [M]$^+$: 601.2195; found: 601.2202.

Compound [3-Rh]BAr$_F$. Following the procedure described above for **[3-Ir]BAr$_F$**, but using **2-Rh**, complex **[3-Rh]BAr$_F$** was obtained in quantitative spectroscopic yield. ^{1}H NMR (CD$_2$Cl$_2$, 25 ºC): δ = 7.44 (m, 3 H, 1 CH$_{Pyr}$ + 2 CH$_{Ph}$), 7.36, 7.26 (t, d, 1:2, $^3J_{HH}$ ~ 7.5 Hz, 3 CH$_{Xyl}$), 7.22 (m, 3 H, 3 CH$_{Ph}$), 6.33, 6.07 (d, 1 H each, $^3J_{HH}$ ~ 7.5 Hz, 2 CH$_{Pyr}$), 2.32 (s, 6 H, 2 Me$_{Xyl}$), 1.34 (s, 15 H, 5 Me$_{Cp*}$); ^{13}C{^{1}H} NMR (CD$_2$Cl$_2$, 25 ºC): δ 175.3, 157.5 (C$_{q-Pyr}$), 145.6 (C$_{q-Ph}$), 143.5, 116.5, 104.2 (CH$_{Pyr}$), 137.9, 136.4 (1:2, C$_{q-Xyl}$), 130.2, 123.2 (2:3, CH$_{Ph}$), 130.1, 128.6 (1:2, CH$_{Xyl}$), 95.2 (d, $^1J_{CRh}$ ~ 8 Hz, C$_{q-Cp*}$), 20.8 (Me$_{Xyl}$), 9.6 (Me$_{Cp*}$); HRMS (FAB): m/z calcd for C$_{29}$H$_{32}$N$_2$Rh [M]$^+$: 511.1621; found 511.1619.

Compound [4-Ir]BAr$_F$. CO (g) was bubbled through a solution of compound **[3-Ir]BAr$_F$** (0.2 g, 0.14 mmoles) in CH$_2$Cl$_2$ (5 mL) at room temperature for 5 min. During this period of time the color of the solution changed from dark grey to bright orange. The resulting mixture was stirred for 10 minutes and the volatiles were then removed under reduced pressure. ^{1}H NMR analysis of the crude product revealed quantitative

conversion into the desired complex, which was crystallized from CH_2Cl_2-pentane mixtures at -23 ºC. Yield: 60%. IR (Nujol): $\nu(CO)$ 2048 cm^{-1}; ^1H NMR (CD$_2$Cl$_2$, 25 ºC): δ = 7.59 (m, 1 H, 1 CH$_{Pyr}$), 7.40 (t, 2 H, $^3J_{HH}$ = 7.7 Hz, 2 CH$_{Ph}$), 7.33 (t, 1 H, $^3J_{HH}$ = 7.6 Hz, 1 CH$_{Xyl}$), 7.19 (m, 3 H, 2 CH$_{Xyl}$ + 1 CH$_{Ph}$), 7.02 (d, 2 H, $^3J_{HH}$ = 7.8 Hz, 2 CH$_{Ph}$), 6.53 (d, 1 H, $^3J_{HH}$ = 8.8 Hz, 1 CH$_{Pyr}$), 6.42 (d, 1 H, $^3J_{HH}$ = 7.3 Hz, 1 CH$_{Pyr}$), 2.19 (s, 6 H, 2 Me$_{Xyl}$), 1.59 (s, 15 H, 5 Me$_{Cp*}$); $^{13}C\{^1H\}$ NMR (CD$_2$Cl$_2$, 25 ºC): δ = 174.4, 157.0 (C$_{q-Pyr}$), 168.8 (Ir-CO), 141.9 (C$_{q-Ph}$), 140.8, 112.8, 107.9 (CH$_{Pyr}$), 137.1, 136.3, 136.2 (C$_{q-Xyl}$), 130.3, 125.1, 123.7 (2:1:2, CH$_{Ph}$), 130.3, 128.7, 128.5 (CH$_{Xyl}$), 101.6 (C$_{q-Cp*}$), 21.3, 20.4 (Me$_{Xyl}$), 9.3 (Me$_{Cp*}$); elemental analysis for C$_{62}$H$_{44}$BF$_{24}$IrN$_2$O: C, 49.9; H, 3.0; N, 1.9; found: C, 49.6; H, 3.0; N, 1.8.

Compound [4-Rh]BAr$_F$. Following the procedure described above for **[4-Ir]BAr$_F$**, but using **[3-Rh]BAr$_F$**, compound **[4-Rh]BAr$_F$** was obtained in quantitative spectroscopic yield (the color of the solution changed from dark brown to orange-colored) and was crystallized from CH_2Cl_2-pentane mixtures at -23 ºC. Yield: 50%. IR (Nujol): $\nu(CO)$ 2077 cm^{-1}, $\nu(CO_{amide})$ 1687 cm^{-1}; ^1H NMR (CD$_2$Cl$_2$, 25 ºC): δ = 7.77, 7.00, 6.66 (t, d, d, 1 H each, $^3J_{HH}$ ~ 7.5 Hz, 3 CH$_{Pyr}$), 7.63, 7.23 (m, br d, 3:1, $^3J_{HH}$ ~ 7.5 Hz, 4 CH$_{Ph}$), 7.40 (t, 1 H, $^3J_{HH}$ ~ 7.5 Hz, 1 CH$_{Xyl}$), 7.28 (m, 3 H, 2CH$_{Xyl}$ + 1 CH$_{Ph}$), 2.20, 2.12 (s, 3 H each, 2 Me$_{Xyl}$), 1.59 (s, 15 H, 5 Me$_{Cp*}$); $^{13}C\{^1H\}$ NMR (CD$_2$Cl$_2$, 25 ºC): δ = 189.3, 187.1 (d, $^1J_{CRh}$ = 30 Hz, $^1J_{CRh}$ = 76 Hz, Rh-CON and Rh-CO, resp.), 162.7, 158.7 (C$_{q-Pyr}$), 141.4, 123.4, 111.2 (CH$_{Pyr}$), 138.7, 137.2, 137.0 (C$_{q-Xyl}$), 136.5 (C$_{q-Ph}$), 131.3, 131.2, 130.8, 129.3, 129.0 (CH$_{Ph}$), 130.6, 129.4 (1: 2, CH$_{Xyl}$), 109.3 (d, $^1J_{CRh}$ = 5 Hz, C$_{q-Cp*}$), 22.3, 21.7 (Me$_{Xyl}$), 9.5 (Me$_{Cp*}$); elemental analysis for C$_{63}$H$_{44}$BF$_{24}$N$_2$O$_2$Rh: C, 52.9; H, 3.1; N, 2.0; found: C, 53.3; H, 3.2; N, 1.8; HRMS (FAB): m/z calcd for C$_{31}$H$_{32}$N$_2$O$_2$Rh [M]$^+$: 567.1519; found: 567.1503.

Compound [5-Ir]BAr$_F$. C$_2$H$_4$ (g) was bubbled through a solution of compound **[3-Ir]BAr$_F$** (0.02 g, 0.014 mmoles) in CH$_2$Cl$_2$ (3 mL) in a Young NMR tube for 3 min. During this period of time the color of the solution changed from black to orange. ^1H NMR analysis of the crude product revealed quantitative conversion into complex **[5-**

Ir]BAr$_F$ in admixture with free ethylene. This complex could not be isolated due to its reversion to the starting material in absence of C_2H_4 and to its evolution at room temperature to **6-Ir$^+$**. ^{1}H NMR (CD$_2$Cl$_2$, -40 °C): δ = 7.44 (t, 1 H, $^3J_{HH}$ = 8.1 Hz, 1 CH$_{Pyr}$), 7.34 (t, 2 H, $^3J_{HH}$ = 7.1 Hz, 2 CH$_{Ph}$), 7.28, 7.17 (m, 1:2, 3 CH$_{Xyl}$), 7.09 (t, 1 H, $^3J_{HH}$ = 7.4 Hz, 1 CH$_{Ph}$), 7.00 (d, 2 H, $^3J_{HH}$ = 7.9 Hz, 2 CH$_{Ph}$), 6.50 (d, 1 H, $^3J_{HH}$ = 8.9 Hz, 1 CH$_{Pyr}$), 6.24 (d, 1 H, $^3J_{HH}$ = 7.2 Hz, 1 CH$_{Pyr}$), 4.02 (br d, 4 H, $^3J_{HH}$ = 8.6 Hz, Ir-C$_2$H$_4$), 2.15, 2.06 (s, 3 H each, 2 Me$_{Xyl}$), 1.34 (s, 15 H, 5 Me$_{Cp*}$); ^{13}C{^{1}H} NMR (CD$_2$Cl$_2$, -40 °C): δ = 171.0, 156.6 (C$_{q-Pyr}$), 141.7 (C$_{q-Ph}$), 139.1, 111.4, 108.0 (CH$_{Pyr}$), 137.1, 136.3, 135.2 (C$_{q-Xyl}$), 129.5, 123.4, 122.2 (2:1:2, CH$_{Ph}$), 129.4, 128.1, 127.5 (CH$_{Xyl}$), 98.5 (C$_{q-Cp*}$), 61.7 (Ir-C$_2$H$_4$), 21.8, 20.9 (Me$_{Xyl}$), 8.5 (Me$_{Cp*}$).

Compound [6-Ir]BAr$_F$. C$_2$H$_4$ (g) was bubbled through a solution of compound **[3-Ir]BAr$_F$** (0.1 g, 0.068 mmoles) in CH$_2$Cl$_2$ (15 mL) for 3 min. The resulting mixture was stirred for 24 h. The color changed from orange to green and then the volatiles were removed under reduced pressure. Quantitative conversion into **[6-Ir]BAr$_F$** was ascertained by ^{1}H NMR, and the product was crystallized from Et$_2$O-pentane mixtures at -23 °C. Yield 78 mg (75%). IR (Nujol): ν(Ir-H) 2096 cm^{-1}; ^{1}H NMR (CD$_2$Cl$_2$, 25 °C): δ = 7.73 – 7.67 (m, 5 H, 5 CH$_{Ph}$), 7.60 (t, 1 H, $^3J_{HH}$ = 8.0 Hz, 1 CH$_{Pyr}$), 7.34 (t, 1 H, $^3J_{HH}$ = 7.7 Hz, 1 CH$_{Xyl}$), 7.25 (m, 2 H, 2 CH$_{Xyl}$), 6.93 (dd, 1 H, $^3J_{HH}$ = 7.5 Hz, $^4J_{HH}$ =1.5 Hz, 1 CH$_{Pyr}$), 6.84 (dd, 1 H, $^3J_{HH}$ = 8.5 Hz, $^4J_{HH}$ =1.5 Hz, 1 CH$_{Pyr}$), 2.69 (d, 3 H, $^4J_{HH}$ = 2.3 Hz, Ir=CMe), 2.10, 2.06 (s, 3 H each, 2 Me$_{Xyl}$), 1.65 (s, 15 H, 5 Me$_{Cp*}$), -16.42 (br s, 1 H, Ir-H); ^{13}C{^{1}H} NMR (CD$_2$Cl$_2$, 25 °C): δ = 235.9 (Ir=CMe), 165.9, 160.6 (C$_{q-Pyr}$), 139.7 (C$_{q-Ph}$), 139.4, 137.7, 137.3 (C$_{q-Xyl}$), 138.2, 124.6, 113.9 (CH$_{Pyr}$), 131.8, 131.4, 127.6 (2:1:2, CH$_{Ph}$), 130.4, 129.2 (1:2, CH$_{Xyl}$), 98.4 (C$_{q-Cp*}$), 35.4 (Ir=CMe), 21.5, 19.7

(Me$_{Xyl}$), 9.8 (Me$_{Cp*}$); elemental analysis for C$_{63}$H$_{48}$BF$_{24}$IrN$_2$: C, 50.7; H, 3.2; N, 1.9; found: C, 50.6; H, 3.5; N, 1.7.

Compound [7-Ir]BAr$_F$. To a solution of compound **[6-Ir]BAr$_F$** (0.02 g, 0.013 mmoles) in CD$_2$Cl$_2$ (0.5 mL) in a Young NMR, an excess of PMe$_3$ was added (0.05 mL, 0.5 mmol). ^{1}H NMR analysis of the crude product revealed quantitative conversion into complex **[7-Ir]BAr$_F$** after 15 h at room temperature. Free trimethylphosphine was removed under reduced pressure and compound **[7-Ir]BAr$_F$** was crystallized from CH$_2$Cl$_2$-pentane mixtures at -23 ºC. Yield: 15 mg (70%). ^{1}H NMR (CD$_2$Cl$_2$, -40 ºC): δ = 7.49, 7.31 (t, m, 2:3, $^3J_{HH}$ ~ 7.5 Hz, 3 CH$_{Ph}$), 7.35, 6.50, 6.21 (t, d, d, 1 H each, $^3J_{HH}$ ~ 7.5 Hz, 3 CH$_{Pyr}$), 7.15, 7.06 (m, 1:2, 3 CH$_{Xyl}$), 3.67 (m, 2 H, 1 IrCH$_2$C*H*$_2$), 2.09 (s, 6 H, 2 Me$_{Xyl}$), 1.62 (s, 15 H, 5 Me$_{Cp*}$), 1.47 (m, 2 H, 1 IrC*H*$_2$CH$_2$), 1.38 (d, 18 H, $^2J_{HP}$ = 9.5 Hz, 2 PMe$_3$); ^{13}C{^{1}H} NMR (CD$_2$Cl$_2$, 25 ºC): δ = 158.6, 158.3 (C$_{q\text{-}Pyr}$), 145.4 (C$_{q\text{-}Ph}$), 142.5, 136.3, 127.4 (C$_{q\text{-}Xyl}$), 131.0, 129.8 (2:3, CH$_{Ph}$), 128.1, 127.9 (1:2, CH$_{Xyl}$), 126.8, 113.4, 106.9 (CH$_{Pyr}$), 99.0 (C$_{q\text{-}Cp*}$), 56.0 (t, $^3J_{CP}$ = 5 Hz, IrCH$_2$*C*H$_2$), 20.7 (Me$_{Xyl}$), 18.1 (d, $^1J_{CP}$ = 38 Hz, PMe$_3$), 10.1 (Me$_{Cp*}$), -7.1 (t, $^3J_{CP}$ = 7 Hz, Ir*C*H$_2$CH$_2$). ^{31}P{^{1}H} NMR (160 MHz, CD$_2$Cl$_2$, 25 ºC): δ = -45.4.

Compound [8-Ir]BAr$_F$. A solution of complex **[3-Ir]BAr$_F$** (0.05 g, 0.034 mmoles) in CH$_2$Cl$_2$ (1.25 mL) was treated with H$_2$ (1 atm) and the resulting mixture was stirred for 10 min at room temperature. ^{1}H NMR analysis of the reaction mixture revealed formation of complex **[8-Ir]BAr$_F$** together with its isomer **[3-Ir]BAr$_F$** in a *ca.* 3:1 ratio. **[8-Ir]BAr$_F$** was separated by fractional crystallization from CH$_2$Cl$_2$-pentane mixtures at -23 ºC as bright orange crystals. Yield: 10 mg (22%). ^{1}H NMR (CD$_2$Cl$_2$, 25

ºC): δ = 7.71 (br s., 1 H, 1 CH_{Xyl}), 7.69 (m, 1 H, 1 CH_{Pyr}), 7.50 (t, 2 H, $^3J_{HH}$ = 7.8 Hz, 2 CH_{Ph}), 7.46 (m, 1 H, 1 CH_{Xyl}), 7.33 (t, 1 H, $^3J_{HH}$ = 7.5 Hz, 1 CH_{Ph}), 7.24 (d, 2 H, $^3J_{HH}$ = 7.8 Hz, 2 CH_{Ph}), 6.98 (d, 1 H, $^3J_{HH}$ = 8.4 Hz, 1 CH_{Xyl}), 6.93 (d, 1 H, $^3J_{HH}$ = 8.7 Hz, 1 CH_{Pyr}), 6.25 (br s, 1 H, NH), 6.23 (d, 1 H, $^3J_{HH}$ = 7.7 Hz, 1 CH_{Pyr}), 3.61, 2.11 (d, 1 H each, $^2J_{HH}$ = 4.8 Hz, Ir-CH_2), 2.47 (s, 3 H, 1 Me_{Xyl}), 1.58 (s, 15 H, 5 Me_{Cp*}); $^{13}C\{^1H\}$ NMR (CD_2Cl_2, 25 ºC): δ = 154.5, 154.0 (C_{q-Pyr}), 141.4, 118.8, 108.8 (CH_{Pyr}), 137.8 (C_{q-Xyl}), 136.9 (C_{q-Ph}), 134.0, 130.4, 129.5 (CH_{Xyl}), 130.8, 126.8, 122.8 (2:1:2, CH_{Ph}), 100.8 (Ir-CH_2-C_q), 93.9 (Ir-C_{q-Xyl}), 90.3 (C_{q-Cp*}), 35.6 (Ir-CH_2), 20.8 (Me_{Xyl}), 9.3 (Me_{Cp*}); HRMS (FAB): m/z calcd. for $C_{29}H_{32}N_2Ir$ $[M]^+$: 601.2195; found: 601.2181; elemental analysis for $C_{61}H_{44}BF_{24}IrN_2$: C, 50.0; H, 3.0; N, 1.9; found: C, 49.8; H, 3.1; N, 1.8.

Compound [8-Rh]BArF. In a Young NMR tube, a solution of complex [3-Rh]BArF (40 mg, 0.029 mmol) in CH_2Cl_2 (0.5 mL) was treated with H_2 (60 mol %) and after 24 h at room temperature ^1H NMR analysis of the reaction mixture revealed transformation into complex [8-Rh]BArF in 50 % spectroscopic yield. [8-Rh]BArF was separated by fractional crystallization from CH_2Cl_2-pentane mixtures at -23 ºC as bright red crystals. Yield: 16 mg (38%). IR (Nujol): ν(NH) 3396 cm^{-1}; ^1H NMR (CD_2Cl_2, 25 ºC): δ = 7.73 (br s, 1 H, 1 CH_{Xyl}, detected by NOESY experiment, under the $BArF^-$ signal), 7.63, 6.90, 6.30 (t, d, d, 1 H each, $^3J_{HH}$ ~ 7.5 Hz, 3 CH_{Pyr}), 7.49 (m, 3 H, 1 CH_{Xyl} + 2 CH_{Ph}), 7.31, 7.25 (t, d, 1:2, $^3J_{HH}$ ~ 7.5 Hz, 3 CH_{Ph}), 6.97 (d, 1 H, $^3J_{HH}$ ~ 7.5 Hz, 1 CH_{Xyl}), 6.14 (br s, 1 H, NH), 3.64, 2.54 (d, 1 H each, $^2J_{HH}$ ~ 3.5 Hz, Rh–CH_2), 2.48 (s, 3 H, 1 Me_{Xyl}), 1.51 (s, 15 H, 5 Me_{Cp*}); $^{13}C\{^1H\}$ NMR (CD_2Cl_2, 25 ºC): δ = 155.6, 153.8 (C_{q-Pyr}), 141.4, 117.5, 109.1 (CH_{Pyr}), 137.9 (C_{q-Xyl}), 137.3 (C_{q-Ph}), 133.5, 131.0, 129.0 (CH_{Xyl}), 130.8, 126.6, 122.6 (2:1:2, CH_{Ph}), 107.3 (br, Rh–CH_2–C_{q-Xyl},

detected by HMBC experiment), 100.6 (br, Rh–$C_{q\text{-Xyl}}$), 96.7 (d, $^1J_{CRh}$ = 7.3 Hz, $C_{q\text{-Cp*}}$), 47.9 (d, $^1J_{CRh}$ = 13.8 Hz, Rh–CH_2), 20.8 (Me_{Xyl}), 9.5 (Me_{Cp*}). HRMS (FAB): m/z calcd. for $C_{29}H_{32}N_2Rh$ [M]$^+$: 511.1621; found: 511.1620.

Observation of a hydride intermediate in the reaction of [3-Ir]BAr$_F$ with H$_2$. In a Young NMR tube, a solution of complex **[3-Ir]BAr$_F$** (0.02 g, 14 µmol) in CD_2Cl_2 (0.5 mL) was treated with H$_2$ (500 mol %) and after 1-2 min. at room temperature the solution color changed from dark grey to orange and ^{1}H NMR analysis of the reaction mixture revealed formation of a hydride intermediate in ≥ 95% spectroscopic yield. This complex could not be isolated nor be completely characterized (see text). ^{1}H NMR (CD_2Cl_2, 25 ºC): δ = 8.03 (t, 1 H, $^3J_{HH}$ = 7.9 Hz 1 CH_{Ar}), 7.53-6.85 (10 CH_{Ar}), 2.12 (s, 6 H, 2 Me_{Xyl}), 1.20 (s, 15 H, 5 Me_{Cp*}), -6.32 (s, 1 H, Ir–H). A resonance attributable to a possible N*H* proton could not be located.

Compound [9-Ir]BAr$_F$. CO (g) was bubbled through a solution of compound **[8-Ir]BAr$_F$** (0.01 g, 6.8 µmol) in CH_2Cl_2 (2.5 mL), at room temperature for 5 minutes. The solution changed color immediately from orange to light yellow. The solvent was removed under reduced pressure and ^{1}H NMR analysis of the reaction product showed quantitative conversion into **[9-Ir]BAr$_F$**. It was washed with pentane and dried under vacuum. IR (Nujol): ν(NH) 3356 cm^{-1}, ν(CO) 2029 cm^{-1}; ^{1}H NMR (CD_2Cl_2, 25 ºC): δ = δ 7.64, 6.87 (t, d, 1 H each, $^3J_{HH}$ ~ 7.5 Hz, 2 CH_{Pyr}), 7.54, 7.42 (m, t, 2:1, $^3J_{HH}$ = 7.5 Hz, 3 CH_{Ph}), 7.30 (m, 3 H, 2 CH_{Ph} + 1 CH_{Xyl}), 7.19 (m, 3 H, 1 CH_{Xyl} + 1 CH_{Pyr} + NH), 7.10 (d, 1 H, $^3J_{HH}$ = 7.5 Hz, 1 CH_{Xyl}), 3.73, 2.99 (d, 1 H each, $^2J_{HH}$ = 11.0 Hz, Ir–CH_2), 2.32

(s, 3 H, 1 Me$_{Xyl}$), 1.67 (s, 15 H, 5 Me$_{Cp*}$); ^{13}C{^{1}H} NMR (CD$_2$Cl$_2$, 25 ℃): δ = 168.1 (CO), 159.7, 155.2 (C$_{q-Pyr}$), 144.6 (C$_{q-Ph}$), 140.4, 118.6, 108.4 (CH$_{Pyr}$), 138.1, 137.9, 137.5 (C$_{q-Xyl}$), 131.1, 128.2, 125.3 (2:1:2, CH$_{Ph}$), 129.9, 129.3, 123.6 (CH$_{Xyl}$), 101.9 (C$_{q-Cp*}$), 21.9 (Me$_{Xyl}$), 8.9 (Ir–CH$_2$), 8.8 (Me$_{Cp*}$); elemental analysis for C$_{62}$H$_{44}$BF$_{24}$IrN$_2$O: C, 49.9; H, 3.0; N, 1.9; found: C, 49.7; H, 3.4; N, 1.6.

Computational details

DFT calculations were carried out with the Gaussian 09 program.[39] Geometry optimizations of all species were calculated in the gas phase without restrictions using the PBE0 functional.[40] All light atoms were represented with the 6-31g(d,p) basis set, while the Ir and Rh atoms were described by the SDD basis set and its associated electron core potential.[41] Frequency calculations were performed on the optimized structures at the same level of theory to characterize the stationary points, as well as for the calculation of gas-phase enthalpies (H), entropies (S) and Gibbs energies (G). The nature of the intermediates connected by a transition state was determined by Intrinsic Reaction Coordinate (IRC) calculations or by perturbing the transition states along the TS coordinate and optimizing to a minimum. Bulk solvent effects were modelled using Truhlar's SMD continuum solvent model[42] and empirical dispersion corrections were added with the D3 version of Grimme's dispersion.[43-45] Both corrections were made on the gas phase geometries by single point calculations. All energies reported throughout the text are Zero Point corrected Potential Energies in dichloromethane.

ASSOCIATED CONTENT

Supporting Information

The Supporting Information is available free of charge on the ACS Publications Website.

Experimental procedures for the synthesis of compounds **1** and **[5-Rh]BAr$_F$**, proposed mechanism for the H$_2$-catalyzed isomerization between **3-M$^+$** and **8-M$^+$**, NMR spectra of all compounds, crystallographic data and details of the structure determinations for **2-Ir**, **2-Rh**, **[3-Ir]BAr$_F$**, **[4-Ir]BAr$_F$**, **[4-Rh]BAr$_F$**, **[5-Rh]BAr$_F$**, **[6-Ir]BAr$_F$**, **[7-Ir]BAr$_F$**, **[8-Ir]BAr$_F$** and **[8-Rh]BAr$_F$**, and additional computational details (PDF).

Geometric coordinates of all transition states and intermediates (XYZ).

Accession Codes

CCDC 1572330-1572339 contain the supplementary crystallographic data for this paper. These data can be obtained free of charge via www.ccdc.cam.ac.uk/data_request/cif, or by emailing data_request@ccdc.cam.ac.uk, or by contacting The Cambridge Crystallographic Data Centre, 12 Union Road, Cambridge CB2 1EZ, UK; fax: +44 1223 336033.

AUTHOR INFORMATION

Corresponding Author

*E-mail: nuria@iiq.csic.es (N. R.)

ORCID

Nuria Rendón: 0000-0003-1760-185X

Author Contributions

The manuscript was written through contributions of all authors. All authors have given approval to the final version of the manuscript.

Notes

The authors declare no competing financial interest.

REFERENCES

(1) (a) Valpuesta, J. E. V.; Rendón, N.; López-Serrano, J.; Poveda, M. L.; Sánchez, L.; Álvarez, E.; Carmona, E. Dihydrogen-Catalyzed Reversible Carbon–Hydrogen and Nitrogen–Hydrogen Bond Formation in Organometallic Iridium Complexes. *Angew. Chem. Int. Ed.* **2012**, *51*, 7555–7557. (b) Zamorano, A.; Rendón, N.; López-Serrano, J.; Valpuesta, J. E. V.; Álvarez, E.; Carmona, E. Dihydrogen Catalysis of the Reversible Formation and Cleavage of C—H and N—N Bonds of Aminopyridinate Ligands Bound to $(\eta^5\text{-}C_5Me_5)Ir^{III}$. *Chem. Eur. J.* **2015**, *21*, 2576–2587.

(2) Zamorano, A.; Rendón, N.; Valpuesta, J. E. V.; Álvarez, E.; Carmona, E. Synthesis and Reactivity toward H_2 of $(\eta^5\text{-}C_5Me_5)Rh(III)$ Complexes with Bulky Aminopyridinate Ligands. *Inorg. Chem.* **2015**, *54*, 6573–6581.

(3) (a) Barr, D.; Clegg, W.; Mulvey, R. E.; Snaith, R. The Isolation and Crystal Structure of [Ph(Z-Pyr)NLi].(HMPA)=[Ph(2-Pyr)NH]; a Model Monomeric Organonitrogen-Lithium Species containing Co-ordination of Lithium by both an Anchimeric Pyridyl N-Atom and by a Potentially Reactive Amine Ligand. *J. Chem. Soc. Chem. Commun.* **1984**, 469– 470. (b) Scott, N. M.; Schareina, T.; Tok, O.; Kempe, R. Lithium and Potassium Amides of Sterically Demanding Aminopyridines. *Eur. J. Inorg. Chem.* **2004**, 3297 –3304. (c) Lyubov, D. M.; Dçring, C.; Ketkov, S. Y.; Kempe, R.; Trifonov, A. A. Selective Protonation of the Y—C Bond in Trinuclear Yttrium Alkyl–Hydrido Clusters and Formation of the Cationic Polyhydrido Core. *Chem. Eur. J.* **2011**, *17*, 3824 –3826.

(4) (a) Hintermair, U.; Sheehan, S. W.; Parent, A. R.; Ess, D. H.; Richens, D. T.; Vaccaro, P. H.; Brudvig, G. W.; Crabtree, R. H. Precursor Transformation during Molecular Oxidation Catalysis with Organometallic Iridium Complexes. *J. Am. Chem. Soc.* **2013**, *135*, 10837 –10851. (b) Graeupner, J.; Hintermair, U.; Huang, D. L.; Thomsen, J. M.; Takase, M.; Campos, J.; Hashmi, S. M.; Elimelech, M.; Brudvig, G. W.; Crabtree, R. H. Probing the Viability of Oxo-Coupling Pathways in Iridium-

Catalyzed Oxygen Evolution. *Organometallics* **2013**, *32*, 5384 – 5390. (c) Hintermair, U.; Hashmi, S. M.; Elimelech, M.; Crabtree, R. H. Particle Formation during Oxidation Catalysis with Cp* Iridium Complexes. *J. Am. Chem. Soc.* **2012**, *134*, 9785 –9795. (d) Crabtree, R. H. An Organometallic Future in Green and Energy Chemistry? *Organometallics* **2011**, *30*, 17–19.

(5) Zuccaccia, C.; Bellachioma, G.; Bortolini, G.; Bucci, A.; Savini, A.; Macchioni, A. Transformation of a Cp*–Iridium(III) Precatalyst for Water Oxidation when Exposed to Oxidative Stress. *Chem. Eur. J.* **2014**, *20*, 3446–3456.

(6) Kuwata, S.; Ikariya, T. Metal–ligand bifunctional reactivity and catalysis of protic N-heterocyclic carbene and pyrazole complexes featuring β-NH units. *Chem. Commun.* **2014**, *50*, 14290–14300.

(7) (a) Han, Y.-F.; Jin, G.-X. Cyclometalated [Cp*M(C^X)] (M = Ir, Rh; X = N, C, O, P) complexes. *Chem. Soc. Rev.* **2014**, *43*, 2799–2823. (b) Wang, C.; Villa-Marcos, B.; Xiao, J. Hydrogenation of imino bonds with half-sandwich metal catalysts. *Chem. Commun.* **2011**, *47*, 9773–9785.

(8) Liu, Z.; Sadler, P. J. Organoiridium Complexes: Anticancer Agents and Catalysts. *Acc. Chem. Res.* **2014**, *47*, 1174–1185.

(9) Smith, D. P.; Chen, H.; Ogo, S.; Elduque, A. I.; Eisenstein, M.; Olmstead, M.; Fish, R. H. Bioorganometallic Chemistry. 27. Synthetic, X-ray Crystallographic, and Competitive Binding Studies in the Reactions of Nucleobases, Nucleosides, and Nucleotides with [Cp*Rh(H$_2$O)$_3$](OTf)$_2$, as a Function of pH, and the Utilization of Several Cp*Rh–DNA Base Complexes in Host–Guest Chemistry. *Organometallics* **2014**, *33*, 2389–2404.

(10) (a) Hartwig, J. *Organotransition Metal Chemistry. From Bonding to Catalysis;* University Science Books, **2010**. (b) Bochmann, N. *Organometallics and Catalysis: An Introduction;* Manfred. Oxford University Press. **2014**.

(11) See for example (a) Nova, A.; Taylor, D. J.; Blacker, A. J.; Duckett, S. B.; Perutz, R. N.; Eisenstein, O. Computational Studies Explain the Importance of Two Different Substituents on the Chelating Bis(amido) Ligand for Transfer Hydrogenation by Bifunctional Cp*Rh(III) Catalysts. *Organometallics* **2014**, *33*, 3433−3442 and references therein. (b) Blacker, A. J.; Clot, E.; Duckett, S. B.; Eisenstein, O.; Grace, J.; Nova, A.; Perutz, R. N.; Taylor, D. J.; Whitwood, A. C. Synthesis and structure of "16-electron" rhodium(III) catalysts for transfer hydrogenation of a cyclic imine: mechanistic implications. *Chem. Commun.* **2009**, 6801−6803.

(12) (a) Hanley, P. S.; Hartwig, J. F. Migratory Insertion of Alkenes into Metal–Oxygen and Metal–Nitrogen Bonds. *Angew. Chem. Int. Ed.* **2013**, *52*, 8510-8525. (b) Tye, J. W.; Hartwig, J. F. Computational Studies of the Relative Rates for Migratory Insertions of Alkenes into Square-Planar, Methyl, −Amido, and −Hydroxo Complexes of Rhodium. *J. Am. Chem. Soc.* **2009**, *131*, 14703-14712.

(13) (a) Casalnuovo, A. L.; Calabrese, J. C.; Milstein, D. Rational design in homogeneous catalysis. Iridium(I)-catalyzed addition of aniline to norbornylene via nitrogen-hydrogen activation. *J. Am. Chem. Soc.* **1988**, *110*, 6738-6744. (b) Neukom, J. D.; Perch, N. S.; Wolfe, J. P. Intramolecular Alkene Aminopalladation Reactions of (dppf)Pd(Ar)[N(Ar^1)(CH$_2$)$_3$CH═CH$_2$] Complexes. Insertion of Unactivated Alkenes into Pd−N Bonds. *J. Am. Chem. Soc.* **2010**, *132*, 6276-6277. (c) White, P. B.; Stahl, S. S. Reversible Alkene Insertion into the Pd–N Bond of Pd(II)-Sulfonamidates and Implications for Catalytic Amidation Reactions. *J. Am. Chem. Soc.* **2011**, *133*, 18594-18597.

(14) For the terminology employed to refer to complexes with carbene ligands see: Peloso, R.; Carmona, E. Non-heteroatom-substituted alkylidene complexes of groups 10 and 11. *Coord. Chem. Rev.* **2017**, DOI: 10.1016/j.ccr.2017.07.018. See also ref. 10b.

(15) Heiden, Z. M.; Rauchfuss, T. B. Homogeneous Catalytic Reduction of Dioxygen Using Transfer Hydrogenation Catalysts. *J. Am. Chem. Soc.* **2007**, *129*, 14303-14310.

(16) (a) Holland, P. L.; Andersen, R. A.; Bergman, R. G. Synthesis, Characterization, Isomerization, and Reactivity of Dimeric Cyclopentadienylnickel Amido Complexes. *J. Am. Chem. Soc.* **1996**, *118*, 1092-1104. (b) Mindiola, D. J.; Hillhouse, G. L. Isocyanate and carbodiimide synthesis by nitrene-group-transfer from a nickel(II) imido complex. *Chem. Comm.* **2002**, 1840-1841. (c) Tomon, T.; Koizumi, T.-a; Tanaka, K. Electrochemical Hydrogenation of $[Ru(bpy)_2(napy-\kappa N)(CO)]^{2+}$: Inhibition of Reductive Ru—CO Bond Cleavage by a Ruthenacycle. *Angew. Chem. Int. Ed.* **2005**, *44*, 2229–2232. (d) Liang, L.-C.; Hung, Y.-T.; Huang, Y.-L.; Chien, P.-S.; Lee, P.-Y.; Chen, W.-C. Divergent Carbonylation Reactivity Preferences of Nickel Complexes Containing Amido Pincer Ligands: Migratory Insertion versus Reductive Elimination. *Organometallics* **2012**, *31*, 700-708. (e) Shishilov, O. N.; Kumanyaev, I. M.; Akhmadullina, N. S.; Churakov, A. V.; Garbuzova, I. A.; Flid, V. R. The first carbamoyl–carboxylate complex of transition metals: Synthesis and structure of $\{(OC_4H_8NH)[OC_4H_8NC(O)]Pd\}_2(\mu-CMe_3CO_2)_2$. *Inorg. Chem. Commun.* **2015**, *58*, 16-19.

(17) Bassetti, Mauro; Monti, Donato; Haynes, Anthony; Pearson, Jean M.; Stanbridge, Ian A.; Maitlis, Peter M. Relative reaction rates for rhodium and iridium: oxidative addition of methyl iodide to M(I) and the migratory insertion in M(III) methyl carbonyl complexes. *Gazz. Chim. Ital.* **1992**, *122*, 391-393.

(18) Campos, J.; Carmona, E. Rhodium and Iridium Complexes of Bulky Tertiary Phosphine Ligands. Searching for Isolable Cationic M[III] Alkylidenes. *Organometallics* **2015**, *34*, 2212−2221.

(19) (a) Lara, P.; Paneque, M.; Poveda, M. L.; Santos, L. L.; Valpuesta, J. E. V; Carmona, E.; Moncho, S.; Ujaque, G.; Lledós, A.; Álvarez, E.; Mereiter, K.

Experimental and Computational Studies on the Iridium Activation of Aliphatic and Aromatic C—H Bonds of Alkyl Aryl Ethers and Related Molecules. *Chem. Eur. J.* **2009**, *15*, 9034–9045. (b) Paneque, M.; Poveda, M. L.; Santos, L.L.; Carmona, E.; Mereiter, K. Generation of Metallacyclic Structures from the Reactions of Vinyl Ethers with a Tp^{Me2}Ir^{III} Compound *Organometallics* **2008**, *27*, 6353–6359. (c) Paneque, M.; Poveda, M. L.; Rendón, N.; Álvarez, E.; Carmona, E. The Synthesis of Iridabenzenes by the Coupling of Iridacyclopentadienes and Olefins. *Eur. J. Inorg. Chem.* **2007**, 2711–2720.

(20) Campos, J.; López−Serrano, J.; Álvarez, E.; Carmona, E. Cationic Ir(III) Alkylidenes Are Key Intermediates in C–H Bond Activation and C–C Bond-Forming Reactions. *J. Am. Chem. Soc.* **2012**, *134*, 7165−7175.

(21) (a) Lara, P.; Paneque, M.; Poveda, M. L.; Santos, L. L.; Valpuesta, J. E. V; Salazar, V.; Carmona, E.; Moncho, S.; Ujaque, G.; Lledós, A.; Maya, C.; Mereiter, K. Synthetic, Mechanistic, and Theoretical Studies on the Generation of Iridium Hydride Alkylidene and Iridium Hydride Alkene Isomers. *Chem. Eur. J.* **2009**, *15*, 9046–9057. (b) Paneque, M.; Poveda, M. L.; Santos, L. L.; Carmona, E.; Lledós, A.; Ujaque, G.; Mereiter, K. A Measureable Equilibrium between Iridium Hydride Alkylidene and Iridium Hydride Alkene Isomers. *Angew. Chem. Int. Ed.* **2004**, *43*, 3708–3711.

(22) Clot, E.; Chen, J.; Lee, D.-H.; Sung, S. Y.; Appelhans, L. N.; Faller, J. W.; Crabtree, R. H.; Eisenstein, O. Double Geminal C−H Activation and Reversible α-Elimination in 2-Aminopyridine Iridium(III) Complexes: The Role of Hydrides and Solvent in Flattening the Free Energy Surface. *J. Am. Chem. Soc.* **2004**, *126*, 8795–8804.

(23) Schrock, R. R.; Seidel, S. W.; Mösch-Zanetti, N. C.; Shih, K.-Y.; O'Donoghue, M. B.; Davis, W. M.; Reiff, W. M. Synthesis and Decomposition of Alkyl Complexes of Molybdenum(IV) That Contain a [(Me$_3$SiNCH$_2$CH$_2$)$_3$N]$^{3-}$ Ligand. Direct Detection

of α-Elimination Processes That Are More than Six Orders of Magnitude Faster than β-Elimination Processes. *J. Am. Chem. Soc.* **1997**, *119*, 11876–11893.

(24) Campos, J.; Esqueda, A. C.; López-Serrano, J.; Sánchez, L.; Cossio, F. P.; de Cozar, A.; Álvarez, E.; Maya, C.; Carmona, E. A Cationic Rh(III) Complex That Efficiently Catalyzes Hydrogen Isotope Exchange in Hydrosilanes. *J. Am. Chem. Soc.* **2010**, *132*, 16765–16767.

(25) Brookhart, M.; Green, M. L. H.; Parkin, G. Agostic interactions in transition metal compounds. *Proc. Natl. Acad. Sci. USA* **2007**, *104*, 6908–6914.

(26) (a) Grabowski, S. J. What Is the Covalency of Hydrogen Bonding?. *Chem. Rev.* **2011**, *111*, 2597–2625. (b) Saßmannshausen, J. Quo Vadis, agostic bonding?. *Dalton Trans.* **2012**, *41*, 1919–1923. (c) Scherer, W.; McGrady, G. S. Agostic Interactions in d^0 Metal Alkyl Complexes. *Angew. Chem. Int. Ed.* **2004**, *43*, 1782–1806. (d) van der Eide, E. F.; Yang, P.; Bullock, R. M. Isolation of Two Agostic Isomers of an Organometallic Cation: Different Structures and Colors. *Angew. Chem. Int. Ed.* **2013**, *52*, 10190–10194. (e) Dunlop-Brière, A. F.; Baird, M. C. [Cp$_2$TiCH$_2$CHMe(SiMe$_3$)]$^+$, an Alkyl–Titanium Complex Which (a) Exists in Equilibrium between a β-Agostic and a Lower Energy γ-Agostic Isomer and (b) Undergoes Hydrogen Atom Exchange between α-, β-, and γ-Sites via a Combination of Conventional β-Hydrogen Elimination–Reinsertion and a Nonconventional CH Bond Activation Process Which Involves Proton Tunnelling. *J. Am. Chem. Soc.* **2013**, *135*, 17514–17527.

(27) (a) Bruce, M. I. Organometallic chemistry of vinylidene and related unsaturated carbenes. *Chem. Rev.* **1991**, *91*, 197–257. (b) Bruneau, C.; Dixneuf, P. H. Metal Vinylidenes in Catalysis. *Acc. Chem. Res.* **1999**, *32*, 311–323. (c) Werner, H. Vinylidenerhodium complexes as promising tools for C–C coupling reactions. *Coord. Chem. Rev.* **2004**, *248*, 1693-1702. (d) Lynam, J. M. Recent Mechanistic and Synthetic Developments in the Chemistry of Transition-Metal Vinylidene Complexes. *Chem. Eur. J.* **2010**, *16*, 8238–8247.

(28) (a) Khusnutdinova, J. R.; Milstein, D. Metal–Ligand Cooperation. *Angew. Chem. Int. Ed.* **2015**, *54*, 12236–12273. (b) Milstein, D. Metal–ligand cooperation by aromatization–dearomatization as a tool in single bond activation. *Phil. Trans. R. Soc. A.* **2015**, *373*, 20140189.

(29) Arita, A. J.; Cantada, J.; Grotjahn, D. B.; Cooksy, A. L. Computational Study of the Extensive Role of Heterocyclic Ligands in Acetylene Hydration by a Bifunctional Organometallic Catalyst. *Organometallics* **2013**, *32*, 6867–6870.

(30) (a) Álvarez, E.; Conejero, C.; Lara, P.; López, J. A.; Paneque, M.; Petronilho, A.; Poveda, M. L.; del Río, D.; Serrano, O.; Carmona, E. Rearrangement of Pyridine to Its 2-Carbene Tautomer Mediated by Iridium. *J. Am. Chem. Soc.* **2007**, *129*, 14130-14131. (b) Cristóbal, C.; Hernández, Y. A.; López-Serrano, J.; Paneque, M.; Petronilho, A.; Poveda, M. L.; Salazar, V.; Vattier, F.; Álvarez, E.; Maya, C.; Carmona, E. Reactivity Studies of Iridium Pyridylidenes [$Tp^{Me2}Ir(C_6H_5)_2(C(CH)_3C(R)NH$] (R=H, Me, Ph). *Chem. Eur. J.* **2013**, *19*, 4003–4020.

(31) Crabtree. R. H. *The Organometallic Chemistry of the Transition Metals*; 5th Edition, John Wiley and Sons Inc. **2009**.

(32) (a) Jaffart, J.; Cole, M. L.; Etienne, M.; Reinhold, M.; McGrady, J. E.; Maseras, F. C–H and C–C agostic interactions in cycloalkyl tris(pyrazolyl)boratoniobium complexes. *Dalton Trans.* **2003**, 4057–4064. (b) Jaffart, J.; Etienne, M.; Maseras, F.; McGrady, J. E.; Eisenstein, O. Equilibria between α- and β-Agostic Stabilized Rotamers of Secondary Alkyl Niobium Complexes. *J. Am. Chem. Soc*. **2001**, *123*, 6000–6013. (c) Fryzuk, M. D.; Johnson, S. A.; Rettig, S. R. Reaction of [P_2N_2]Ta=CH2(Me) with Ethylene: Synthesis of [P_2N_2]Ta(C_2H_4)Et, a Neutral Species with a β-Agostic Ethyl Group in Equilibrium with an α-Agostic Ethyl Group ([P_2N_2] = PhP($CH_2SiMe_2NSiMe_2CH_2$)$_2$PPh). *J. Am. Chem. Soc.* **2001**, *123*, 1602–1612. (d) Li, X.; Appelhans, L. N.; Faller, J. W.; Crabtree, R. H. Stoichiometric C−C Coupling Reactions

in the Coordination Sphere of an Iridium(III) Alkyl. *Organometallics* **2004**, *23*, 3378–3387.

(33) White, C.; Oliver, A. J.; Maitlis, P. M. Pentamethylcyclopentadienyl- rhodium and -iridium Complexes. Part VII. Mono-, Di-, and Tri-μ-Hydrido-complexes. *J. Chem. Soc. Dalton Trans*. **1973**, 1901–1907.

(34) Clot, E.; Eisenstein, O.; Dubé, T.; Faller, J. W.; Crabtree, R. H. Interplay of Weak Interactions: An Iridium(III) System with an Agostic tert-Butyl but a Nonagostic Isopropyl Group. *Organometallics* **2002**, *21*, 575–580.

(35) (a) Kang, J. W.; Maitlis, P. M. Pentamethylcyclopentadienyl)rhodium and -iridium complexes. V. Complexes with oxy-ligands and the exchange of methyl protons by deuterium under basic conditions. *J. Organomet. Chem.* **1971**, *30*, 127−133. (b) Vargaftik, M. N.; Struchkov, Y. T.; Yanovsky, A. I.; Maitlis, P. M. Synthesis and X-Ray Structure of Cp*Rh(III)-Molybdate Complexes Derived from Bis(triphenylphosphineiminium) Mono- and Polymolybdates. *Mendeleev Commun*. **1993**, *3*, 247−249.

(36) (a) Moseley, K.; Kang, J. W; Maitlis, P. M. Pentamethylcyclopentadienyl-rhodium and -iridium halides. II. Reactions with mono-, di-, and triolefins. *J. Chem. Soc. (A) Inorg. Phys. Theor.* **1970**, *17*, 2875-83. (b) Paneque, M.; Maitlis, P. M. Loss of pentamethylcyclopentadiene from pentamethylcyclopentadienylrhodium hydride complexes. *J. Chem. Soc. Chem. Comm.* **1989**, 105-106.

(37) White, C.; Yates, A.; Maitlis, P. M.; Heinekey, D. M. (η[5]-Pentamethylcyclopentadienyl)Rhodium and -Iridium Compounds. *Inorg. Synth*. **1992**, *29*, 228-234.

(38) Brookhart, M.; Grant, B.; Volpe, A. F. [(3,5-$(CF_3)_2C_6H_3)_4$B]-[H$(OEt_2)_2$]$^+$: a convenient reagent for generation and stabilization of cationic, highly electrophilic organometallic complexes. *Organometallics* **1992**, *11*, 3920-3922.

(39) Frisch, M. J.; Trucks, G. W.; Schlegel, H. B.; Scuseria, G. E.; Robb, M. A.; Cheeseman, J. R.; Scalmani, G.; Barone, V.; Mennucci, B.; Petersson, G. A.; Nakatsuji, H.; Caricato, M.; Li, X.; Hratchian, H. P.; Izmaylov, A. F.; Bloino, J.; Zheng, G. ; Sonnenberg, J. L.; Hada, M.; Ehara, M.; Toyota, K.; Fukuda, R.; Hasegawa, J.; Ishida, M.; Nakajima, T.; Honda, Y.; Kitao, O.; Nakai, H.; Vreven, T.; Montgomery Jr., J. A.; Peralta, J. E.; Ogliaro, F.; Bearpark, M. J.; Heyd, J.; Brothers, E. N.; Kudin, K. N.; Staroverov, V. N.; Keith, T.; Kobayashi, R.; Normand, J.; Raghavachari, K.; Rendell, A. P.; Burant, J. C.; Iyengar, S. S.; Tomasi, J.; Cossi, M.; Rega, N.; Millam, N. J.; Klene, M.; Knox, J. E.; Cross, J. B.; Bakken, V.; Adamo, C.; Jaramillo, J.; Gomperts, R.; Stratmann, R. E. ; Yazyev, O.; Austin, A. J.; Cammi, R.; Pomelli, C.; Ochterski, J. W.; Martin, R. L.; Morokuma, K.; Zakrzewski, V. G.; Voth, G. A.; Salvador, P.; Dannenberg, J. J.; Dapprich, S.; Daniels, A. D.; Farkas, Ö.; Foresman, J. B.; Ortiz, J. V.; Cioslowski, J.; Fox, D. J. Revision D.01 ed., Gaussian, Inc., Wallingford, CT, USA, **2013**.

(40) (a) Perdew, J. P.; Burke, K.; Ernzerhof, M. Generalized Gradient Approximation Made Simple. *Phys. Rev. Lett.* **1996**, *77*, 3865-3868. (b) Perdew, J. P.; Burke, K.; Ernzerhof, M. Generalized Gradient Approximation Made Simple (Errata). *Phys. Rev. Lett.* **1997**, *78*, 1396.

(41) Andrae, D.; Häußermann U.; Dolg, M.; Stoll, H.; Preuß, H. Energy-adjusted *ab initio* pseudopotentials for the second and third row transition elements. *Theor. Chim. Acc.* **1990***, 77*, 123-141.

(42) Marenich, A. V.; Cramer, C. J.; Truhlar, D. G. Universal Solvation Model Based on Solute Electron Density and on a Continuum Model of the Solvent Defined by the Bulk Dielectric Constant and Atomic Surface Tensions. *J. Phys. Chem. B* **2009**, *113*, 6378-6396.

(43) Grimme, S.; Antony, J.; Ehrlich, S.; Krieg, H. A consistent and accurate *ab initio* parametrization of density functional dispersion correction (DFT-D) for the 94 elements H-Pu. *J. Chem. Phys*. **2010**, *132*, 154104.

(44) Miloserdov, F. M.; McKay, D.; Muñoz, B. K.; Samouei, H.; Macgregor, S. A.; Grushin, V. V. Exceedingly Facile Ph—X Activation (X=Cl, Br, I) with Ruthenium(II): Arresting Kinetics, Autocatalysis, and Mechanisms. *Angew. Chem. Int. Ed*. **2015**, *54*, 8466-8470.

(45) Miloserdov, F. M.; McMullin, C. L.; Belmonte, M. M. N.; Benet-Buchholz, J.; Bakhmutov, V. I.; Macgregor, S. A.; Grushin, V. V. The Challenge of Palladium-Catalyzed Aromatic Azidocarbonylation: From Mechanistic and Catalyst Deactivation Studies to a Highly Efficient Process. *Organometallics* **2014**, *33*, 736-752.

Insert Table of Contents Graphic and Synopsis Here

"For Table of Contents Only"
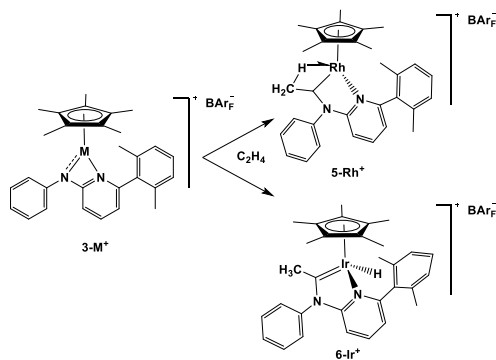
A study on the reactivity of cationic Rh(III) and Ir(III) complexes of composition $[(\eta^5\text{-}C_5Me_5)M(N^\wedge N)]^+$ (complexes **3-M$^+$**) with small molecules such as CO, C_2H_4 and H_2 is reported. Migratory insertion reactivity is observed with CO and C_2H_4 while H_2 catalyzed the isomerization of the aminopyridinate ligand from the κ^2-*N,N′* coordination to a κ-*N*-η^3-pseudo-allylic bonding mode.

Supporting Information for the paper:

Activation of Small Molecules by the Metal-Amido Bond of Rhodium(III) and Iridium(III) (η^5-C$_5$Me$_5$)M-Aminopyridinate Complexes

Ana Zamorano, Nuria Rendón,* Joaquín López-Serrano, Eleuterio Álvarez, and Ernesto Carmona

TABLE OF CONTENTS:

I. SYNTHESIS AND CHARACTERIZATION:

Compound 1.

Scheme S1. Synthesis of the aminopyridine ligand utilized in this work.

Step 1. To a suspension of magnesium turnings in THF (6 g, 247 mmol; 120 mL), a solution of 2-Br-1,3-Me$_2$C$_6$H$_3$ in THF (39.1 g, 211.2 mmol, 28.1 mL; 40 mL) was added dropwise. The reaction mixture was activated using 1,2-dibromoethane (2.5 mL). An ice bath was used to cool the reaction mixture when it became too vigorous. The reaction mixture was stirred at room temperature for 12 h and then filtered and the filtrate used directly in *step 2*.

Step 2: The filtrate (*step 1*) was transferred and added dropwise to a Schlenk flask containing a cooled (0 °C) solution in THF (100 mL) of 2,6-dibromopyridine (47.5 g, 200.4 mmol), tricyclohexylphosphane (0.13 g, 0.45 mmol) and [NiBr$_2$(dme)] (dme = dimethoxyethane) (0.07 g, 0.23 mmol). The resulting mixture was warmed to room temperature, stirred for 1 h, and then heated at 50 °C for 72 h. Water (200 mL) and CH$_2$Cl$_2$ (200 mL) were added and the resulting suspension transferred to a separating funnel. The organic phase was collected and the aqueous phase washed with CH$_2$Cl$_2$

(100 mL) and extracted. The combined organic phases were washed with a saturated sodium chloride solution and dried with Na_2SO_4. After filtration, the organic phase was concentrated to dryness under vacuum resulting in an orange-coloured oily product, which was purified by column chromatography on silica gel using dichloromethane as eluent. The residue obtained after evaporation of the solvent was washed with pentane. Yield: 45.2 g (86 %).

Step 3: the solid obtained in *step 2* (10 g, 38.2 mmol), 1,3-bis(diphenylphosphanyl)propane (0.58 g, 1.4 mmol), tris(dibenzylideneacetone)dipalladium(0) (0.63 g, 0.7 mmol) and sodium tert-butoxide (4.2 g, 43 mmol) were combined in a Schlenk flask and aniline (3.6 g, 38.2 mmol, 3.5 mL) dissolved in toluene (120 mL) was added to the flask. The resulting mixture was heated at 95 °C for 72 h, was then cooled to room temperature and treated with water (200 mL) and diethyl ether (200 mL). The organic phase was extracted and the aqueous phase washed with diethyl ether (3x100 mL). The combined organic phases were washed with a saturated sodium chloride solution and the organic phase was dried with sodium sulfate. After filtration, the organic phase was concentrated to dryness under vacuum and the resulting solid was purified by column chromatography on silica gel using CH_2Cl_2 as eluent, and crystallised from a CH_2Cl_2:Et_2O:pentane mixture at -20 °C as colourless crystals. Yield: 5.2 g (50%). IR (Nujol): ν(NH) 3204 cm^{-1}; ^{1}H NMR (CDCl$_3$, 25 ºC): δ = 7.66 (t, 1 H, $^3J_{HH}$ = 7.8 Hz, 1 CH$_{Pyr}$), 7.40 (br s, 2 H, 2CH$_{Ph}$), 7.34 (br s, 3 H, 1 CH$_{Xyl}$ + 2 CH$_{Ph}$), 7.26 (d, 2 H, $^3J_{HH}$ = 9.6 Hz, 2 CH$_{Xyl}$), 7.15 (t, 1 H, $^3J_{HH}$ = 7.5 Hz, 1 CH$_{Ph}$), 7.01 (d, 1 H, $^3J_{HH}$ = 8.2 Hz, 1 CH$_{Pyr}$), 6.85 (br s, 1 H, NH), 6.80 (d, 1 H, $^3J_{HH}$ = 7.3 Hz, 1 CH$_{Pyr}$), 2.32 (s, 6 H, 2 Me$_{Xyl}$); ^{13}C{^{1}H} NMR (CDCl$_3$, 25 ºC): δ = 158.5, 155.9 (C$_{q-Pyr}$), 140.6, 135.7 (1:2, C$_{q-Xyl}$), 137.9, 115.5, 105.7 (CH$_{Pyr}$), 129.1, 122.5, 120.2 (2:1:2, CH$_{Ph}$), 127.6, 127.5 (1:2, CH$_{Xyl}$), 122.2 (C$_{q-Ph}$), 20.3 (Me$_{Xyl}$); Anal. Calcd (%) for C$_{19}$H$_{18}$N$_2$: C, 83.2; H, 6.6; N, 10.2. Found: C, 83.0, H, 6.4; N, 10.5.

Compound [5-Rh]BAr$_F$. C$_2$H$_4$ (g) was bubbled through a cold (0 ºC) solution of compound **[3-Rh]BAr$_F$** (0.3 mg, 0.217 mmol) in CH$_2$Cl$_2$ (15 mL) for 5 min. During this period of time the colour of the solution changed from dark green to orange. After evaporating the solvent under reduced pressure, ^{1}H NMR analysis of the crude product revealed the formation of complex **[5-Rh]BAr$_F$** in admixture with at least four more

rhodium compounds. A few crystals of complex **[5-Rh]BAr$_F$** were obtained by crystallization from CH_2Cl_2-hexane mixtures at -23 ºC. Selected NMR data was extracted from the crude reaction mixture. ^{1}H NMR (CD$_2$Cl$_2$, 25 ºC): δ = 5.02 (q, 1 H, $^3J_{HH}$ ~ 6 Hz, CH(CH$_3$)), 2.29 (s, 6 H, 2 Me$_{Xyl}$), 1.35 (s, 15 H, Me$_{Cp*}$), -0.21 (d, 3 H, $^3J_{HH}$ ~ 6 Hz, CH(CH_3)); ^{13}C{^{1}H} NMR: δ = 99.8 (d, $^1J_{CRh}$ = 8 Hz, C$_{q-Cp*}$), 79.8 (d, $^1J_{CRh}$ ~21 Hz, CH(CH$_3$)), 21.2 (Me$_{Xyl}$), 10.1 (Me$_{Cp*}$), -1.1 (CH(CH$_3$), $^1J_{CH}$ ~130 Hz).

II.   PROPOSED   MECHANISM   FOR   THE   H$_2$-CATALYZED ISOMERIZATION BETWEEN SPECIES 3-M$^+$ AND 8-M$^+$.
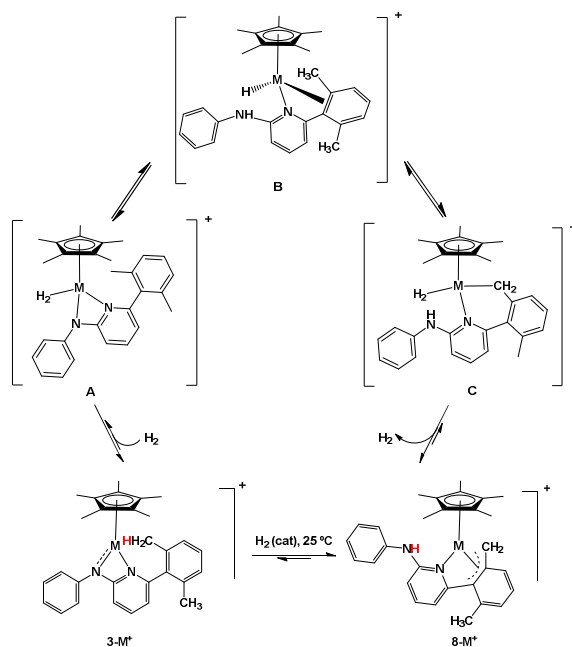
Scheme S2. Proposed mechanism for the H$_2$-catalyzed isomerization between species **3-M$^+$** and **8-M$^+$**.

III.   NMR SPECTRA:
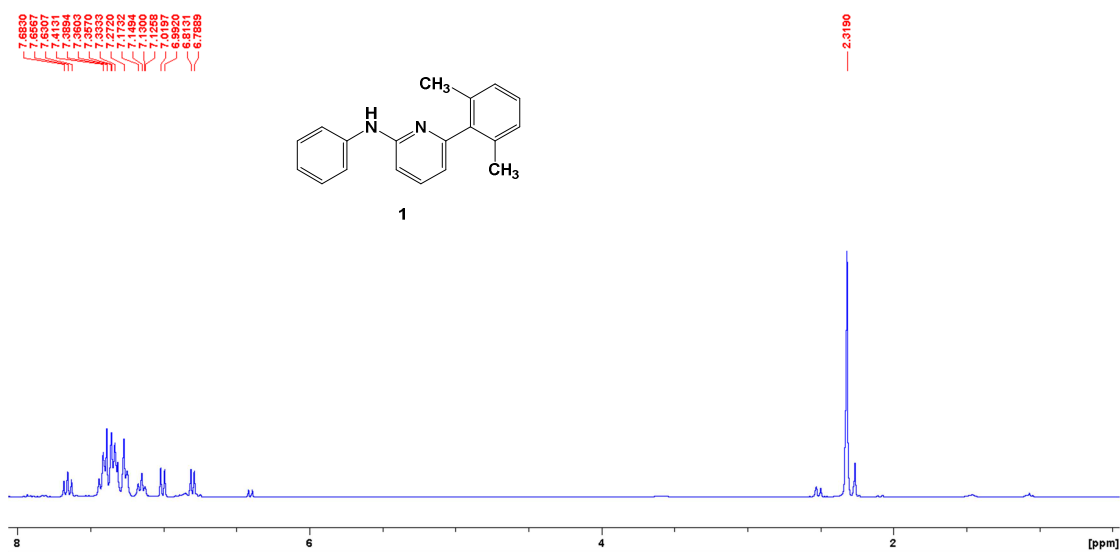
Figure S1. ^{1}H NMR spectrum (300 MHz, CDCl$_3$, 25 °C) of the aminopyridine precursor **1**, employed in this work.
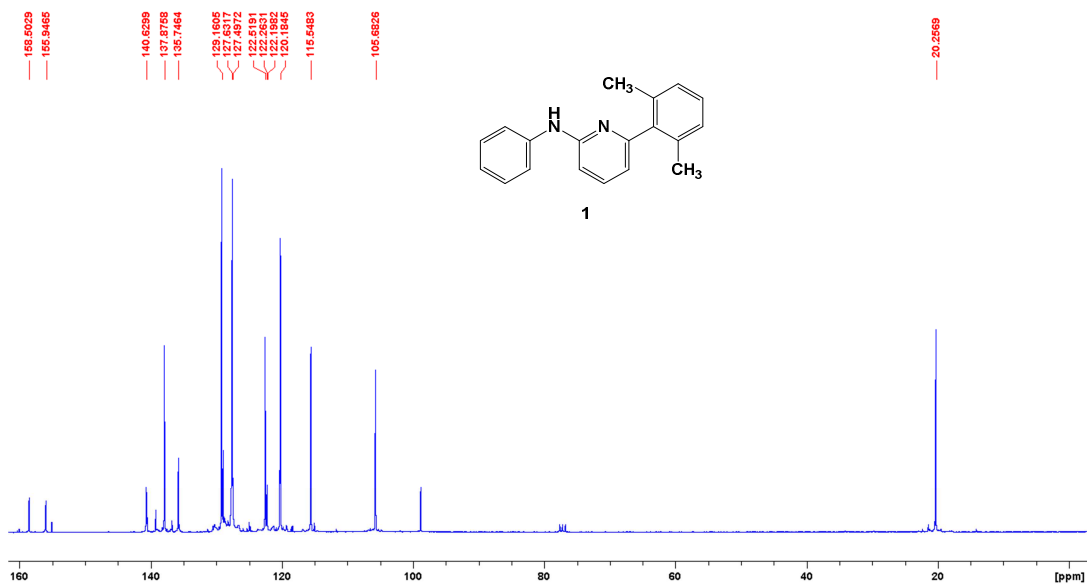
Figure S2. ^{13}C{^{1}H} NMR spectrum (75 MHz, CDCl$_3$, 25 °C) of the aminopyridine precursor **1**, employed in this work.
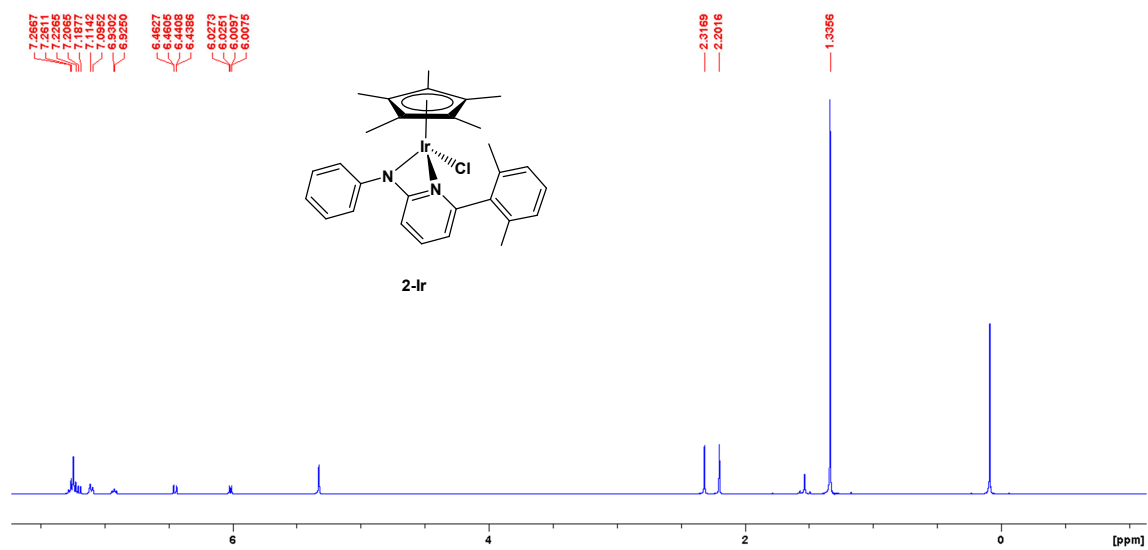
Figure S3. ^{1}H NMR spectrum (400 MHz, CD$_2$Cl$_2$, 25 ℃) of **2-Ir**.
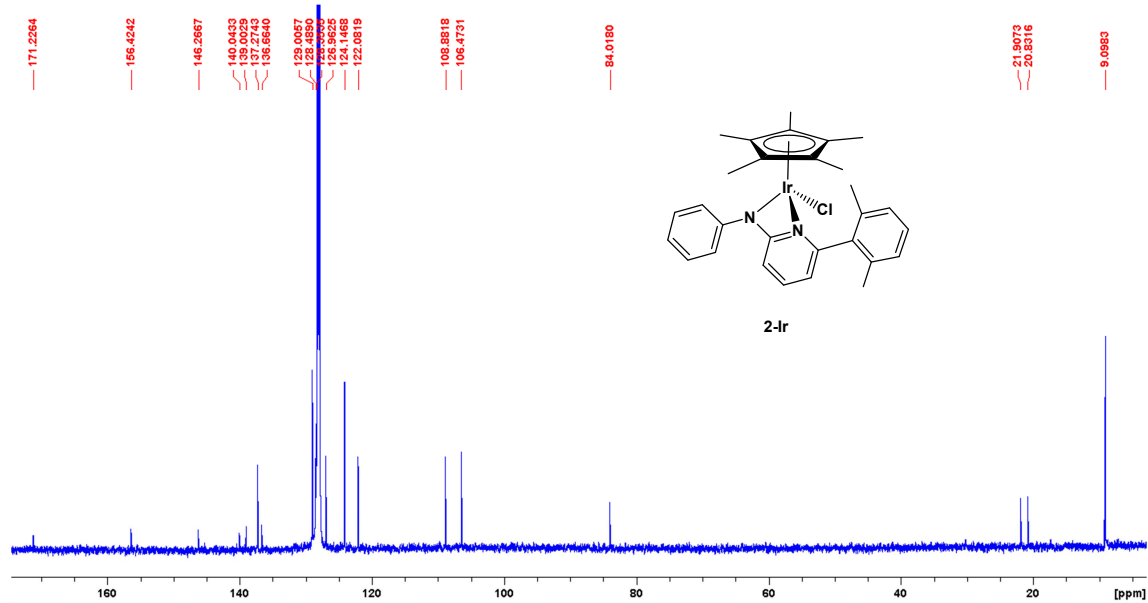
Figure S4. ^{13}C{^{1}H} NMR spectrum (125 MHz, C$_6$D$_6$, 25 ℃) of **2-Ir**.
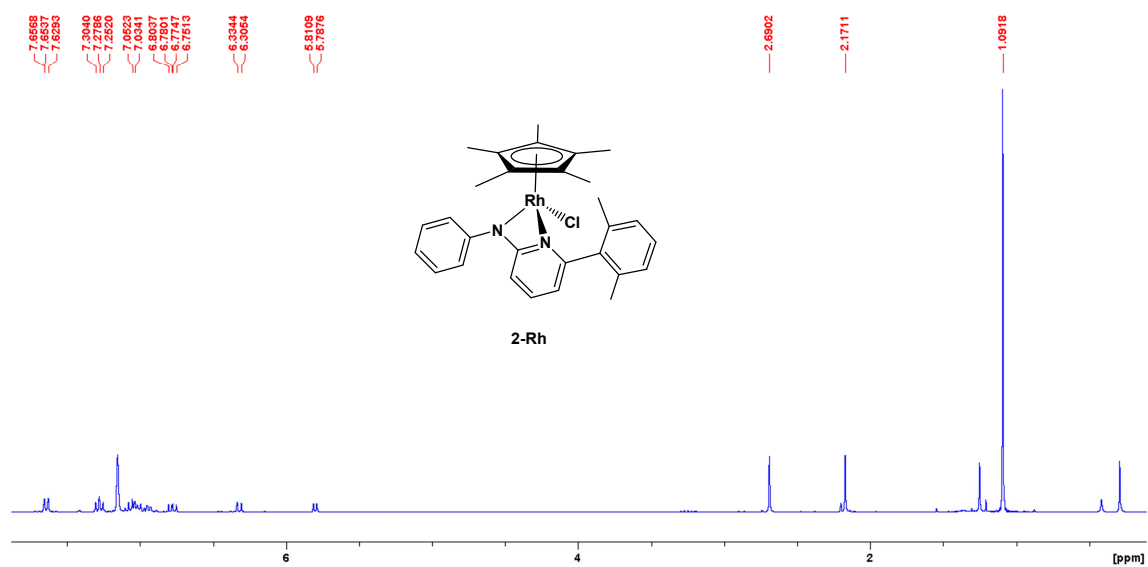
Figure S5. ^{1}H NMR spectrum (400 MHz, CD$_2$Cl$_2$, 25 °C) of **2-Rh**.
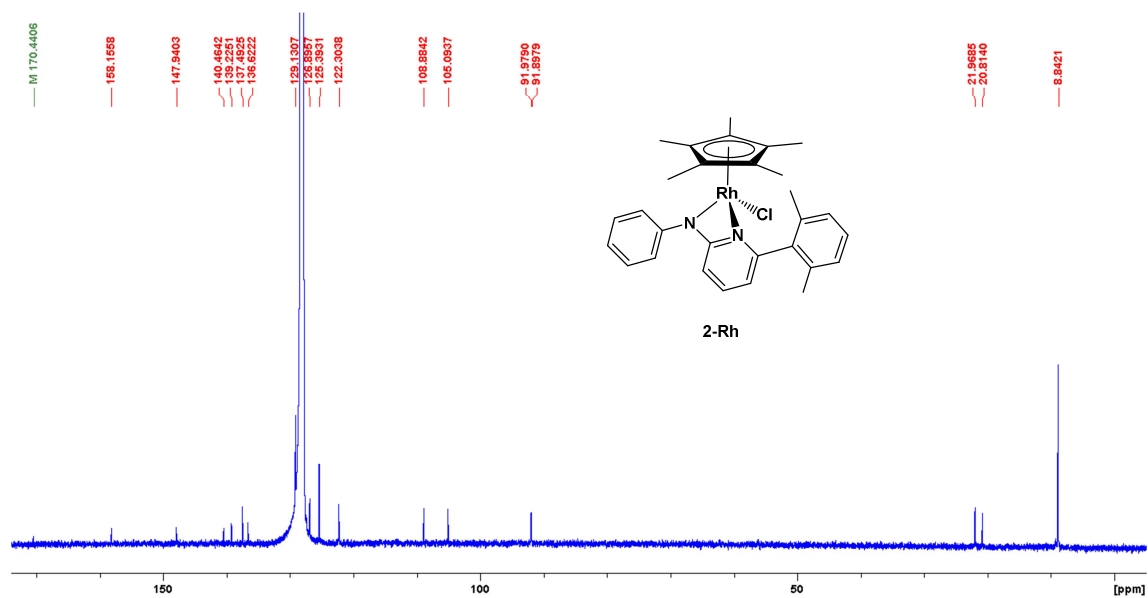
Figure S6. ^{13}C{^{1}H} NMR spectrum (75 MHz, C$_6$D$_6$, 25 °C) of **2-Rh**.
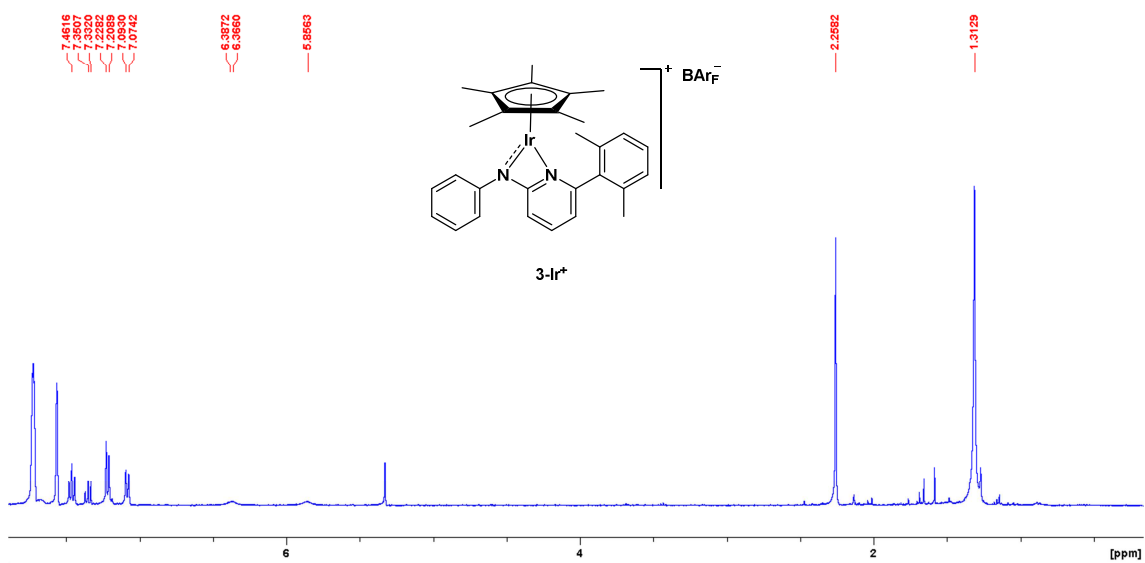
Figure S7. ^{1}H NMR spectrum (400 MHz, CD$_2$Cl$_2$, 25 ºC) of **[3-Ir]BAr$_F$**.
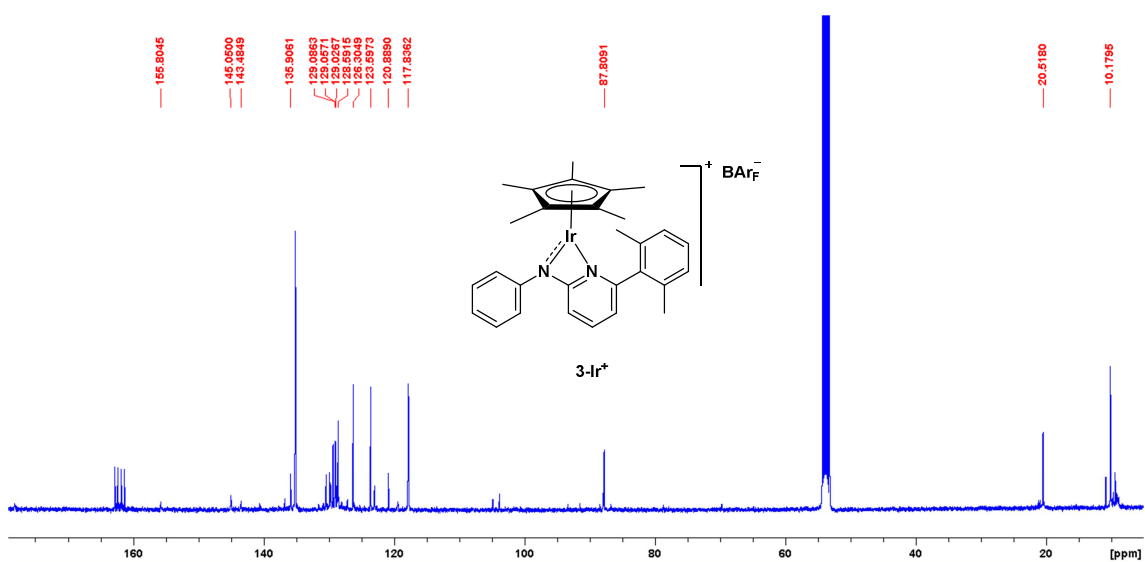
Figure S8. ^{13}C{^{1}H} NMR spectrum (100 MHz, CD$_2$Cl$_2$, 25 ºC) of **[3-Ir]BAr$_F$**.

S8
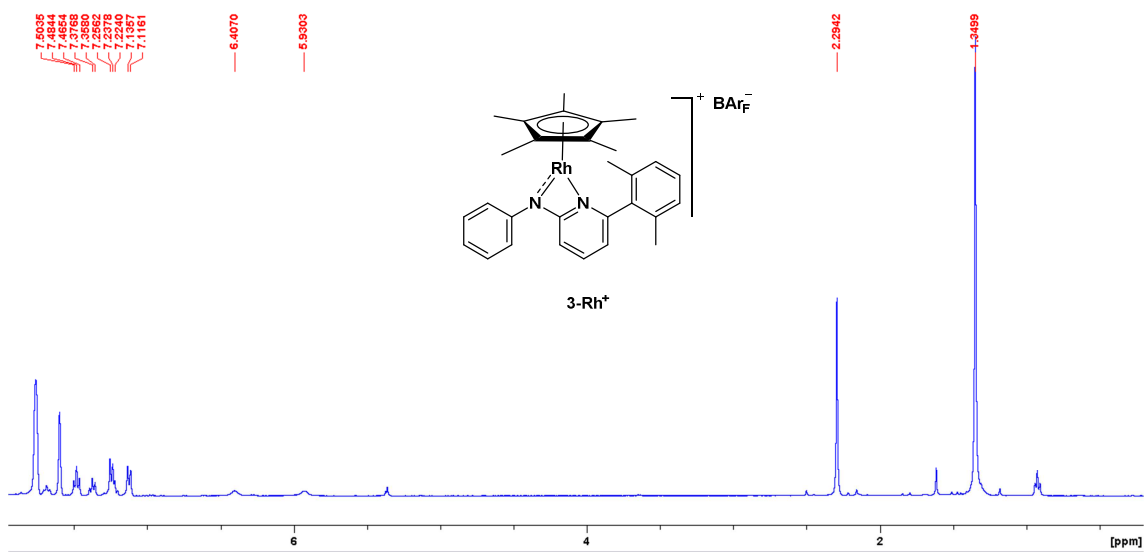
Figure S9. ^{1}H NMR spectrum (500 MHz, CD$_2$Cl$_2$, 25 ℃) of **[3-Rh]BAr$_F$**.
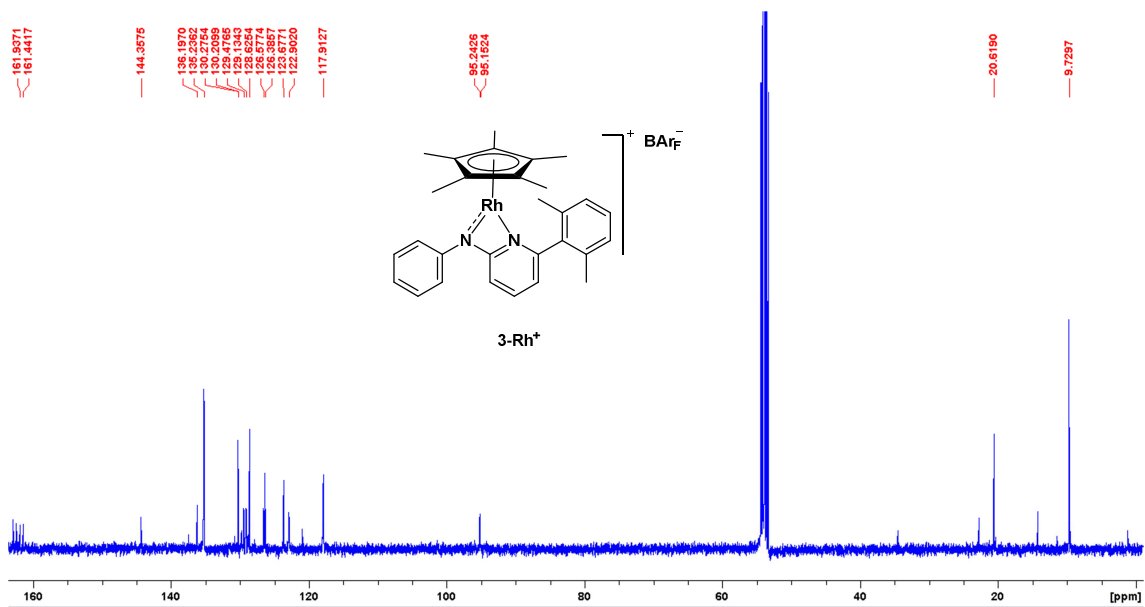
Figure S10. ^{13}C{^{1}H} NMR spectrum (125 MHz, CD$_2$Cl$_2$, 25 ℃) of **[3-Rh]BAr$_F$**.
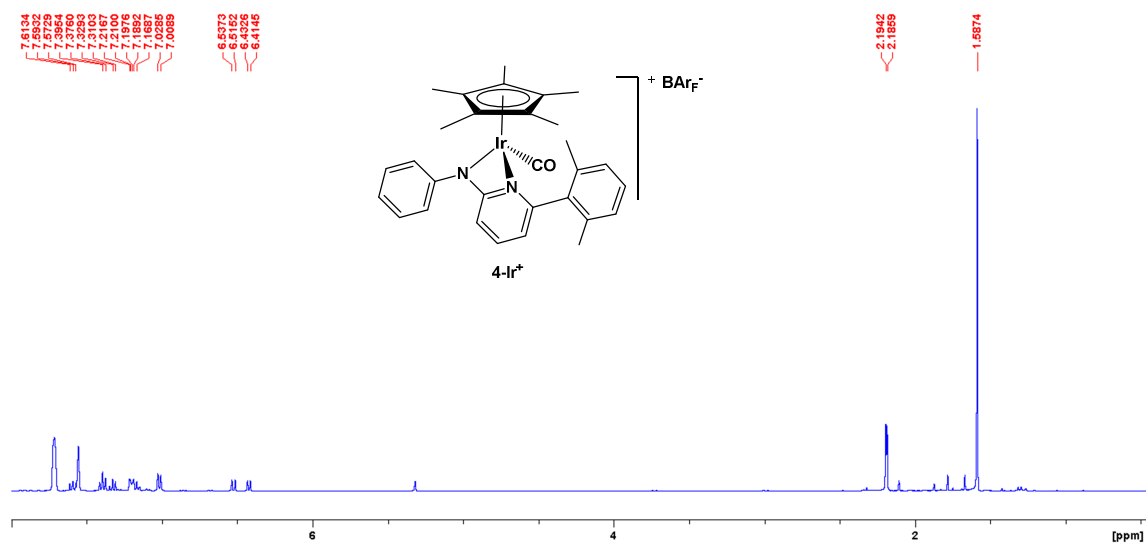
Figure S11. ^{1}H NMR spectrum (400 MHz, CD$_2$Cl$_2$, 25 °C) of **[4-Ir]BAr$_F$**.
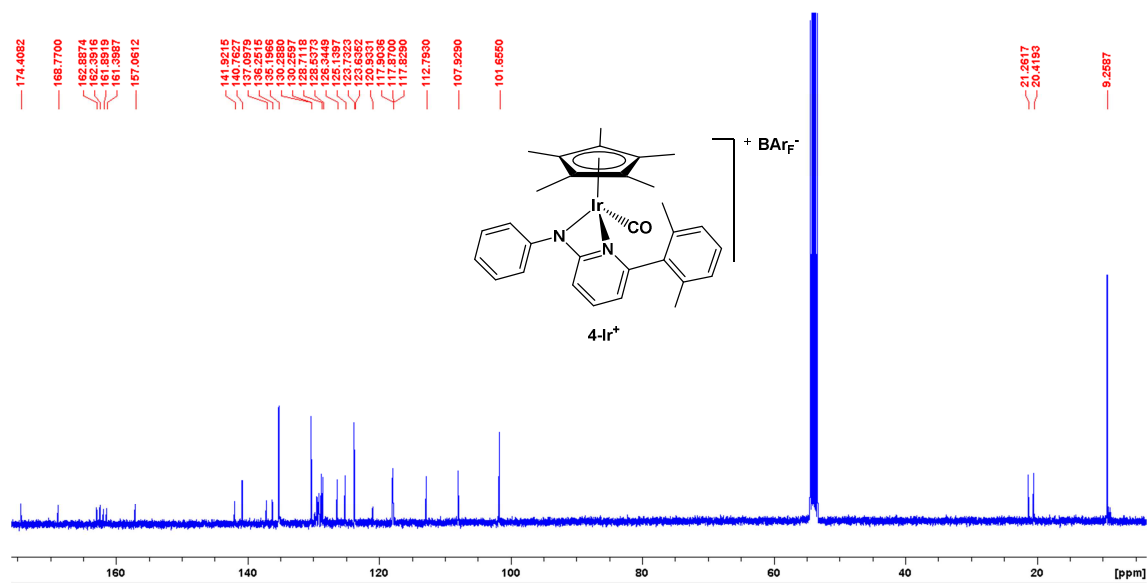
Figure S12. ^{13}C{^{1}H} NMR spectrum (100 MHz, CD$_2$Cl$_2$, 25 °C) of **[4-Ir]BAr$_F$**.
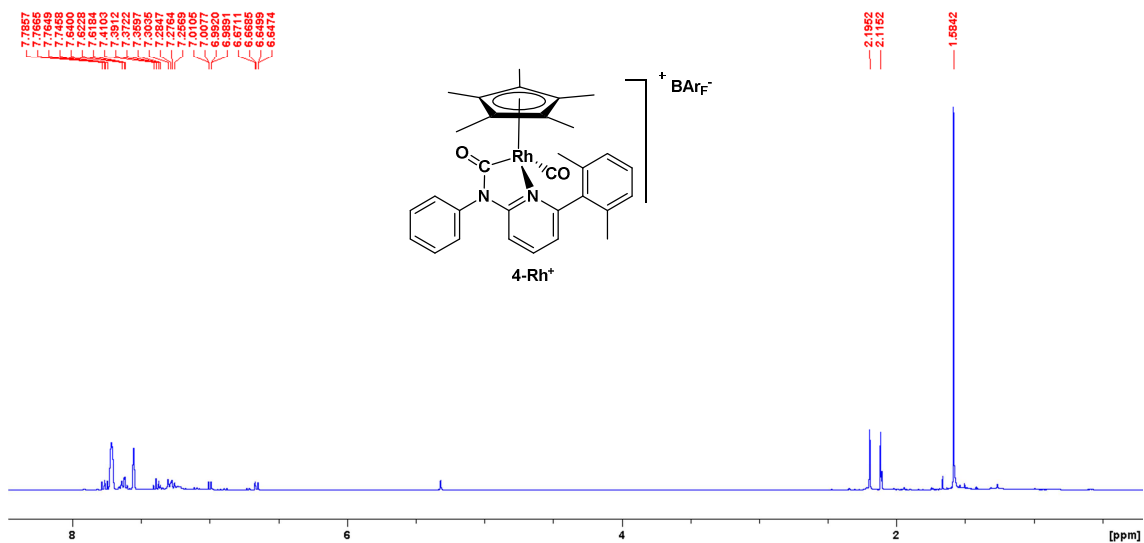
Figure S13. ^{1}H NMR spectrum (400 MHz, CD$_2$Cl$_2$, 25 °C) of **[4-Rh]BAr$_F$**.
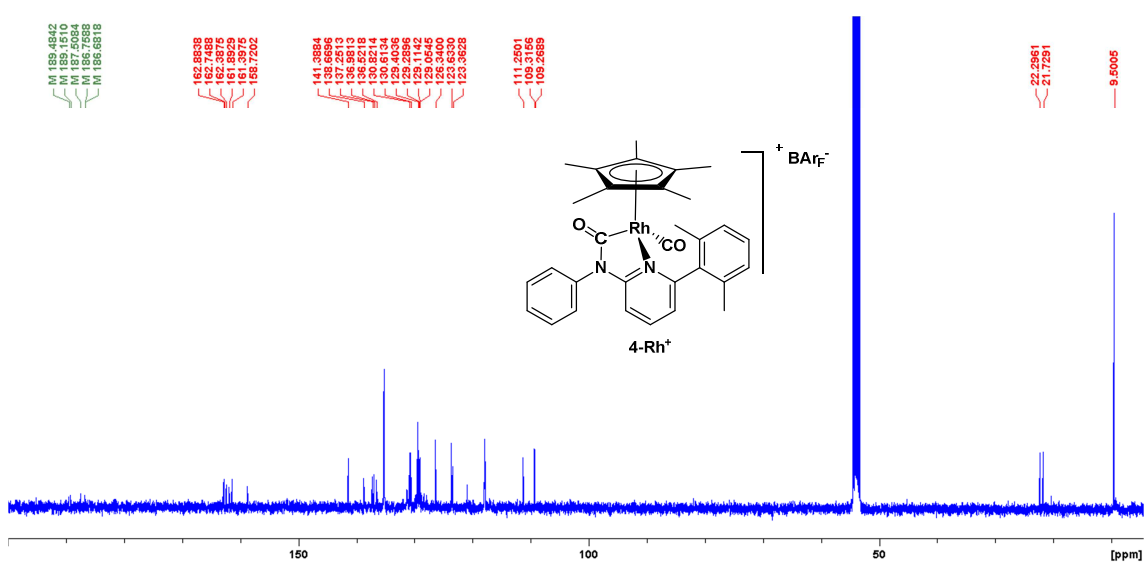
Figure S14. ^{13}C{^{1}H} NMR spectrum (100 MHz, CD$_2$Cl$_2$, 25 °C) of **[4-Rh]BAr$_F$**.
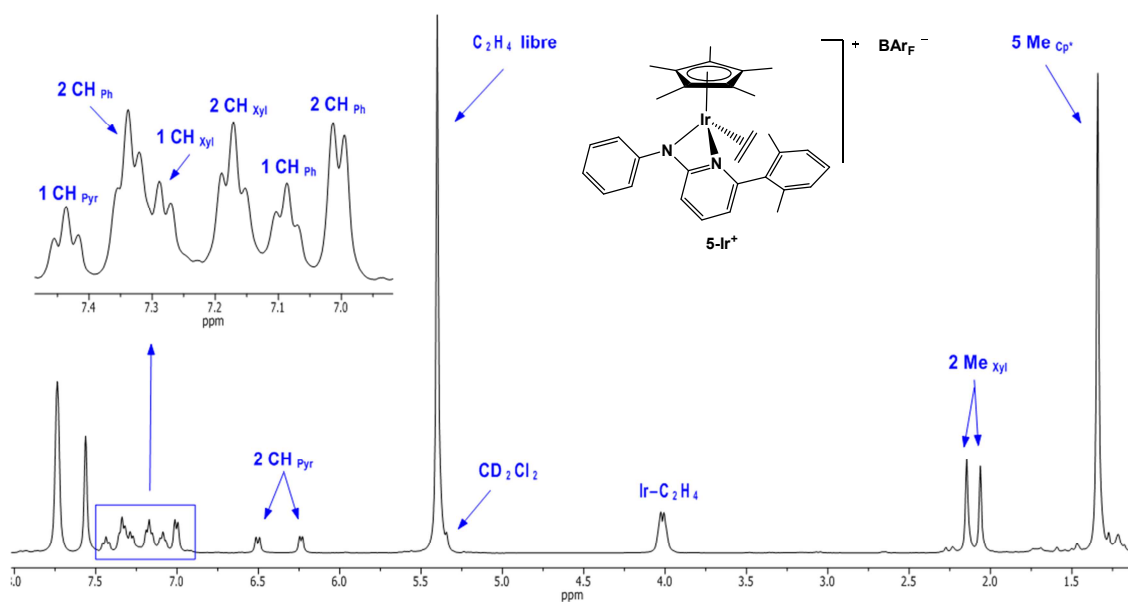
Figure S15. ^{1}H NMR spectrum (400 MHz, CD$_2$Cl$_2$, -40 °C) of **[5-Ir]BAr$_F$**.
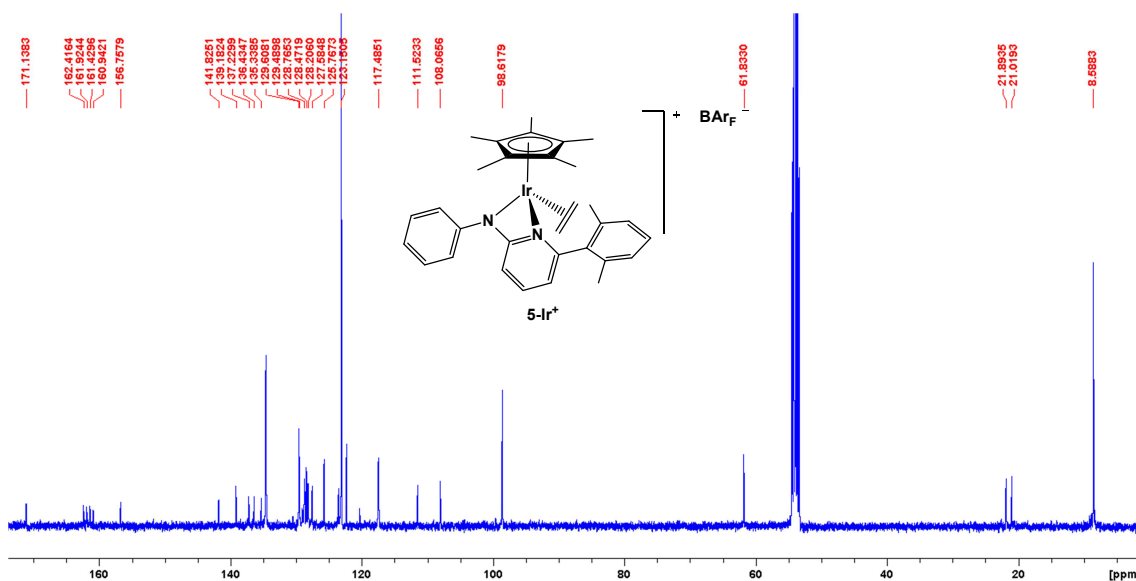
Figure S16. ^{13}C{^{1}H} NMR spectrum (400 MHz, CD$_2$Cl$_2$, -40 °C) of **[5-Ir]BAr$_F$**.
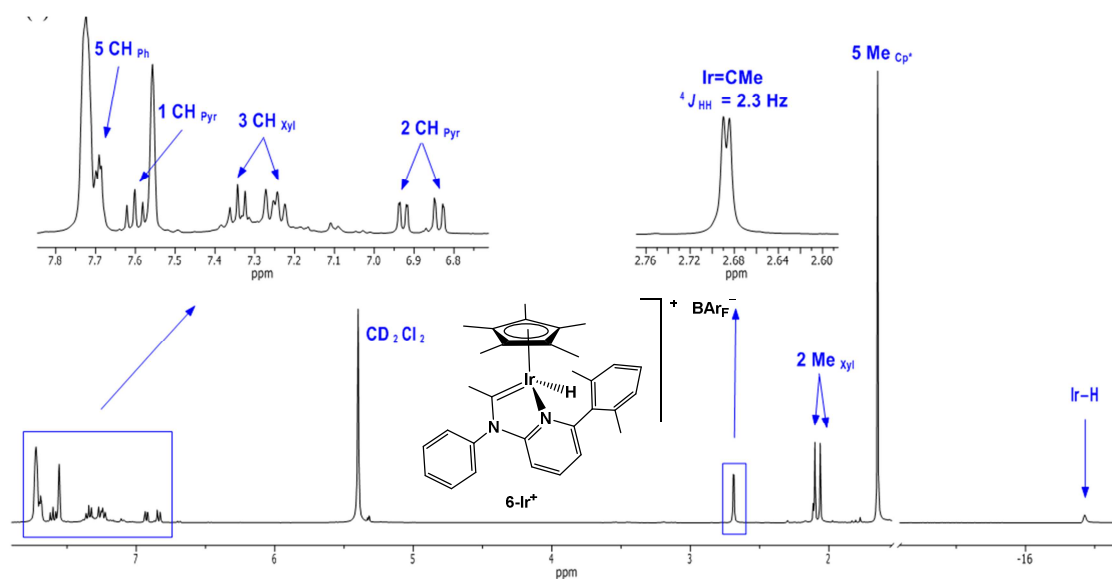
Figure S17. ^{1}H NMR spectrum (400 MHz, CD$_2$Cl$_2$, 25 °C) of **[6-Ir]BAr$_F$**.
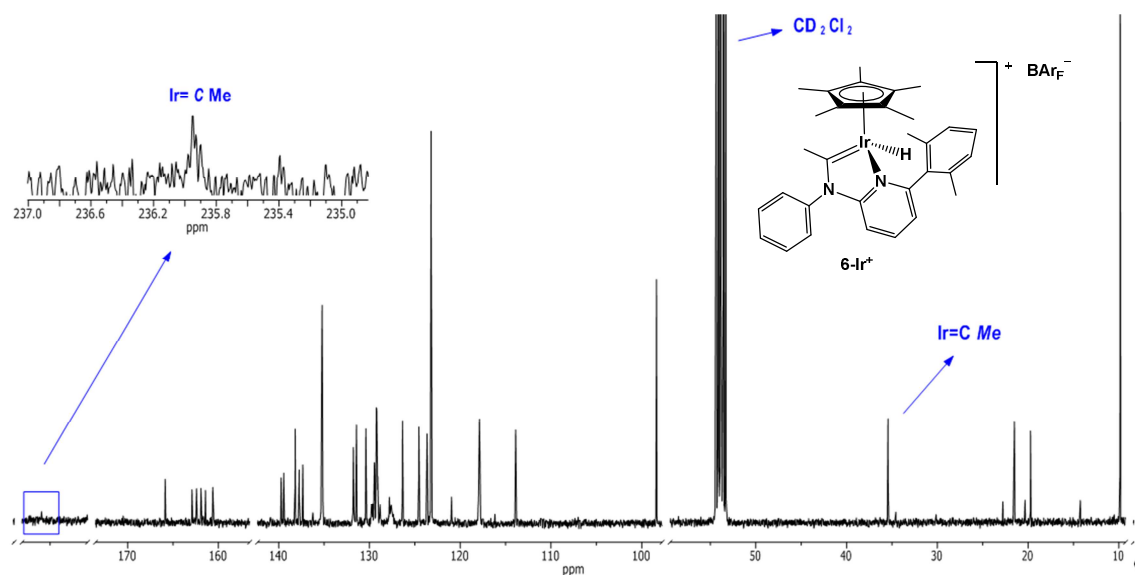
Figure S18. ^{13}C{^{1}H} NMR spectrum (400 MHz, CD$_2$Cl$_2$, 25 °C) of **[6-Ir]BAr$_F$**.
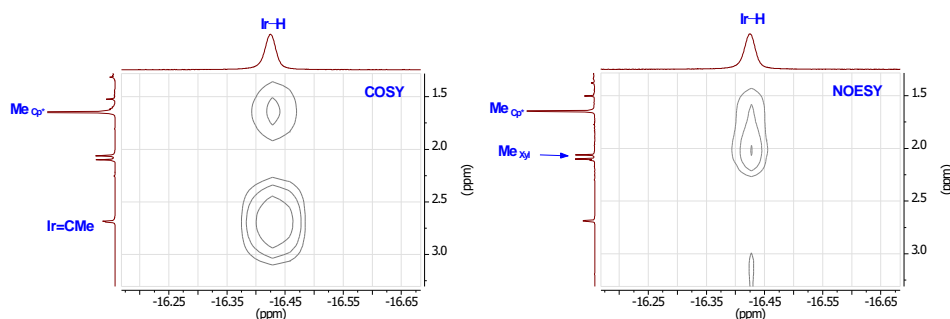
Figure S19. Selected regions of the ^{1}H-^{1}H COSY NMR spectrum (left) and ^{1}H-^{1}H NOESY NMR spectrum (right) of **[6-Ir]BAr$_F$**. (400 MHz, CD$_2$Cl$_2$, 25 °C).
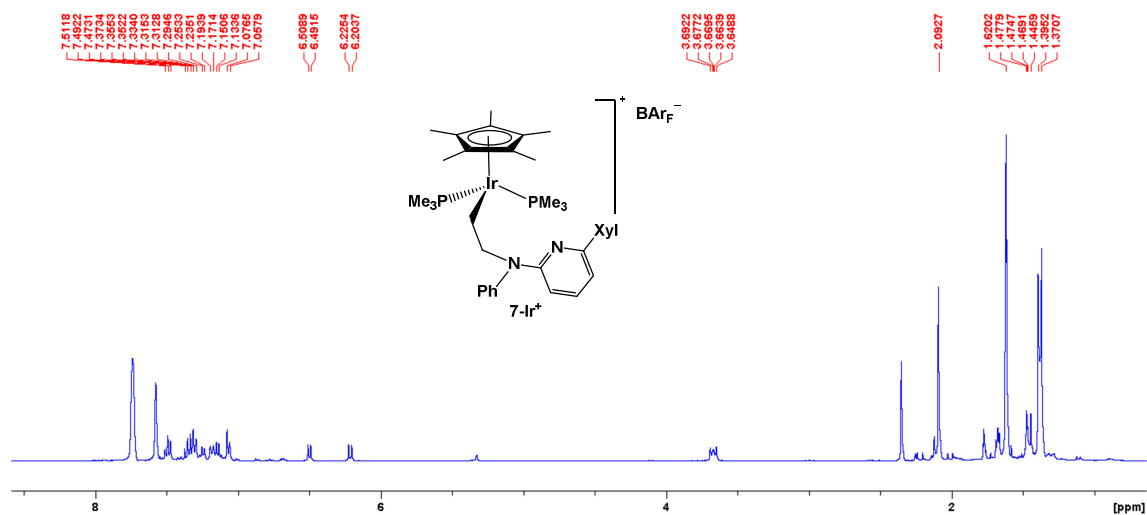
Figure S20. ^{1}H NMR spectrum (400 MHz, CD$_2$Cl$_2$, 25 ℃) of **[7-Ir]BAr$_F$**.
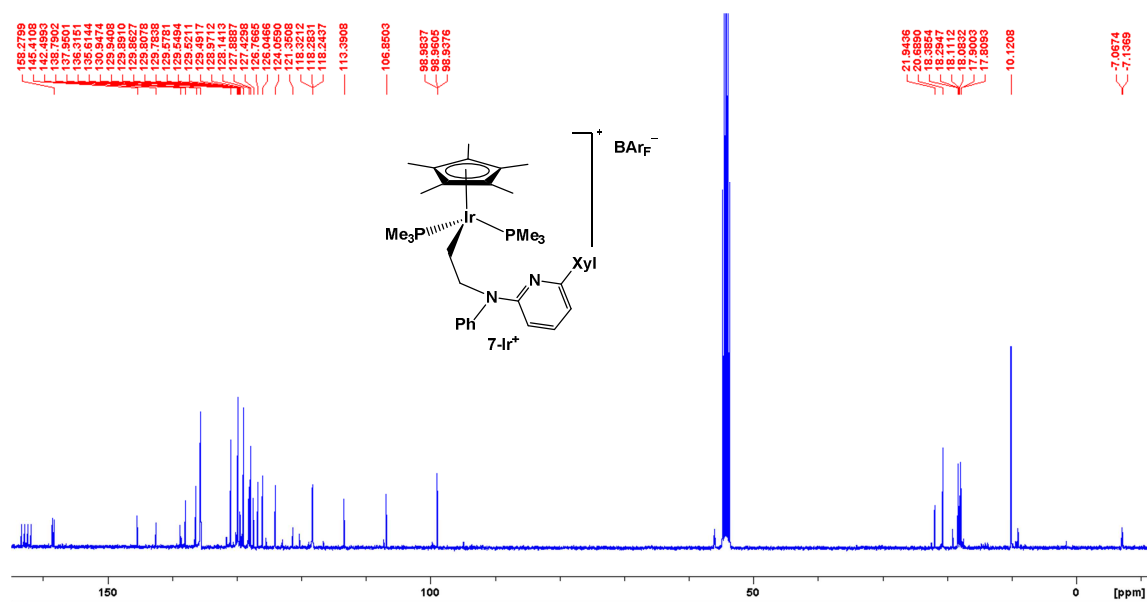
Figure S21. ^{13}C{^{1}H} NMR spectrum (400 MHz, CD$_2$Cl$_2$, 25 ℃) of **[7-Ir]BAr$_F$**.
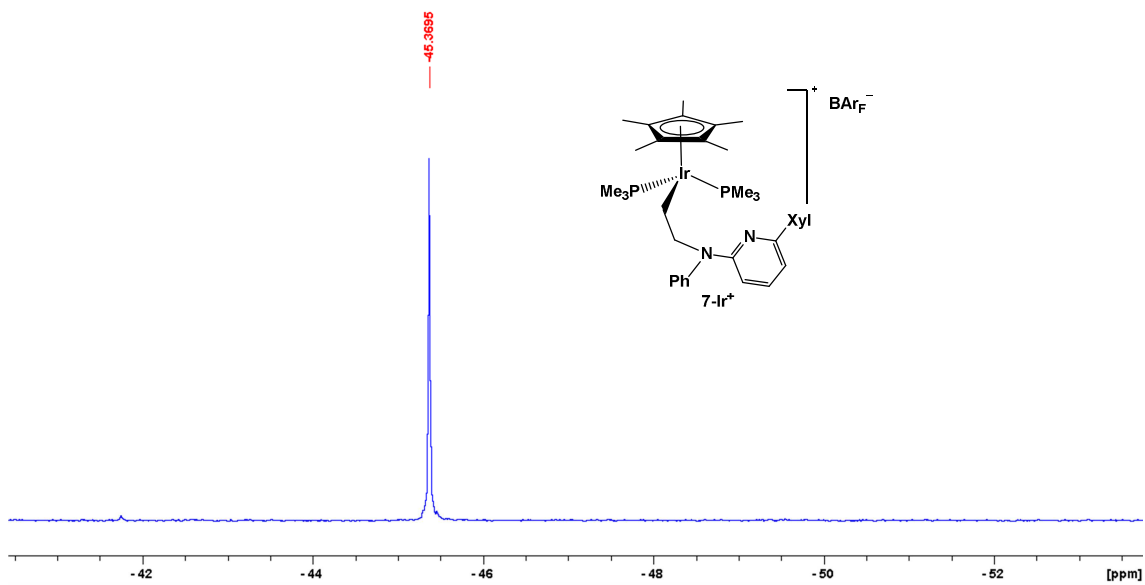
Figure S22. $^{31}P\{^1H\}$ NMR spectrum (400 MHz, CD$_2$Cl$_2$, 25 ºC) of **[7-Ir]BAr$_F$**.
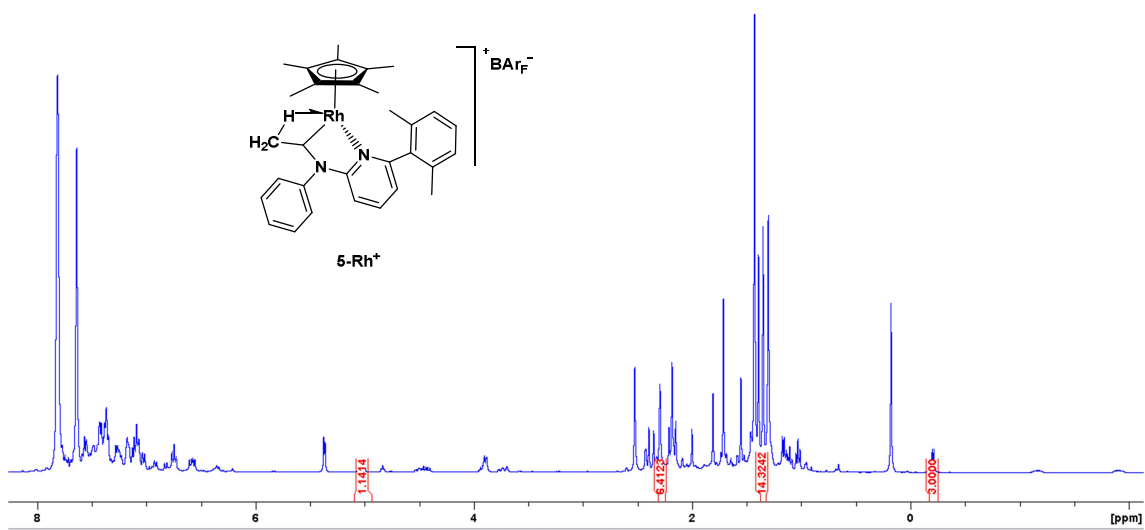
Figure S23. ^1H NMR spectrum (400 MHz, CD$_2$Cl$_2$, 25 ºC) of the crude of the reaction of **[3-Rh]BAr$_F$** with ethylene. Signals attributed to **[5-Rh]BAr$_F$**. are integrated.
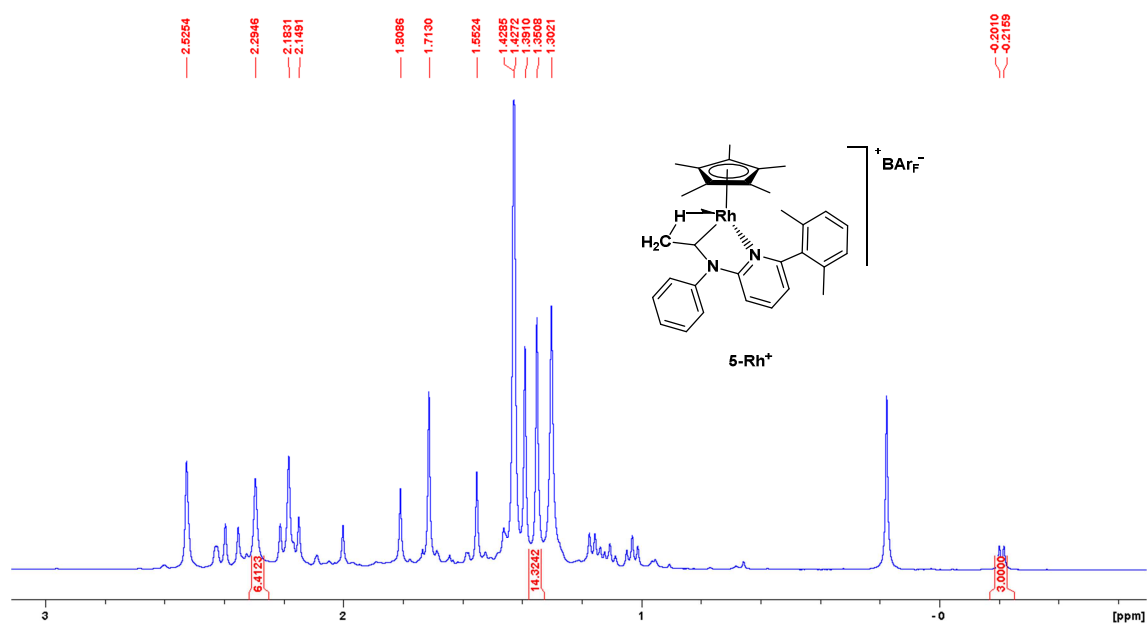
Figure S24. Selected region of the ^{1}H NMR spectrum (400 MHz, CD$_2$Cl$_2$, 25 °C) of the crude of the reaction of **[3-Rh]BAr$_F$**.with ethylene. Signals attributed to **[5-Rh]BAr$_F$** are integrated.
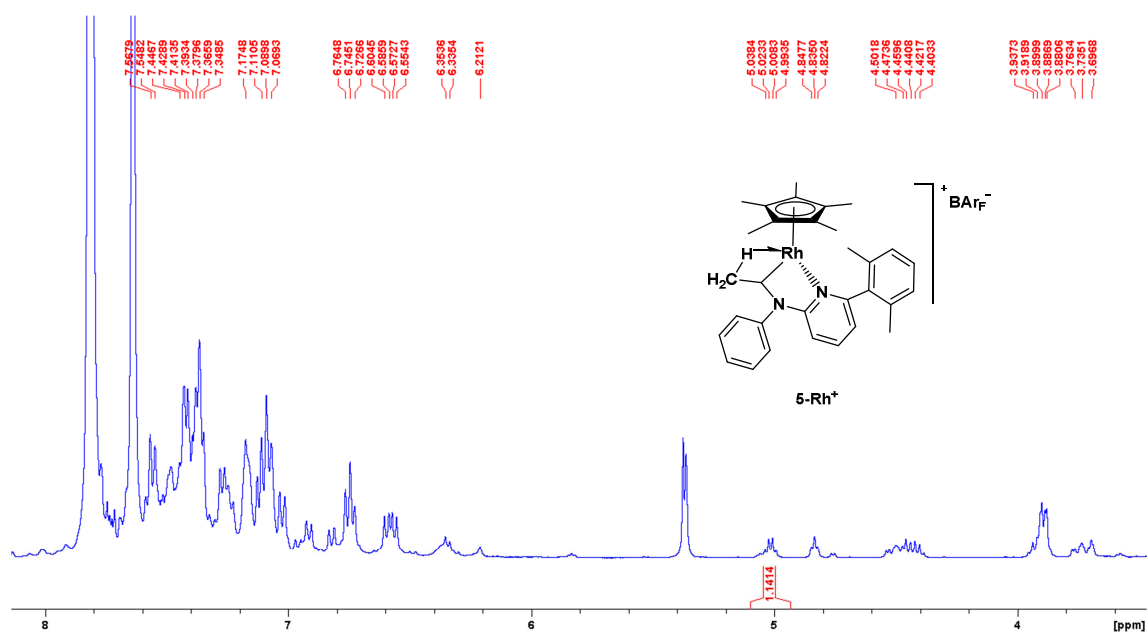
Figure S25. Selected region of the ^{1}H NMR spectrum (400 MHz, CD$_2$Cl$_2$, 25 °C) of the crude of the reaction of **[3-Rh]BAr$_F$** with ethylene. Signals attributed to **[5-Rh]BAr$_F$** are integrated.
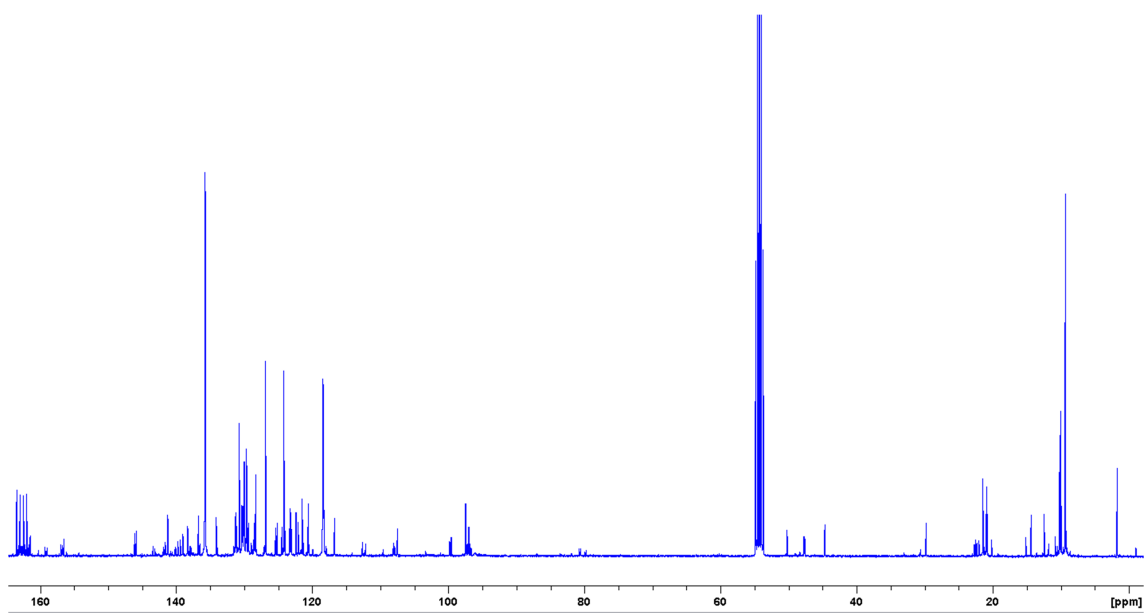
Figure S26. $^{13}C\{^1H\}$ NMR spectrum (125 MHz, CD_2Cl_2, 25 °C) of the crude of the reaction of **[3-Rh]BAr$_F$** with ethylene.
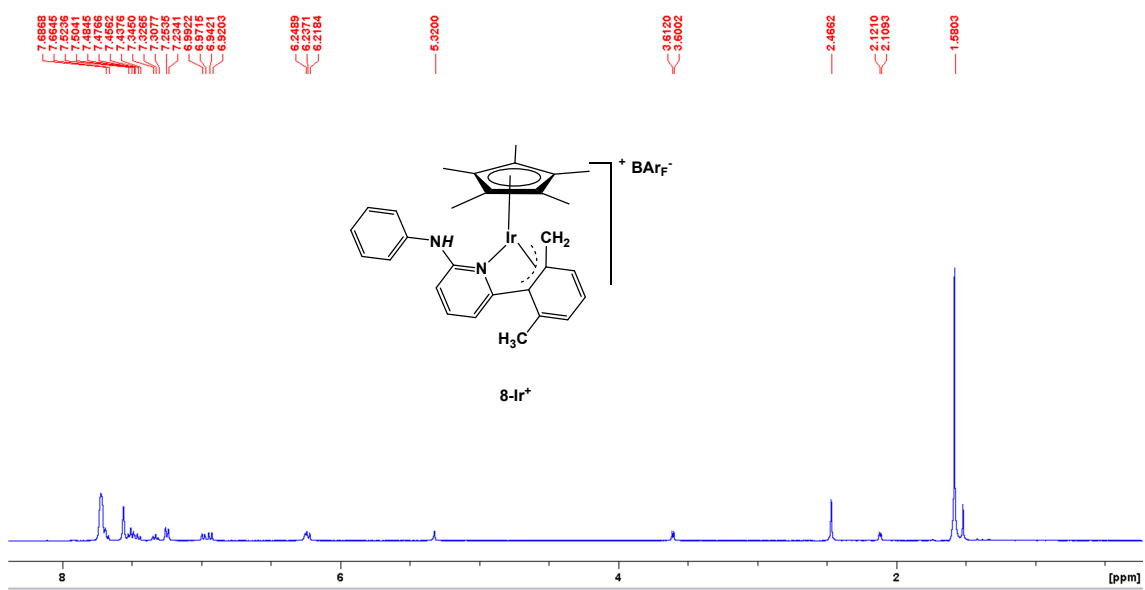
Figure S27. ^1H NMR spectrum (400 MHz, CD_2Cl_2, 25 °C) of **[8-Ir]BAr$_F$**.
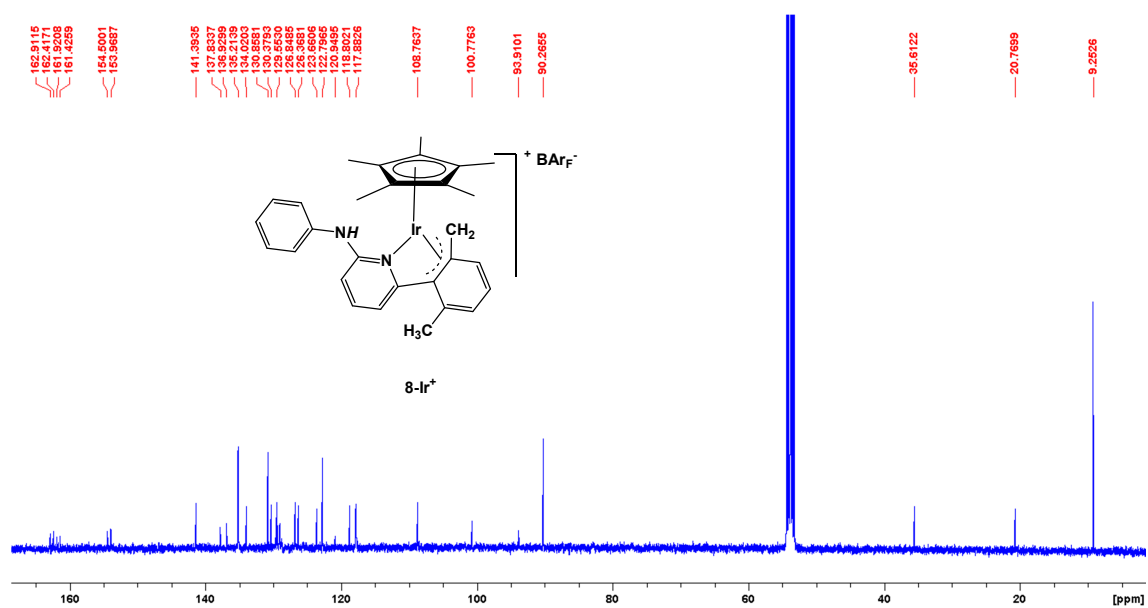
Figure S28. $^{13}C\{^1H\}$ NMR spectrum (400 MHz, CD_2Cl_2, 25 °C) of **[8-Ir]BAr$_F$**.
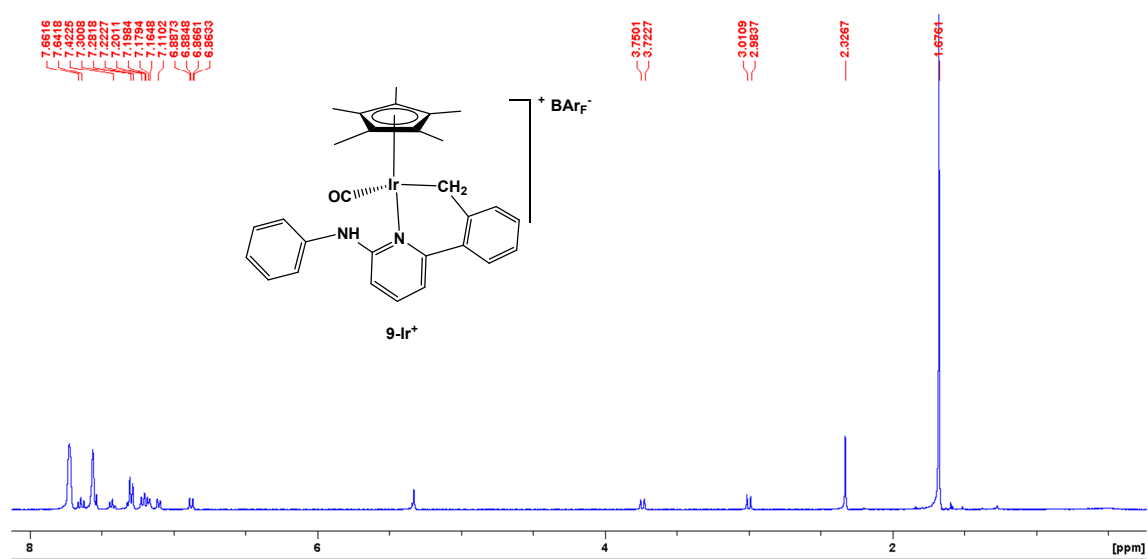
Figure S29. ^1H NMR spectrum (400 MHz, CD_2Cl_2, 25 °C) of **[9-Ir]BAr$_F$**.
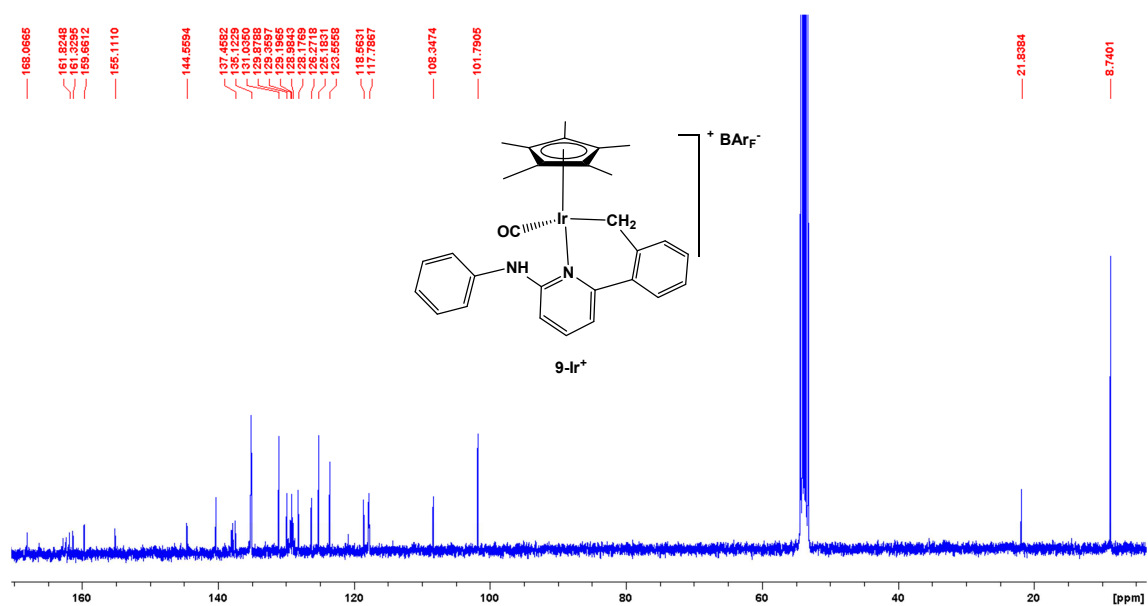
Figure S30. $^{13}C\{^1H\}$ NMR spectrum (400 MHz, CD$_2$Cl$_2$, 25 °C) of **[9-Ir]BAr$_F$**.
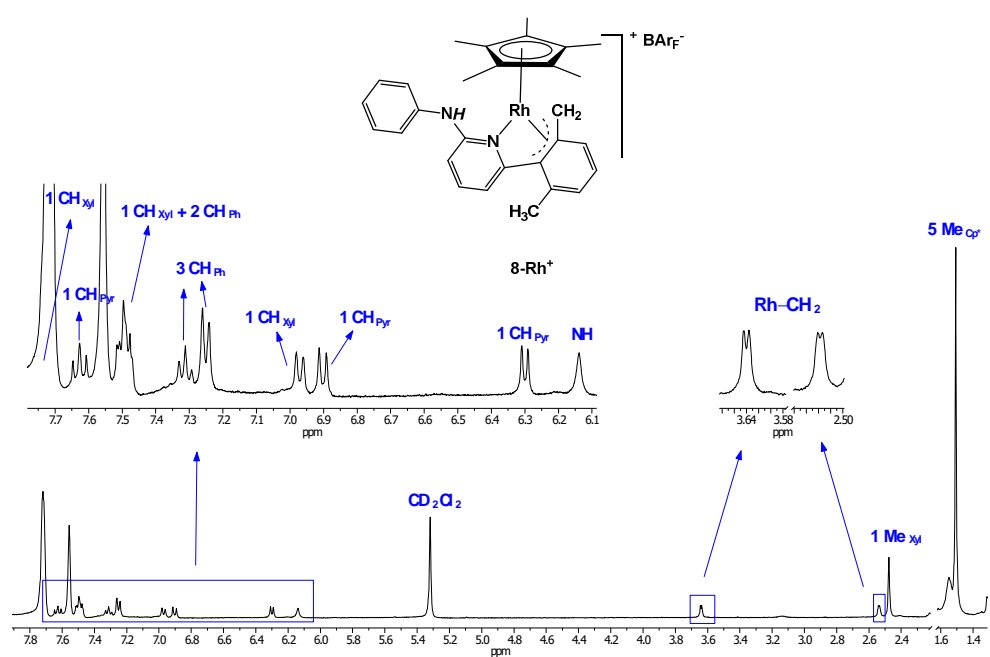
Figure S31. ^1H NMR spectrum (400 MHz, CD$_2$Cl$_2$, 25 °C) of **[8-Rh]BAr$_F$**.
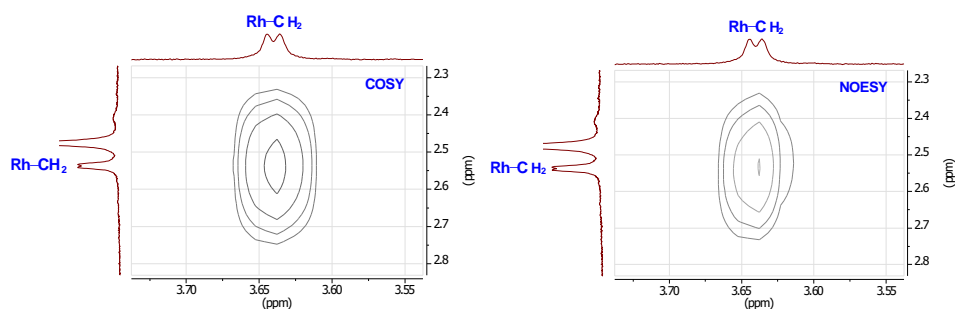
Figure S32. Selected regions of the ^{1}H-^{1}H COSY NMR spectrum (left) and ^{1}H-^{1}H NOESY NMR spectrum (right) of **[8-Rh]BAr$_F$**. (400 MHz, CD$_2$Cl$_2$, 25 ºC).
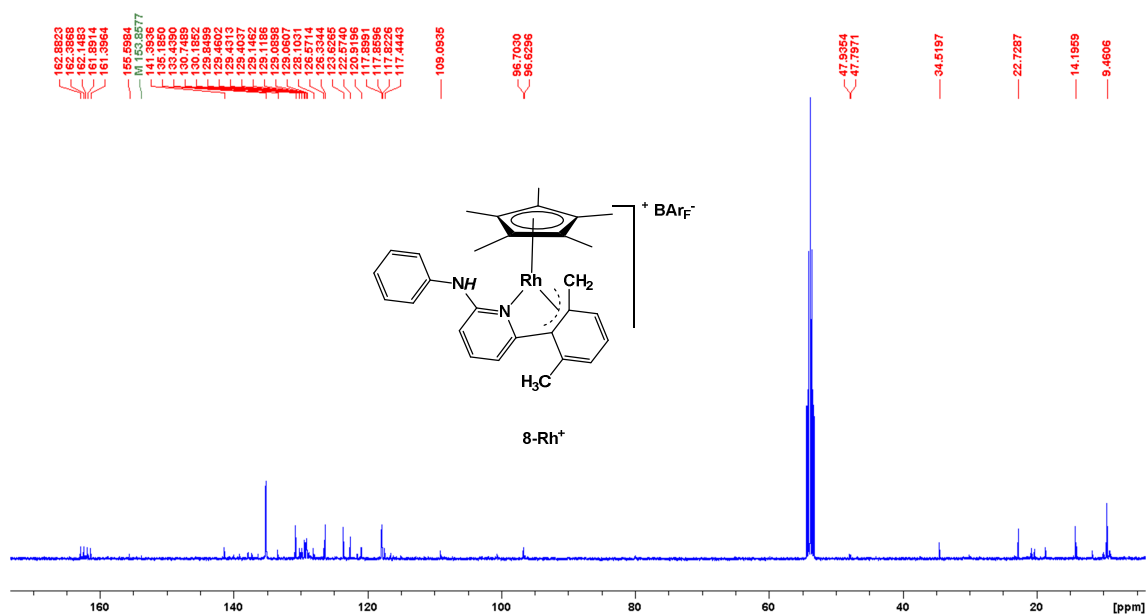
Figure S33. ^{13}C{^{1}H} NMR spectrum (400 MHz, CD$_2$Cl$_2$, 25 ºC) of **[8-Rh]BAr$_F$**..
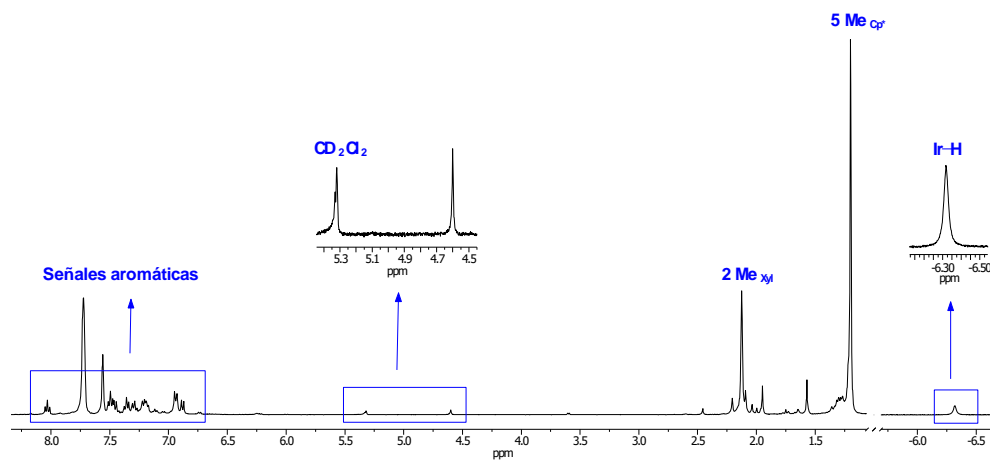
Figure S34. ^{1}H NMR spectrum (400 MHz, CD$_2$Cl$_2$, 25 ºC) of a hydride intermediate in the reaction of **[3-Ir]BAr$_F$** with excess of dihydrogen.

IV. X-RAY STRUCTURE ANALYSIS:

Crystals of suitable size for X-ray diffraction analysis were coated with dry perfluoropolyether and mounted on glass fibers and fixed in a cold nitrogen stream (T = 100 K) to the goniometer head. Data collection was performed on a Bruker-Nonius X8Apex-II CCD diffractometer, using monochromatic radiation λ(Mo K$_\alpha$) = 0.71073 Å, by means of ω and φ scans with a width of 0.50 degree. The data were reduced (SAINT)[1] and corrected for absorption effects by the multi-scan method (SADABS)[2]. The structures were solved by direct methods (SIR-2002)[3] and refined against all F^2 data by full-matrix least-squares techniques (SHELXTL-6.12)[4] minimizing $w[F_o^2-F_c^2]^2$. All the non-hydrogen atoms were refined anisotropically, while C-H hydrogen atoms were placed in geometrically calculated positions using a riding model. The N-H hydrogen atoms were localized by difference Fourier maps and refined fixing their bond lengths at the end of the refinement. Some geometric restraints (SADI and DFIX commands), the ADP restraint SIMU and the rigid bond restraint DELU were used to make the geometric and ADP values of the disordered atoms (-CF$_3$ groups in **BAr$_F$** anions) more reasonable. A search for solvent accessible voids in the crystal structures **[5-Rh]BAr$_F$** and **[7-Ir]BAr$_F$** using PLATON,[5] showed a potential solvent volume, impossible to model even with the most severe restraints. The corresponding CIF data represent SQUEEZE[6] treated structures, with the undefined solvent excluded from the structural model. The SQUEEZE results were appended to the CIF.

CCDC 1572330 (**2-Ir**), 1572331 (**2-Rh**), 1572332 (**[3-Ir]BAr$_F$**), 1572333 (**[4-Ir]BAr$_F$**), 1572334 (**[4-Rh]BAr$_F$**), 1572335 (**[5-Rh]BAr$_F$**), 1572336 (**[6-Ir]BAr$_F$**), 1572337 (**[7-Ir]BAr$_F$**), 1572338 (**[8-Ir]BAr$_F$**), 1572339 (**[8-Rh]BAr$_F$**).

X-Ray data for 2-Ir
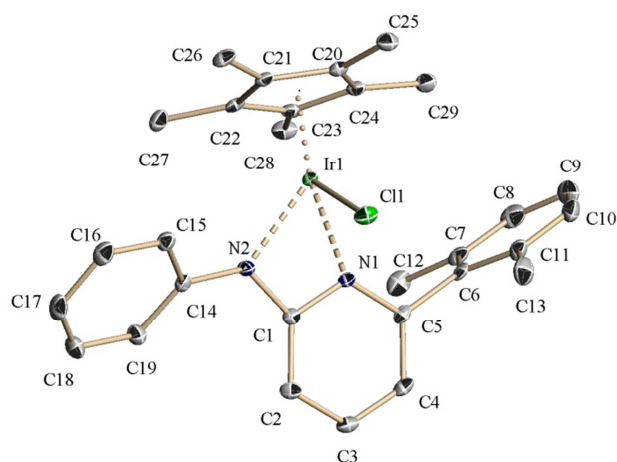
Figure S35. ORTEP view of molecular structure of complex **2-Ir** with thermal ellipsoids drawn at the 30% level. The hydrogen atoms are omitted by clarity.

Table S1. Selected bond lengths [Å] and angles [°] for **2-Ir**

Bond Distances (Å)			
Ir(1)–N(1)	2.175(2)	Ir(1)–C(21)	2.141(3)
Ir(1)–N(2)	2.092(2)	Ir(1)–C(22)	2.138(3)
Ir(1)–Cl(1)	2.3940(7)	Ir(1)–C(23)	2.167(3)
Ir(1)–C(20)	2.180(3)	Ir(1)–C(24)	2.190(3)
Bond Angles (°)			
N(1)-Ir(1)-Cl(1)	84.92(7)	C(1)-N(2)-Ir(1)	97.91(17)
N(2)-Ir(1)-Cl(1)	85.98(7)	C(1)-N(1)-Ir(1)	93.66(16)
N(2)-Ir(1)-N(1)	61.10(9)	N(2)-C(1)-N(1)	106.5(2)

Table S2. Crystal data and structure refinement for **2-Ir**.

|	
Empirical formula	$C_{29}H_{32}ClIrN_2$
Formula weight	636.22
Temperature	173(2) K
Wavelength	0.71073 Å
Crystal system	Monoclinic
Space group	P 2_1/c
Unit cell dimensions	a = 14.4731(7) Å α = 90°.
	b = 7.9759(3) Å β = 91.1950(10)°.
	c = 22.2870(11) Å γ = 90°.
Volume	2572.2(2) $Å^3$
Z	4
Density (calculated)	1.643 Mg/m^3
Absorption coefficient	5.314 mm^{-1}
F(000)	1256
Crystal size	0.15 x 0.10 x 0.08 mm^3
Theta range for data collection	2.28 to 25.25°.
Index ranges	-17<=h<=17, -9<=k<=9, -26<=l<=26
Reflections collected	26382
Independent reflections	4485 [R(int) = 0.0326]
Completeness to theta = 25.25°	99.1 %
Absorption correction	Semi-empirical from equivalents
Max. and min. transmission	0.6558 and 0.5328
Refinement method	Full-matrix least-squares on F^2
Data / restraints / parameters	4485 / 0 / 305
Goodness-of-fit on F^2	1.041
Final R indices [I>2sigma(I)]	R1 = 0.0189, wR2 = 0.0476
R indices (all data)	R1 = 0.0239, wR2 = 0.0490
Largest diff. peak and hole	1.414 and -1.116 e.$Å^{-3}$

X-Ray data for 2-Rh
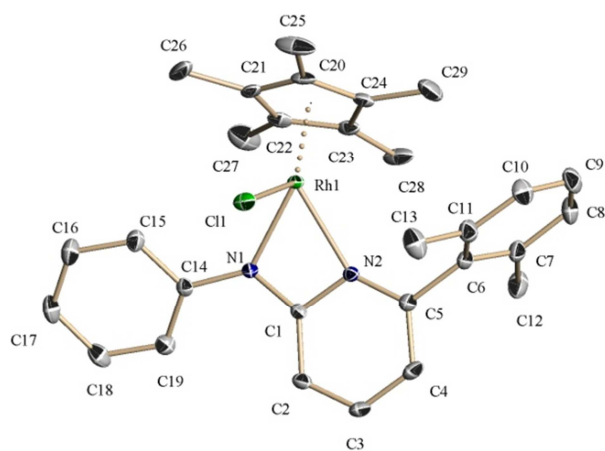
Figure S36. ORTEP view of molecular structure of complex **2-Rh** with thermal ellipsoids drawn at the 30% level. The hydrogen atoms are omitted by clarity.

Table S3. Selected bond lengths [Å] and angles [°] for **2-Rh**

Bond distances (Å)			
Rh(1)–N(1)	2.1114(19)	Rh(1)–C(21)	2.130(2)
Rh(1)–N(2)	2.1705(19)	Rh(1)–C(22)	2.147(2)
Rh(1)–Cl(1)	2.4057(6)	Rh(1)–C(23)	2.128(2)
Rh(1)–C(20)	2.166(2)	Rh(1)–C(24)	2.178(2)
Angles (°)			
N(1)-Rh(1)-Cl(1)	87.64(5)	C(1)-N(2)-Rh(1)	93.33(13)
N(2)-Rh(1)-Cl(1)	91.87(5)	C(1)-N(1)-Rh(1)	96.67(14)
N(1)-Rh(1)-N(2)	61.66(7)	N(1)-C(1)-N(2)	107.64(18)

Table S4. Crystal data and structure refinement for **2-Rh**.

|	
Empirical formula	$C_{30}H_{34}Cl_3N_2Rh$
$[C_{29}H_{32}ClN_2Rh, CH_2Cl_2]$	
Formula weight	631.85
Temperature	173(2) K
Wavelength	0.71073 Å
Crystal system	Orthorhombic
Space group	P 2_1 2_1 2_1
Unit cell dimensions	a = 7.4168(3) Å $\quad$ α= 90°.
	b = 14.4271(6) Å $\quad$ β= 90°.
	c = 26.7421(11) Å $\quad$ γ = 90°.
Volume	2861.5(2) Å^3
Z	4
Density (calculated)	1.467 Mg/m^3
Absorption coefficient	0.899 mm^{-1}
F(000)	1296
Crystal size	0.48 x 0.14 x 0.12 mm^3
Theta range for data collection	2.08 to 25.25°.
Index ranges	-8<=h<=8, -15<=k<=17, -15<=l<=32
Reflections collected	16202
Independent reflections	4934 [R(int) = 0.0183]
Completeness to theta = 25.25°	98.9 %
Absorption correction	Semi-empirical from equivalents
Max. and min. transmission	0.8978 and 0.8602
Refinement method	Full-matrix least-squares on F^2
Data / restraints / parameters	4934 / 54 / 350
Goodness-of-fit on F^2	1.074
Final R indices [I>2sigma(I)]	R1 = 0.0205, wR2 = 0.0491
R indices (all data)	R1 = 0.0214, wR2 = 0.0495
Absolute structure parameter	0.02(2)
Largest diff. peak and hole	0.453 and -0.277 e.Å^{-3}

X-Ray data for [3-Ir]BAr_F
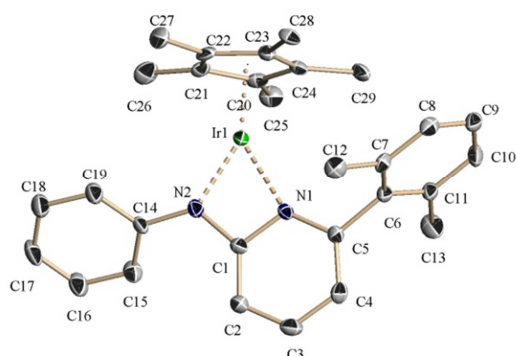
Figure S37. ORTEP view of molecular structure of complex **[3-Ir]BAr_F** with thermal ellipsoids drawn at the 30% level. The hydrogen atoms are omitted by clarity.

Table S5. Selected bond lengths [Å] and angles [°] for **[3-Ir]BAr_F**.

Bond Distances (Å)			
Ir(1)–N(1)	2.109(6)	Ir(1)–C(22)	2.158(7)
Ir(1)–N(2)	1.972(6)	Ir(1)–C(23)	2.176(7)
Ir(1)–C(20)	2.133(8)	Ir(1)–C(24)	2.194(7)
Ir(1)–C(21)	2.155(7)		
Bond Angles (º)			
N(2)-Ir(1)-N(1)	64.3(2)	C(1)-N(1)-Ir(1)	93.2(4)
C(1)-N(2)-Ir(1)	98.2(4)	N(1)-C(1)-N(2)	104.3(6)

Table S6. Crystal data and structure refinement for **[3-Ir]BAr$_F$**.

|	
Empirical formula	C$_{67}$H$_{58}$BF$_{24}$IrN$_2$
[C$_{29}$H$_{32}$IrN$_2$, C$_{32}$H$_{12}$BF$_{24}$, C$_6$H$_{14}$]	
Formula weight	1550.16
Temperature	173(2) K
Wavelength	0.71073 Å
Crystal system	Monoclinic
Space group	P 2$_1$/n
Unit cell dimensions	a = 16.2879(12) Å α= 90°.
	b = 19.0510(13) Å β= 91.720(2)°.
	c = 21.0781(12) Å γ = 90°.
Volume	6537.6(8) Å^3
Z	4
Density (calculated)	1.575 Mg/m^3
Absorption coefficient	2.153 mm^{-1}
F(000)	3088
Crystal size	0.40 x 0.20 x 0.20 mm^3
Theta range for data collection	2.14 to 25.25°.
Index ranges	-15<=h<=19, -22<=k<=22, -25<=l<=25
Reflections collected	63628
Independent reflections	11705 [R(int) = 0.0981]
Completeness to theta = 25.25°	98.8 %
Absorption correction	Semi-empirical from equivalents
Max. and min. transmission	0.6507 and 0.6017
Refinement method	Full-matrix-block least-squares on F^2
Data / restraints / parameters	11705 / 386 / 865
Goodness-of-fit on F^2	1.037
Final R indices [I>2sigma(I)]	R1 = 0.0534, wR2 = 0.1319
R indices (all data)	R1 = 0.0949, wR2 = 0.1447
Largest diff. peak and hole	2.015 and -1.143 e.Å^{-3}

X-Ray data for [4-Ir]BAr_F
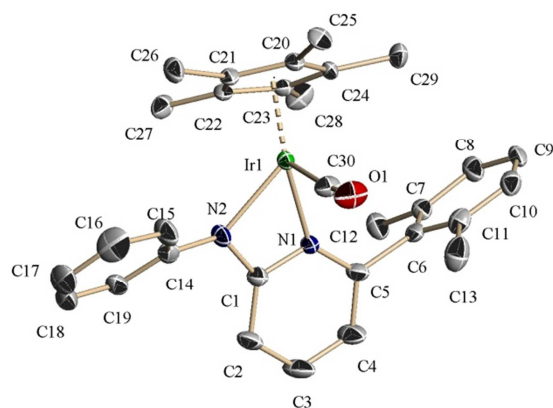
Figure S38. ORTEP view of molecular structure of complex **[4-Ir]BAr_F** with thermal ellipsoids drawn at the 30% level. The hydrogen atoms are omitted by clarity.

Table S7. Selected bond lengths [Å] and angles [°] for **[4-Ir]BAr_F**.

Bond Distances (Å)			
Ir(1)–N(1)	2.137(7)	Ir(1)–C(21)	2.163(6)
Ir(1)–N(2)	2.089(6)	Ir(1)–C(22)	2.232(7)
Ir(1)–C(30)	1.874(8)	Ir(1)–C(23)	2.259(8)
O(1)–C(30)	1.145(9)	Ir(1)–C(24)	2.216(10)
Ir(1)–C(20)	2.181(7)		
Bond Angles (°)			
C(30)-Ir(1)-N(1)	94.2(3)	C(1)-N(1)-Ir(1)	94.3(5)
C(30)-Ir(1)-N(2)	94.5(3)	C(1)-N(2)-Ir(1)	96.3(5)
N(2)-Ir(1)-N(1)	62.0(2)	N(1)-C(1)-N(2)	107.1(8)

Table S8. Crystal data and structure refinement for **[4-Ir]BAr$_F$**.

|	
Empirical formula	$C_{62}H_{44}BF_{24}IrN_2O$
Formula weight	1492.00
Temperature	173(2) K
Wavelength	0.71073 Å
Crystal system	Monoclinic
Space group	C c
Unit cell dimensions	a = 21.926(4) Å $\quad$ α= 90°.
	b = 12.715(3) Å $\quad$ β= 96.81(3)°.
	c = 21.804(4) Å $\quad$ γ = 90°.
Volume	6036(2) Å^3
Z	4
Density (calculated)	1.642 Mg/m^3
Absorption coefficient	2.330 mm^{-1}
F(000)	2944
Crystal size	0.45 x 0.25 x 0.20 mm^3
Theta range for data collection	1.85 to 25.25°.
Index ranges	-21<=h<=26, -15<=k<=15, -26<=l<=26
Reflections collected	42088
Independent reflections	9974 [R(int) = 0.0333]
Completeness to theta = 25.25°	100.0 %
Absorption correction	Semi-empirical from equivalents
Max. and min. transmission	0.6280 and 0.5024
Refinement method	Full-matrix-block least-squares on F^2
Data / restraints / parameters	9974 / 266 / 827
Goodness-of-fit on F^2	1.040
Final R indices [I>2sigma(I)]	R1 = 0.0333, wR2 = 0.0871
R indices (all data)	R1 = 0.0352, wR2 = 0.0882
Absolute structure parameter	0.019(6)
Largest diff. peak and hole	1.530 and -0.739 e.Å^{-3}

X-Ray data for [4-Rh]BAr_F
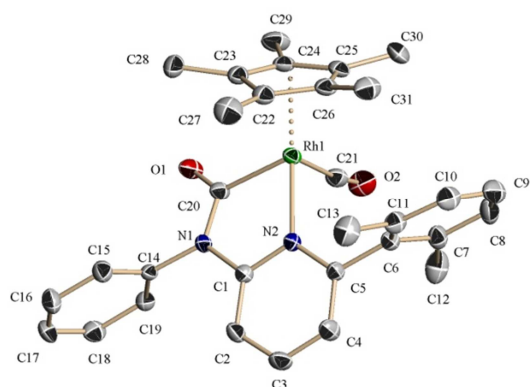
Figure S39. ORTEP view of molecular structure of complex **[4-Rh]BAr_F** with thermal ellipsoids drawn at the 30% level. The hydrogen atoms are omitted by clarity.

Table S9. Selected bond lengths (Å) and angles (°) for **[4-Rh]BAr_F**.

Bond distances (Å)

Rh(1)–N(2)	2.152(3)	Rh(1)–C(22)	2.235(5)
Rh(1)–C(21)	1.908(5)	Rh(1)–C(23)	2.251(5)
O(2)–C(21)	1.115(6)	Rh(1)–C(24)	2.157(4)
Rh(1)–C(20)	2.026(4)	Rh(1)–C(25)	2.262(4)
O(1)–C(20)	1.200(5)	Rh(1)–C(26)	2.333(5)

Angles (°)

C(21)-Rh(1)-N(2)	94.55(17)	N(1)-C(20)-Rh(1)	111.9(3)
C(21)-Rh(1)-C(20)	88.9(2)	C(1)-N(2)-Rh(1)	112.5(3)
C(20)-Rh(1)-N(2)	79.13(15)	N(2)-C(1)-N(1)	115.0(4)

Table S10. Crystal data and structure refinement for **[4-Rh]BAr$_F$**.

|	
Empirical formula	$C_{64}H_{46}BCl_2F_{24}N_2O_2Rh$
	$[C_{32}H_{12}BF_{24}, C_{31}H_{32}N_2O_2Rh, CH_2Cl_2]$
Formula weight	1515.65
Temperature	173(2) K
Wavelength	0.71073 Å
Crystal system	Monoclinic
Space group	P 2$_1$/c
Unit cell dimensions	a = 20.3592(8) Å α= 90°.
	b = 16.6299(6) Å β= 108.0170(10)°.
	c = 19.9031(9) Å γ = 90°.
Volume	6408.2(4) Å^3
Z	4
Density (calculated)	1.571 Mg/m^3
Absorption coefficient	0.465 mm^{-1}
F(000)	3040
Crystal size	0.30 x 0.20 x 0.15 mm^3
Theta range for data collection	1.63 to 25.25°.
Index ranges	-23<=h<=24, -13<=k<=19, -23<=l<=23
Reflections collected	91910
Independent reflections	11592 [R(int) = 0.0532]
Completeness to theta = 25.25°	100.0 %
Absorption correction	Semi-empirical from equivalents
Max. and min. transmission	0.9328 and 0.8941
Refinement method	Full-matrix-block least-squares on F^2
Data / restraints / parameters	11592 / 441 / 946
Goodness-of-fit on F^2	1.106
Final R indices [I>2sigma(I)]	R1 = 0.0616, wR2 = 0.1768
R indices (all data)	R1 = 0.0823, wR2 = 0.1881
Largest diff. peak and hole	2.070 and -1.016 e.Å^{-3}

X-Ray data for [5-Rh]BAr_F

Figure S40. ORTEP view of molecular structure of complex **[5-Rh]BAr_F** with thermal ellipsoids drawn at the 30% level. The hydrogen atoms are omitted by clarity.

Table S11. Selected bond lengths (Å) and angles (°) for **[5-Rh]BAr_F**.

Bond distances (Å)			
Rh(1)–C(30)	2.009(7)	Rh(1)–C(21)	2.153(9)
Rh(1)–H(31C)	1.9373	Rh(1)–C(22)	2.123(8)
Rh(1)–N(2)	2.153(5)	Rh(1)–C(23)	2.179(6)
N(1)–C(30)	1.431(8)	Rh(1)–C(24)	2.259(6)
Rh(1)–C(20)	2.188(7)		
Angles (°)			
C(30)-Rh(1)-N(2)	78.2(3)	C(7)-N(1)-C(30)	118.3(5)
C(30)-Rh(1)-H(31C)	63.9	N(1)-C(7)-N(2)	114.5(5)
N(2)-Rh(1)-H(31C)	88.5	N(1)-C(30)-Rh(1)	111.5(4)
C(7)-N(2)-Rh(1)	112.3(4)	C(31)-H(31C)-Rh(1)	103.15

Table S12. Crystal data and structure refinement for **[5-Rh]BAr_F**.

Empirical formula	$C_{127}H_{98}B_2Cl_2F_{48}N_4Rh_2$
	$[2(C_{31}H_{36}N_2Rh), 2(C_{32}H_{12}BF_{24}), CH_2Cl_2]$
Formula weight	2890.43
Temperature	173(2) K
Wavelength	0.71073 Å
Crystal system	Triclinic
Space group	P $\bar{1}$
Unit cell dimensions	a = 12.6275(7) Å α= 81.802(2)°.
	b = 14.4679(9) Å β= 82.011(2)°.
	c = 19.0388(12) Å γ = 88.103(2)°.
Volume	3409.0(4) Å^3
Z	1
Density (calculated)	1.408 Mg/m^3
Absorption coefficient	0.394 mm^{-1}
F(000)	1454
Crystal size	0.20 x 0.10 x 0.10 mm^3
Theta range for data collection	1.09 to 25.25°.
Index ranges	-15<=h<=15, -16<=k<=17, -22<=l<=22
Reflections collected	61753
Independent reflections	12273 [R(int) = 0.0619]
Completeness to theta = 25.25°	99.3 %
Absorption correction	Semi-empirical from equivalents
Max. and min. transmission	0.961 and 0.954
Refinement method	Full-matrix-block least-squares on F^2
Data / restraints / parameters	12273 / 405 / 973
Goodness-of-fit on F^2	1.058
Final R indices [I>2sigma(I)]	R1 = 0.0641, wR2 = 0.1467
R indices (all data)	R1 = 0.1200, wR2 = 0.2189
Largest diff. peak and hole	2.245 and -0.765 e.Å^{-3}

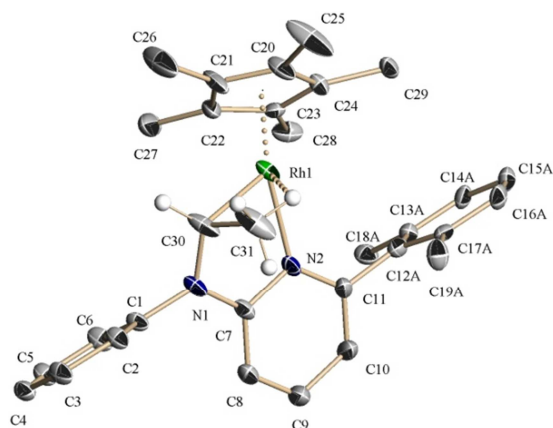**X-Ray data for [6-Ir]BAr_F**
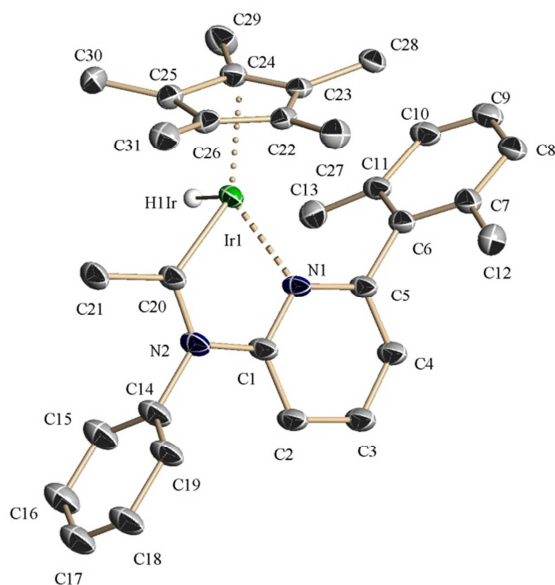
Figure S41. ORTEP view of molecular structure of complex **[6-Ir]BAr_F** with thermal ellipsoids drawn at the 30% level. The hydrogen atoms are omitted by clarity.

Table S13. Selected bond lengths [Å] and angles [°] for **[6-Ir]BAr_F**.

Bond Distances (Å)			
Ir(1)–C(20)	1.911(12)	Ir(1)–C(23)	2.340(11)
Ir(1)–N(1)	2.113(8)	Ir(1)–C(24)	2.280(13)
Ir(1)–H(1Ir)	1.6070	Ir(1)–C(25)	2.161(12)
N(2)–C(20)	1.345(14)	Ir(1)–C(26)	2.226(10)
Ir(1)–C(22)	2.284(11)		

Bond Angles (°)			
C(20)-Ir(1)-N(1)	78.4(4)	C(20)-N(2)-C(1)	115.5(10)
C(20)-Ir(1)-H(1Ir)	89.1	N(1)-C(1)-N(2)	116.2(10)
N(1)-Ir(1)-H(1Ir)	87.0	N(2)-C(20)-Ir(1)	118.8(8)
C(1)-N(1)-Ir(1)	111.1(7)		

Table S14. Crystal data and structure refinement for **[6-Ir]BAr$_F$**.

|	
Empirical formula	$C_{63}H_{48}BF_{24}IrN_2$
$[C_{32}H_{12}BF_{24}, C_{31}H_{36}IrN_2]$	
Formula weight	1492.04
Temperature	173(2) K
Wavelength	0.71073 Å
Crystal system	Monoclinic
Space group	C c
Unit cell dimensions	a = 19.8075(10) Å α= 90°.
	b = 20.1986(9) Å β= 98.691(2)°.
	c = 16.7605(8) Å γ = 90°.
Volume	6628.6(5) Å^3
Z	4
Density (calculated)	1.495 Mg/m^3
Absorption coefficient	2.120 mm^{-1}
F(000)	2952
Crystal size	0.40 x 0.40 x 0.20 mm^3
Theta range for data collection	1.80 to 25.25°.
Index ranges	-22<=h<=23, -23<=k<=24, -20<=l<=20
Reflections collected	32258
Independent reflections	9610 [R(int) = 0.0331]
Completeness to theta = 25.25°	98.7 %
Absorption correction	Semi-empirical from equivalents
Max. and min. transmission	0.6544 and 0.4543
Refinement method	Full-matrix-block least-squares on F^2
Data / restraints / parameters	9610 / 464 / 936
Goodness-of-fit on F^2	1.094
Final R indices [I>2sigma(I)]	R1 = 0.0606, wR2 = 0.1594
R indices (all data)	R1 = 0.0659, wR2 = 0.1640
Absolute structure parameter	0.046(12)
Largest diff. peak and hole	1.894 and -1.769 e.Å^{-3}

X-Ray data for [7-Ir]BAr_F
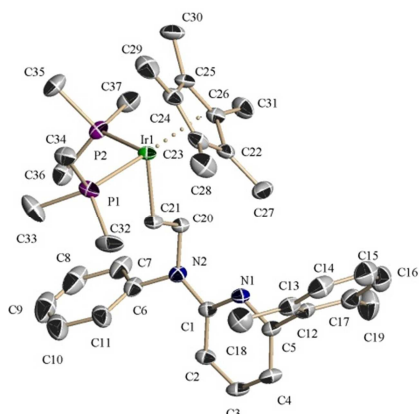
Figure S42. ORTEP view of molecular structure of complex **[7-Ir]BAr_F** with thermal ellipsoids drawn at the 30% level. The hydrogen atoms are omitted by clarity.

Table S15. Selected bond lengths [Å] and angles [°] for **[7-Ir]BAr_F**

Bond Distances (Å)			
Ir(1)–C(21)	2.140(4)	Ir(1)–C(23)	2.246(5)
Ir(1)–P(1)	2.2854(13)	Ir(1)–C(24)	2.278(4)
Ir(1)–P(2)	2.2734(12)	Ir(1)–C(25)	2.281(4)
C(20)–C(21)	1.534(6)	Ir(1)–C(26)	2.236(5)
Ir(1)–C(22)	2.267(5)		
Bond Angles (°)			
P(1)-Ir(1)-P(2)	96.22(5)	Ir(1)-C(21)-C(20)	117.6(3)
P(1)-Ir(1)-C(21)	83.23(13)	C(21)-C(20)-N(2)	112.0(4)
C(21)-Ir(1)-P(2)	89.86(13)		

Table S16. Crystal data and structure refinement for **[7-Ir]BAr$_F$**.

|	
Empirical formula	C$_{69}$H$_{66}$BF$_{24}$IrN$_2$P$_2$
[C$_{32}$H$_{12}$BF$_{24}$, C$_{37}$H$_{54}$IrN$_2$P$_2$]	
Formula weight	1644.19
Temperature	213(2) K
Wavelength	0.71073 Å
Crystal system	Triclinic
Space group	P $\bar{1}$
Unit cell dimensions	a = 12.9657(5) Å α = 73.5760(10)°.
	b = 16.5362(7) Å β = 72.1220(10)°.
	c = 18.6342(7) Å γ = 84.342(2)°.
Volume	3646.9(2) Å^3
Z	2
Density (calculated)	1.497 Mg/m^3
Absorption coefficient	1.976 mm^{-1}
F(000)	1644
Crystal size	0.30 x 0.20 x 0.20 mm^3
Theta range for data collection	1.19 to 25.25°.
Index ranges	-15<=h<=15, -19<=k<=19, -22<=l<=20
Reflections collected	70290
Independent reflections	13174 [R(int) = 0.0384]
Completeness to theta = 25.25°	99.7 %
Absorption correction	Semi-empirical from equivalents
Max. and min. transmission	0.6933 and 0.5886
Refinement method	Full-matrix-block least-squares on F^2
Data / restraints / parameters	13174 / 279 / 946
Goodness-of-fit on F^2	1.111
Final R indices [I>2sigma(I)]	R1 = 0.0370, wR2 = 0.1065
R indices (all data)	R1 = 0.0413, wR2 = 0.1096
Largest diff. peak and hole	1.508 and -0.688 e.Å^{-3}

X-Ray data for [8-Ir]BAr_F
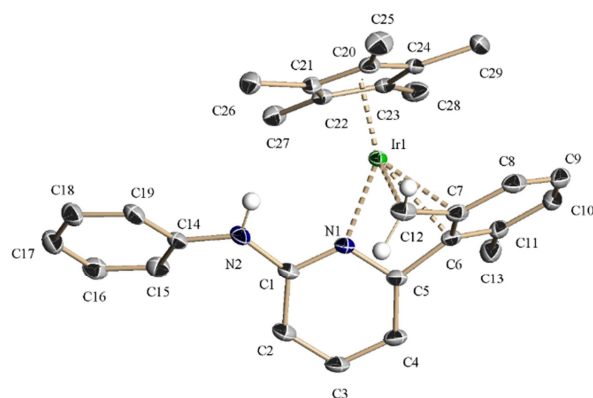
Figure S43. ORTEP view of molecular structure of complex **[8-Ir]BAr_F** with thermal ellipsoids drawn at the 30% level. The hydrogen atoms are omitted by clarity.

Table S17. Selected bond lengths [Å] and angles [°] for **[8-Ir]BAr_F**

Bond Distances (Å)			
Ir(1)–N(1)	2.086(3)	C(10)–C(11)	1.378(6)
Ir(1)–C(6)	2.387(4)	C(6)–C(11)	1.423(6)
Ir(1)–C(7)	2.252(4)	Ir(1)–C(20)	2.170(3)
Ir(1)–C(12)	2.118(4)	Ir(1)–C(21)	2.153(4)
C(6)–C(7)	1.449(5)	Ir(1)–C(22)	2.202(3)
C(7)–C(12)	1.449(6)	Ir(1)–C(23)	2.225(4)
C(7)–C(8)	1.423(6)	Ir(1)–C(24)	2.187(4)
C(8)–C(9)	1.355(7)	Ir(1)–H(2N)	2.891
C(9)–C(10)	1.408(6)		
Bond Angles (°)			
N(1)-Ir(1)-C(6)	62.04(12)	N(1)-Ir(1)-C(12)	80.11(14)
C(7)-Ir(1)-C(6)	36.27(13)	N(1)-C(5)-C(6)	108.5(3)
C(12)-Ir(1)-C(7)	38.59(16)	N(1)-C(1)-N(2)	115.1(3)

Table S18. Crystal data and structure refinement for **[8-Ir]BAr$_F$**.

|	
Empirical formula	C$_{61}$H$_{44}$BF$_{24}$IrN$_2$
[C$_{32}$H$_{12}$BF$_{24}$, C$_{29}$H$_{32}$IrN$_2$]	
Formula weight	1463.99
Temperature	173(2) K
Wavelength	0.71073 Å
Crystal system	Triclinic
Space group	P -1
Unit cell dimensions	a = 12.2362(6) Å α= 91.3100(10)°.
	b = 13.0883(6) Å β= 90.8470(10)°.
	c = 18.4287(8) Å γ = 93.2790(10)°.
Volume	2945.4(2) Å^3
Z	2
Density (calculated)	1.651 Mg/m^3
Absorption coefficient	2.384 mm^{-1}
F(000)	1444
Crystal size	0.50 x 0.30 x 0.20 mm^3
Theta range for data collection	1.89 to 25.25°.
Index ranges	-14<=h<=14, -15<=k<=15, -20<=l<=22
Reflections collected	54111
Independent reflections	10558 [R(int) = 0.0357]
Completeness to theta = 25.25°	99.0 %
Absorption correction	Semi-empirical from equivalents
Max. and min. transmission	0.6211 and 0.4279
Refinement method	Full-matrix-block least-squares on F^2
Data / restraints / parameters	10558 / 265 / 811
Goodness-of-fit on F^2	1.070
Final R indices [I>2sigma(I)]	R1 = 0.0289, wR2 = 0.0776
R indices (all data)	R1 = 0.0323, wR2 = 0.0790
Largest diff. peak and hole	1.455 and -0.681 e.Å^{-3}

X-Ray data for [8-Rh]BAr_F
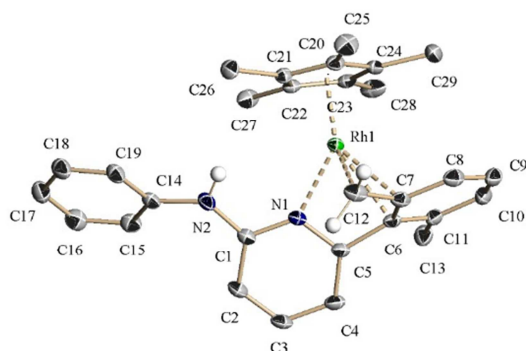
Figure S44. ORTEP view of molecular structure of complex **[8-Rh]BAr_F** with thermal ellipsoids drawn at the 30% level. The hydrogen atoms are omitted by clarity.

Table S19. Selected bond lengths (Å) and angles (°) for **[8-Rh]BAr_F**.

Bond distances (Å)			
Rh(1)–N(1)	2.101(3)	C(10)–C(11)	1.372(7)
Rh(1)–C(6)	2.379(4)	C(6)–C(11)	1.428(7)
Rh(1)–C(7)	2.237(4)	Rh(1)–C(20)	2.176(4)
Rh(1)–C(12)	2.124(5)	Rh(1)–C(21)	2.155(4)
C(6)–C(7)	1.441(6)	Rh(1)–C(22)	2.191(4)
C(7)–C(12)	1.437(7)	Rh(1)–C(23)	2.218(4)
C(7)–C(8)	1.432(7)	Rh(1)–C(24)	2.174(4)
C(8)–C(9)	1.350(8)	Rh(1)–H(2N)	2.987
C(9)–C(10)	1.406(8)		
Angles (°)			
N(1)-Rh(1)-C(6)	62.43(14)	N(1)-Rh(1)-C(12)	81.00(17)
C(7)-Rh(1)-C(6)	36.21(16)	N(1)-C(5)-C(6)	110.3(4)
C(12)-Rh(1)-C(7)	38.37(19)	N(1)-C(1)-N(2)	115.4(4)

Table S20. Crystal data and structure refinement for **[8-Rh]BAr$_F$**.

|	
Empirical formula	$C_{61}H_{44}BF_{24}N_2Rh$
$[C_{32}H_{12}BF_{24}, C_{29}H_{32}N_2Rh]$	
Formula weight	1374.70
Temperature	173(2) K
Wavelength	0.71073 Å
Crystal system	Triclinic
Space group	P $\bar{1}$
Unit cell dimensions	a = 12.2207(3) Å $\quad$ α= 91.176(2)°.
	b = 13.0773(4) Å $\quad$ β= 90.924(2)°.
	c = 18.3938(5) Å $\quad$ γ = 93.482(2)°.
Volume	2933.09(14) Å^3
Z	2
Density (calculated)	1.557 Mg/m^3
Absorption coefficient	0.409 mm^{-1}
F(000)	1380
Crystal size	0.50 x 0.30 x 0.20 mm^3
Theta range for data collection	1.56 to 25.25°.
Index ranges	-14<=h<=14, -15<=k<=15, -22<=l<=21
Reflections collected	65306
Independent reflections	10620 [R(int) = 0.0297]
Completeness to theta = 25.25°	99.8 %
Absorption correction	Semi-empirical from equivalents
Max. and min. transmission	0.9226 and 0.8626
Refinement method	Full-matrix-block least-squares on F^2
Data / restraints / parameters	10620 / 265 / 811
Goodness-of-fit on F^2	1.057
Final R indices [I>2sigma(I)]	R1 = 0.0518, wR2 = 0.1465
R indices (all data)	R1 = 0.0573, wR2 = 0.1520
Largest diff. peak and hole	1.912 and -0.698 e.Å^{-3}

V.   COMPUTATIONAL DETAILS
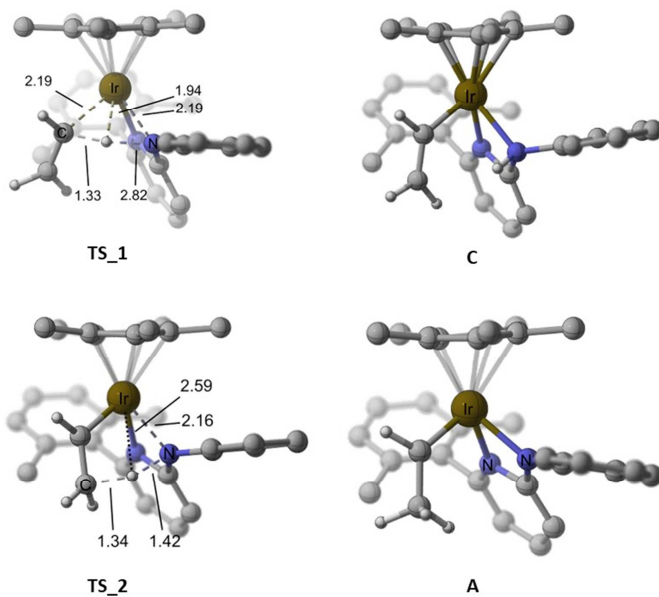
Figure S45. DFT optimized geometries of relevant intermediates and transition states of the calculated ethylidene route to complex **6-Ir$^+$**.
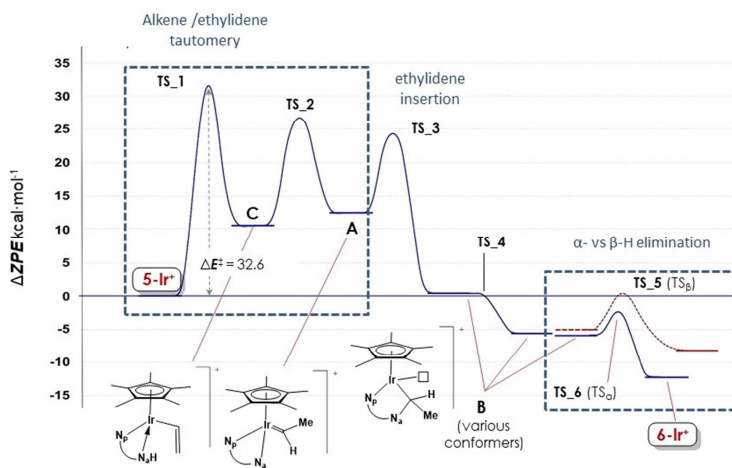

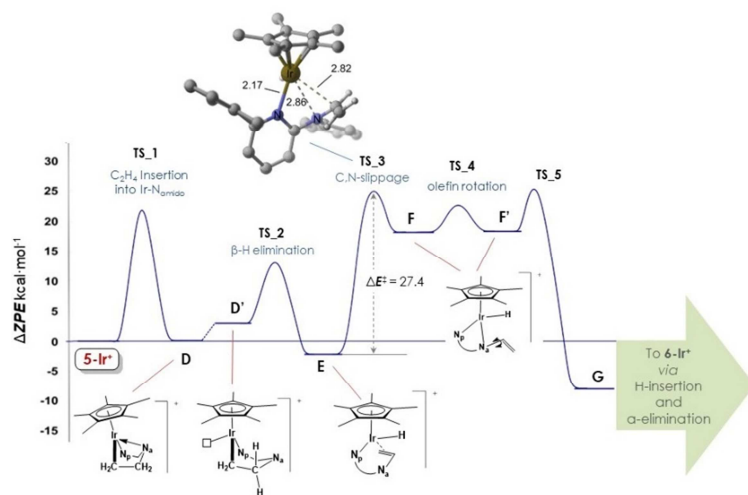Figure S46. Energy profile for the ethylidene route to complex **6-Ir$^+$**.

Figure S47. Energy profile including the initial steps of the migratory insertion path.

VI. REFERENCES

(1)   Bruker (**2007**). *APEX2*. Bruker AXS Inc., Madison, Wisconsin, USA.

(2)   Bruker (**2001**). *APEX2*. Bruker AXS Inc., Madison, Wisconsin, USA.

(3)   Burla, C. M.; Camalli, M.; Carrozzini, B.; Cascarano, G. L.; Giacovazzo, C.; Poliori, G.; Spagna, R. *SIR2002*: the program. *J. Appl. Cryst.* **2003**, *36*, 1103–1103.

(4)   Sheldrick, G. M. A short history of *SHELX*. *Acta Crystallogr.* **2008**, A64, 112–122.

(5)   Spek, A. L. Single-crystal structure validation with the program *PLATON*. *J. Appl. Crystallogr.* **2003**, *36*, 7–13.

(6)   Van der Sluis, P.; Spek, A. L. *BYPASS*: an effective method for the refinement of crystal structures containing disordered solvent regions. *Acta Crystallogr.* **1990**, A*46*, 194–201.